

Intramanifold level mixing by time-dependent electric fields: Multilevel Landau-Zener effect

David A. Harmin

Department of Physics and Astronomy, University of Kentucky, Lexington, Kentucky 40506-0055

(Received 9 January 1991)

The mixing of substates of an isolated Rydberg manifold (constant n, m) is studied using time-evolution matrices $U(t, t_0)$. Coherent mixing is effected by a linearly ramped electric field, $F(t) = \dot{F}t$. The spherical l basis, diabatic (hydrogenic) p basis, and adiabatic (nonhydrogenic) q basis are considered. In the linear Stark regime, the diabatic levels are coupled by $F(t)$ through the atomic core, parametrized by quantum defects. The resulting adiabatic levels E_q^F in this model group into a submanifold degenerate at $F=0$ plus shifted levels split off from the adiabatic manifold. Analytical expressions for the q levels E_q^r and their coupling Γ_{qq}^r are derived as a function of rescaled field or time τ . The time evolution of the levels' populations is studied first for the two-level case—the usual Landau-Zener effect (LZE)—which is generalized to a multilevel Landau-Zener effect (MLZE) for any n manifold. The matrices $U(t, t_0)$ are constructed in the Riemann product representation, including Magnus corrections up to fourth order. The probability $P_{q \rightarrow q'}(V_l)$ of making a transition from state q to q' upon a one-way pass across the manifold depends on a single parameter $V_l = [2\mu_l^2 / (3\dot{F}n^9)]^{1/2}$ (when one $\mu_l \neq 0$). Numerical results for $l=m=0$ indicate that either diabatic ($p \rightarrow p' = p$) or adiabatic ($q \rightarrow q' = q$) transitions always predominate, no matter what the ramp rate \dot{F} . Strong evidence supports the conjecture that outer diabatic transitions between edge states of a manifold obey $P_n^{\text{diab}}(V) = \exp(-\beta_n \pi V^2)$ for $l=m=0$, with $\beta_n = 1$ for $n=2$ (the LZE) and $\beta_n \approx \ln n$ for $n \gg 2$ (the MLZE), and that a similar analytical result holds for arbitrary $\{\mu_i\}$ and m .

I. INTRODUCTION

The transfer of population between eigenstates of a quantum-mechanical system is usually envisaged as proceeding in two possible ways: (1) an external time-dependent potential, such as a weak photon field, may couple the states, or (2) the energy levels themselves may shift in response to a parameter of the system that varies in time. Examples of the latter include variable internuclear separation in atomic collisions, spin precession in atomic beams passing through a magnetic field, and any electric or magnetic field applied externally to an atom. The standard two-level models for these processes lead to (1) the optical Bloch equations and Rabi oscillations, and (2) the Landau-Zener effect (LZE), respectively [1]. The application of a weak, homogeneous but time-dependent electric field $\mathbf{F} = F(t)\hat{z}$ to an atom in a highly excited state offers the opportunity to study both Rabi oscillations and the LZE in a multilevel setting. This paper, the first in a series on Stark level mixing, will explore the effects of linearly ramped fields on population distributions within an isolated Stark manifold.

This study is experimentally motivated. Rubbmark *et al.* [2] considered two-level avoided crossings subject to arbitrary $F(t)$. Their experiments showed that anticrossing Stark levels in Li are indeed mixed by linearly ramped fields in accordance with the LZE. In an effort to understand selective-field ionization, other researchers [3] followed an initially populated level through the sequences of level anticrossings encountered as the field is ramped to values sufficient to ionize the atom ($F \gtrsim 0.1n^{-4}$ a.u.). The compounded probability of steer-

ing adiabatically or diabatically along one path or another as a function of ramp rate presumably underlies general rules for identifying initial states with ionization signals. When a state is initially populated at near-zero fields, however, coherent state mixing within an isolated Stark manifold is critical to determining the relative fractions of states emerging at higher fields. This view was suggested by other observations of ionization rates of He atoms in static [4] and microwave [5] fields. Rolfes, Smith, and MacAdam [6] exposed excited Na atoms to slewed fields that were reversed once through $F=0$ and observed ionization signals attributable to a redistribution of population within a *single* Stark n manifold.

The key process that needs to be addressed is how a time-dependent electric field mixes a manifold of levels amongst themselves. To this end we consider a theoretical model based on the linear Stark effect in Rydberg spectra of singly excited atoms. We introduce the model with a brief discussion of Stark manifolds, the range of field values for which the model is valid in practice, and the form of $F(t)$. [Atomic units are assumed unless noted otherwise. To convert to a.u.: F (a.u.) = $1.945 \times 10^{-10} F$ (V/cm), dF/dt (a.u.) = $4.704 \times 10^{-21} dF/dt$ (V/cm μsec).]

The energy level of a hydrogenic state of principal quantum number n and fixed $m = |m_l|$, $E_n = -\frac{1}{2}n^{-2}$, is split by a static field $\mathbf{F} = F\hat{z}$ ($F > 0$) into a manifold of $n - m$ levels, where the projection m_l of angular momentum onto the field axis is a good quantum number [7]. These hydrogenic levels lie at [8–10]

$$E_{nm_1m}(F) = -\frac{1}{2}n^{-2} + \frac{3}{2}Fn(n_1 - n_2) + O(F^2n^6), \quad (1.1)$$

where $n_i=0, 1, \dots, n-m-1$ ($i=1, 2$) are the usual parabolic quantum numbers and $n_1+n_2+m+1=n$; adjacent levels have spacing $\Delta E(F)=3Fn$. The gross structure of the *nonhydrogenic* n manifold at moderate field strengths imitates the hydrogenic fan of levels (see Fig. 1). Most of the levels appear to cross at E_n at zero field and all nearly attain the same equal spacing $\Delta E(F)$ at large fields. However, at $F=0$ the few lowest angular momentum states are shifted to their Rydberg levels by core effects:

$$E_{n_l} = -\frac{1}{2}(n - \mu_l)^{-2} \approx E_n - \mu_l n^{-3}, \quad (1.2)$$

where μ_l is the quantum defect (mod 1) (with $|\mu_l| < \frac{1}{2}$) for the Rydberg series [11]. Thus, the essential structure of this “bowtie” model is a field-tuned crossing of many levels at $F=0$ plus at least one level that avoids crossing with the rest (Fig. 1). We assume that all but the largest one or two quantum defects are precisely zero—this will be justified in Sec. V—although numerical calculations

do not require any such restriction.

An *isolated manifold* is defined here to range over field values $|F| \leq F_{\max}$ that extend out to the “hydrogenic” limit, where the $n-m$ levels all diverge linearly. This occurs when the largest Stark shift from E_n exceeds the maximum core shift: $\frac{3}{2}Fn^2 \gg |\mu|n^{-3}$ or

$$F_{\max} = F(\text{hydrogenic}) \gg 2|\mu|/3n^5, \quad (1.3)$$

where μ is the largest quantum defect (mod 1) with $l \geq m$. On a larger scale, however, one sees from a Stark map [12] of energy levels versus F that a manifold will overlap its neighbors when its total spread ($\approx 3Fn^2$ a.u.) exceeds the Rydberg level separation ($\approx n^{-3}$ a.u.). Manifolds “interact” wherever $3Fn^5 > 1$ on account of the non-Coulombic potential arising from the core electrons. The resulting forest of avoided crossings must be traversed during selective-field ionization. The focus here on “isolated” n manifolds would seem to require

$$F \ll F(\text{overlapping}) \approx 1/3n^5 = 175(n/25)^{-5} \text{ V/cm}. \quad (1.4)$$

Compatibility of Eqs. (1.3) and (1.4) would then demand $|\mu(\text{mod } 1)| \ll \frac{1}{2}$. Nevertheless, Eq. (1.3) will be taken for granted here for core interactions of any strength [13], even if (1.4) is violated, so that large- F limits of *intra*-manifold effects are well defined. Our treatment of individual n manifolds establishes a prediagonalization scheme; any future considerations of their interactions in the overlap region $3Fn^5 > 1$ will involve the coupling of several isolated manifolds.

Although the nonoverlap criterion (1.4) may be violated in this model, ionization has to be strictly forbidden in order to maintain unitarity within each manifold. If one follows the levels (1.1) out to their intersection with the classical ionization limit $E_{\text{ion}} = -2\sqrt{F}$, one sees that the uppermost level ($n_2=0$) ionizes there first [14] when $Fn^4 \approx 1/(11 + \sqrt{112})$, so we must have

$$F_{\max} < F(\text{ionization}) \approx \frac{1}{21.58} n^{-4}. \quad (1.5)$$

The requirements (1.3) and (1.5) are both satisfied only when n is large and [13] $|\mu| < n/15$; we assume this inequality holds. Note that, as a bonus, the condition $Fn^4 \ll 1$ implies that the linear-Stark approximation used in Eq. (1.1) is a reasonable one. The important features of level mixing will depend anyhow on the crossing and anticrossing substructures within the bowtie as illustrated in Fig. 1—not on nonlinearities in the distant splay of levels.

The nonstatic behavior of $F(t)$ is restricted in this paper to linearly ramped electric fields,

$$F(t) = \dot{F}t, \quad (1.6)$$

where $\dot{F} = dF/dt > 0$ is typically 1–10 000 V/cm μsec . The coherent mixing of state amplitudes as the field (1.6) is ramped through an n manifold will be denoted the multilevel Landau-Zener effect (MLZE). Note that we consider here only a *single* pass through the bowtie, as opposed to the double passage often considered for an-

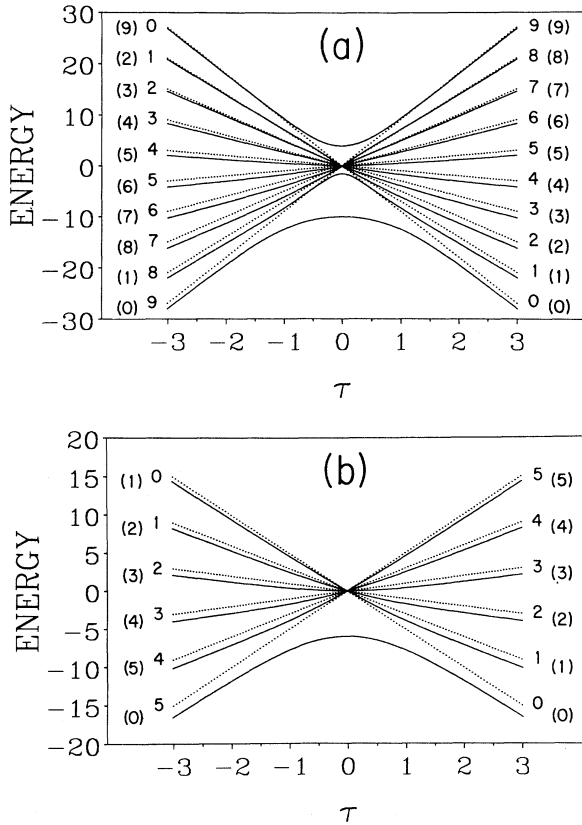


FIG. 1. Stark maps (bowties) of single n manifolds. Field-time scale τ , Eq. (2.24); energy scale is that of (2.26), (2.30), and (3.11), with $V_0=1$. Diabatic levels (dotted lines) labeled n_i : $E_p(\tau) = p\tau$, slopes $p = 2n_1 - n + m + 1$. Adiabatic levels (solid lines) E_q^τ labeled (q). (a) $n=10$, $m=0$, and three nonzero quantum defects, $\mu_0=0.1$, $\mu_1=-0.04$, $\mu_2=0.015$. (b) $n=6$, $m=0$ and one nonzero $\mu_0=0.1$. Note large- $|\tau|$ limits; degeneracies $E_q^\tau=0$ and shift $E_0^\tau = -nV$ at $\tau=0$.

ticrossing molecular states [15]. Evaluation of the MLZE will always consist of (i) populating one Stark eigenstate at an initial time $t_0 \rightarrow -\infty$ (numerically, t_0 will be chosen so that $F \ll -F_{\max}$), (ii) integration of the Schrödinger equation over the range $t_0 < t < |t_0|$ in an appropriate basis, and (iii) evaluation of the manifold's states' amplitudes at $t = |t_0| \rightarrow \infty$ (i.e., at $F \gg F_{\max}$). The time-evolution operator for this system, $\mathbf{U}(\infty, -\infty)$, is to be regarded as a scattering matrix, insofar as the states are uncoupled asymptotically (as $|t|, |F| \rightarrow \infty$) and are mixed only at "short range," i.e., at small values of the field parameter ($|F| < 2|\mu|/3n^5$). Analytical expressions for transition amplitudes are difficult to come by except in special cases (see Secs. III B and IV C); e.g., Demkov's contour-integral method [16] is not directly applicable to the bowtie problem because the diabatic levels (1.1) all have different slopes $dE_{nn_1, m}/dt$. The matrix elements of $\mathbf{U}(t, t_0)$ are computed through its Riemann product representation [17], whose factors, of the form

$$\mathbf{U}(t_2, t_1) = \exp \left[-i \int_{t_1}^{t_2} dt' \mathbf{H}(t') \right], \quad (1.7)$$

are to be calculated for successive small time intervals $[t_1, t_2]$ within the range $[t_0, t]$. A major feature of the present calculation is the use of second- and third-order Magnus corrections [18,19] to the exponent in (1.7), which significantly reduces the number of time steps required for the convergence of $\mathbf{U}(t, t_0)$.

State mixing by nonlinear dynamical fields will be analyzed in subsequent papers and applied to experiments. The computer code TIMEPASS that calculates $\mathbf{U}(t, t_0)$ has been developed and used here for linear fields, but is designed to accommodate arbitrary functions $F(t)$. *Half-traversals* of a manifold, akin to half-scattering or photoionization, wherein an initial population is slewed from $F \approx 0$ to $F = F_{\max}$, have been used in recent experiments of MacAdam [20]; in this case the start-up behavior of the ramp may be critical. Quasioscillatory fields $F(t) = F_0(t) \cos(\omega t + \alpha)$ are relevant to the microwave-induced state mixing observed in the experiments of Ref. [21], and to multiphoton absorption and ionization processes in general. Such potentials are typically handled by Floquet analysis [18,21], but Floquet methods lose their advantage when the Fourier transform of $F(t)$ is no longer simple. The time evolution operators (1.7), on the other hand, can be applied to any form of $F(t)$ and are unitary by construction.

The bowtie model is analyzed in both diabatic (hydrogenic) and adiabatic (nonhydrogenic) bases in Sec. II; the usual LZE is reviewed in this context, and its many-state counterpart (with one quantum defect) is diagonalized semianalytically at fixed F . The positions and coupling of the adiabatic levels is analyzed in some detail in II C to provide the groundwork for future studies of n manifolds. In Sec. III, the time dependence of $F(t)$ is invoked to generate $\mathbf{U}(t, t_0)$ and $\mathbf{U}(\infty, -\infty)$, including Magnus corrections and limiting cases amenable to analytical treatment. In Sec. IV we present numerical results, including the evolution of $\mathbf{U}(t, t_0)$ with t ; the mixture of states represented by $\mathbf{U}(\infty, -\infty)$ upon full traversal

across the manifold; variations with n ; the MLZE, and its implications for experiments. The effects of additional quantum defects are briefly considered in Sec. V. Concluding remarks are given in Sec. VI, and some mathematical results are collected in the Appendixes, including convergence properties of $\mathbf{U}(t_2, t_1)$.

II. THE BOWTIE MODEL—ANALYSIS

A. General formulation, basis sets

The wave function Ψ of the Rydberg electron will evolve in time according to the Schrödinger equation,

$$i \frac{\partial \Psi}{\partial t} = \hat{\mathbf{H}} \Psi = \left[-\frac{1}{2} \nabla^2 - \frac{1}{r} + \mathbf{r} \cdot \mathbf{F}(t) + V_{\text{non-H}}(\mathbf{r}) \right] \Psi. \quad (2.1)$$

The Hamiltonian operator $\hat{\mathbf{H}}(F)$ includes the following potential energy terms: $-1/r$, the asymptotic Coulomb potential of the nucleus and core electrons; $\mathbf{r} \cdot \mathbf{F}(t) = zF(t)$, the Stark potential; and $V_{\text{non-H}}(\mathbf{r})$, an effective, short-range potential representing all nonhydrogenic effects of the core electrons (screening, exchange, etc.) aside from the Coulomb term. Consider an orthonormal basis set of wave functions $\{\psi_k(\mathbf{r})\}$ that may depend on the field $F(t)$ and hence on t . Each ψ_k is an eigenfunction of $\hat{\mathbf{L}}_z$ and the set is taken to lie in a subspace of fixed [7] $m = 0, 1, \dots$. The basis spans a Stark manifold of fixed n , where it contains $n - m$ states. The $n - m$ values of the index k will refer implicitly to the quantum numbers (n, m) and explicitly to a third label (l or p or q) that depends on our choice of basis. The expansion

$$\Psi(t) = \sum_{k'} a_{k'}(t) \psi_{k'}, \quad (2.2)$$

when substituted into Eq. (2.1), leads to a set of $n - m$ coupled linear differential equations for the coefficients $\{a_k(t)\}$:

$$i \frac{da_k}{dt} = \sum_{k'} \left[H_{kk'}(F) - i \left\langle \psi_k \left| \frac{\partial \psi_{k'}}{\partial t} \right. \right\rangle \right] a_{k'}, \quad (2.3)$$

where $H_{kk'}(F) = \langle \psi_k | \hat{\mathbf{H}}(F) | \psi_{k'} \rangle$ and we have used $\langle \psi_k | \psi_{k'} \rangle = \delta_{kk'}$. The effective Hamiltonian in large parentheses in Eq. (2.3) is Hermitian, so the normalization condition

$$\langle \Psi | \Psi \rangle = \sum_k |a_k(t)|^2 = 1 \quad (2.4)$$

holds at all times. We will let the time dependence of the function $F(t)$ remain implicit and arbitrary for the time being.

Three different bases $\{\psi_k(\mathbf{r})\}$ are appropriate representations for the amplitudes $\{a_k(t)\}$ in various regions of the manifold (Fig. 1). Note that in the absence of both Stark and atomic potentials ($F = 0$ and $\mu_l = 0$), all (hydrogenic) eigenfunctions are degenerate at E_n . This Coulomb degeneracy arises from the $O(4)$ symmetry of Eq. (2.1) whereby it is separable in both spherical and

parabolic coordinates [8]. Henceforth all energies will be shifted by $-E_n$ so that a chosen n th Rydberg level of hydrogen occurs at $E=0$ and subscripts n are no longer necessary.

1. Spherical basis

The $\{\psi_l(\mathbf{r})\}$ are the zero-field spherical eigenfunctions of hydrogen (n, m fixed), labeled by $l=m, \dots, n-1$. They diagonalize $\hat{\mathbf{H}}$ when $F=0$ in Eq. (2.1) but core effects shift their eigenenergies to [13]

$$E_l = \langle \psi_l | V_{\text{non-H}} | \psi_l \rangle = -\mu_l n^{-3} \quad (2.5)$$

[cf. Eq. (1.2)]. The exact eigenstates of the atom can be precisely labeled by l only at zero field. (A common error is to label the adiabatic levels on a Stark map—as they are continued away from $F=0$ —by s, p, d , etc., yet assume the eigenstates retain spherical character even when $|F| \gg 0$.) At $F \neq 0$ each noncrossing level adiabatically tied to $E=E_l$ remains dominated by that ψ_l so long as $|F| \ll 2|\mu_l|/3n^5$, i.e., where the Stark shift from E_l is predominantly quadratic [10]. The levels that cross at $F=0$ [all but three in Fig. 1(a)] correspond to some field-dependent mixture of l states. In any case, the basis functions $\{\psi_l\}$ themselves do not depend on time. Equations (2.3) and (2.1) thus reduce to

$$i \frac{da_l}{dt} = \sum_{l'} H_{ll'}^{\text{spH}}(F) a_{l'}, \quad (2.6)$$

$$H_{ll'}^{\text{spH}}(F) = F \langle \psi_l | z | \psi_{l'} \rangle - \mu_l n^{-3} \delta_{ll'}, \quad (2.7)$$

where

$$\begin{aligned} \langle \psi_l | z | \psi_{l'} \rangle &= \langle \psi_{l'} | z | \psi_l \rangle \\ &= -\frac{3}{2} n \sqrt{n^2 - l^2} \left[\frac{l^2 - m^2}{4l^2 - 1} \right]^{1/2} \delta_{l, l'+1} \end{aligned} \quad (2.8)$$

are the usual dipole matrix elements [22] for $n=n'$ and $l=l'+1 \geq 1$, times an angular matrix element of $\cos\theta$ (the second radical). The Hamiltonian (2.7) is symmetric and tridiagonal—the set of Eqs. (2.6) could represent a system of coupled oscillators. Note that hydrogenic and nonhydrogenic spherical bases are identical here because all states with $n' \neq n$ are discarded. Hence the dipoles used in Eqs. (2.7) and (2.8) are the hydrogenic ones. This is only a matter of convenience, however. The use of nonhydrogenic dipoles would necessitate redefinitions of the eigendipoles $\{p\}$ and transformation coefficients $U_{pl}^{(nm)}$ defined for the diabatic basis [Eqs. (2.9) *et seq.*]—but the essential features of intramanifold level mixing would not change.

2. Diabatic or parabolic basis

The $\{\psi_p(\mathbf{r})\}$ are the hydrogenic Stark states [8,23,24] that diagonalize $\hat{\mathbf{H}}$ when $V_{\text{non-H}}(\mathbf{r})=0$ in Eq. (2.1), which is then separable in parabolic coordinates (ξ, η, ϕ) . The third good quantum number here is the z projection of the Runge-Lenz vector [25],

$$p = n_1 - n_2 = 2n_1 - (n - m - 1), \quad (2.9)$$

which ranges from $-(n-m-1)$ to $+(n-m-1)$ in steps $\Delta p=2$, corresponding to $n_1=0, 1, \dots, n-m-1$. The eigenenergies (1.1) are now

$$E_p(F) = \frac{3}{2} npF, \quad (2.10)$$

to first order. These levels appear as dotted lines in Fig. 1 and in subsequent plots of $E(F)$. The most important feature of these eigenstates is that *each ψ_p is independent of F as long as $Fn^4 \ll 1$* . This is the principal advantage of working within the linear Stark approximation: the hydrogenic states or levels cannot be mixed by any variations in the field whatsoever, so that $\partial\psi_p/\partial t = (\partial\psi_p/\partial F)\dot{F}=0$. Equation (2.3) reduces to

$$i \frac{da_p}{dt} = \sum_{p'} H_{pp'}^{\text{diab}}(F) a_{p'}, \quad (2.11)$$

$$H_{pp'}^{\text{diab}}(F) = E_p(F) \delta_{pp'} + \langle \psi_p | V_{\text{non-H}} | \psi_{p'} \rangle. \quad (2.12)$$

At large F ($|F| \simeq F_{\text{max}}$), $H_{pp'}^{\text{diab}}$ approaches a diagonal matrix having the hydrogenic Stark eigenvalues (2.10), while the exact eigenstates approach $\{\psi_p\}$ as $F \rightarrow \pm\infty$.

The connection between the l and p bases is established for fixed (n, m) by an orthogonal, field-independent transformation [8,10,26] $U_{pl}^{(nm)} = \langle \psi_l | \psi_p \rangle$:

$$\psi_l = \sum_{p=-n+m+1}^{n-m-1} \tilde{U}_{lp}^{(nm)} \psi_p, \quad \psi_p = \sum_{l=m}^{n-1} U_{pl}^{(nm)} \psi_l, \quad (2.13)$$

where $\tilde{\mathbf{U}}^{(nm)}$ is the transpose of the matrix $\mathbf{U}^{(nm)}$. To avoid confusion with the time-evolution matrix $\mathbf{U}(t_2, t_1)$, we define the renormalized coefficients

$$u_{pl} = \sqrt{n} U_{pl}^{(nm)}, \quad (2.14)$$

which obey

$$\sum_p u_{pl} u_{p'l'} = n \delta_{ll'}, \quad \sum_l u_{pl} u_{p'l} = n \delta_{pp'}. \quad (2.14')$$

Table III in Appendix A lists all u_{pl} up to $l=3$. We note the following features: (a) the s state is symmetric; (b) the larger (smaller) $l-m$ is, the more $(u_{pl})^2$ is weighted towards the edges (center) of the manifold, where $|p|/n \lesssim 1$ ($|p|/n \approx 0$); (c) for $m \neq 0$, the projection of ψ_l onto the edge states is very small, $(u_{pl})^2 \simeq \mathcal{O}(n^{-m})$. When applied to Eq. (2.12), the expansion (2.13) and the energies (2.5) and (2.10) yield

$$H_{pp'}^{\text{diab}}(F) = \frac{3}{2} npF \delta_{pp'} - n^{-4} \sum_{l=m}^{n-1} \mu_l u_{pl} u_{p'l} \quad (2.15)$$

for the diabatic basis.

3. Adiabatic or local basis

The $\{\Psi_q^F(\mathbf{r})\}$ are the nonhydrogenic Stark states that exactly diagonalize $\hat{\mathbf{H}}(F)$ at a fixed field value F : $\hat{\mathbf{H}}\Psi_q^F = E_q^F \Psi_q^F$. The energy eigenvalues $\{E_q^F\}$ are labeled from lowest to highest at $F>0$ by $q=0, 1, \dots, n-m-1$. These levels appear as solid lines in Fig. 1. As $F \rightarrow \infty$ the adiabatic states reduce to the pure diabatic states, $p = -(n-m-1), \dots, n-m-1$, and we can then equate q with n_1 . When there are N_+

quantum defects for $l \geq m$ with $\mu_l > 0$, and N_- with $\mu_l < 0$, the lowest N_+ and highest N_- adiabatic levels retain their ordinal positions when continued to $F < 0$; the remaining group of levels cross at $F = 0$ and reverse their order at $F < 0$ [cf. Fig. 1(a) with three shifted levels]. For example, for one nonzero $\mu_l > 0$ the order of levels at $F < 0$ is, from top to bottom, $q = \{1, 2, \dots, n - m - 1, 0\}$ [Fig. 1(b)]. As $F \rightarrow -\infty$ these adiabatic levels reduce to the diabatic levels labeled

$$n_1 = \{0, 1, 2, \dots, n - m - 1\}$$

or

$$p = \{-(n - m - 1), \dots, n - m - 1\},$$

respectively. However, the single noncrossing level ($q = 0$) switches from $n_1 = n - m - 1$ at $F \ll 0$ to $n_1 = 0$ at $F \gg 0$, while each level in the manifold of crossing levels ($q = 1, \dots, n - m - 1$) shifts one notch from $n_1 = q - 1$ at $F \ll 0$ to $n_1 = q$ at $F \gg 0$. At $F = 0$, the subset of q states that do not cross coincides with the subset of l states with $\mu_l \neq 0$.

In order to obtain the Hamiltonian in the adiabatic basis, we write the general expansion (2.2) in the p and q bases as

$$\Psi(t) = \sum_p a_p(t) \psi_p = \sum_q b_q(t) \Psi_q^F. \quad (2.16)$$

We can expand the eigenstates $\{\Psi_q^F\}$ in the diabatic basis at fixed F ,

$$\Psi_q^F = \sum_p c_{pq}^F \psi_p, \quad (2.17)$$

and write the diabatic Hamiltonian (2.15) in diagonalized form (also at fixed F),

$$\mathbf{H}^{\text{diab}}(F) = \mathbf{c}^F \mathbf{E}^F \bar{\mathbf{c}}^F, \quad (2.18)$$

where eigenvectors form the columns of an orthogonal matrix \mathbf{c}^F ($\bar{\mathbf{c}}^F$ is its transpose), and the energies $\{E_q^F\}$ form a diagonal matrix \mathbf{E}^F . The adiabatic and diabatic coefficients are thus related by

$$\mathbf{b} = \bar{\mathbf{c}}^F \mathbf{a}, \quad \mathbf{a} = \mathbf{c}^F \mathbf{b}, \quad (2.19)$$

where \mathbf{b} and \mathbf{a} are column vectors with elements $b_q(t)$ and $a_p(t)$. Finally, substitution of Eqs. (2.18) and (2.19) into Eq. (2.11) yields

$$i \frac{d\mathbf{b}}{dt} = \mathbf{H}^{\text{adi}}(F) \mathbf{b}, \quad (2.20)$$

$$\mathbf{H}^{\text{adi}}(F) = \mathbf{E}^F - i \bar{\mathbf{c}}^F \frac{d\mathbf{c}^F}{dt}. \quad (2.21)$$

In this representation all quantities depend on time through $F = F(t)$. \mathbf{H}^{adi} is the effective Hamiltonian in the large parentheses in Eq. (2.3) with $k \rightarrow q$, $a_k \rightarrow b_q$, $\psi_k \rightarrow \Psi_q$:

$$H_{qq'}^{\text{adi}}(F) = E_q^F \delta_{qq'} - i \frac{dF}{dt} \sum_p c_{pq}^F \frac{\partial c_{pq'}}{\partial F}, \quad F = F(t). \quad (2.22)$$

Unlike the spherical and parabolic states, the adiabatic

states $\{\Psi_q^F\}$ do depend on time because the linear combination (2.17) varies with field through \mathbf{c}^F . Time-varying electric fields thus couple the adiabatic states; however, the couplings in $\mathbf{H}^{\text{adi}}(F)$ die off at large field (see Sec. II C)—in contrast to the off-diagonal terms in $\mathbf{H}^{\text{diab}}(F)$ [Eq. (2.15)], which are independent of field. Note that the trace of the Hamiltonian,

$$\text{tr} \mathbf{H} = \sum_q E_q^F = -n^{-3} \sum_l \mu_l, \quad (2.23)$$

is constant in any basis [(2.7), (2.15), or (2.22)].

We now invoke the linear time dependence (1.6) and further assume that there is only one nonzero μ_l , with $\mu_l > 0$. We define a rescaled time parameter

$$\tau = (\frac{3}{2} n \dot{F})^{1/2} t = (\frac{3}{2} n / \dot{F})^{1/2} F, \quad (2.24)$$

which can equally well be regarded as a field parameter. The diabatic Eqs. (2.11) and (2.15) now read

$$i \frac{da_p}{d\tau} = \sum_{p'} H_{pp'}^{\text{diab}}(\tau) a_{p'}, \quad (2.25)$$

$$H_{pp'}^{\text{diab}}(\tau) = p \tau \delta_{pp'} - V u_{pl} u_{p'l}, \quad (2.26)$$

where

$$V_l = \mu_l n^{-4} (\frac{3}{2} \dot{F} n)^{-1/2} \quad (2.27)$$

is a fundamental parameter measuring the relative importance of core coupling and ramp rate. (The subscript l will be dropped from V_l when only one μ_l is nonzero.) Upon diagonalization of (2.26) [as in Eq. (2.18)], Eqs. (2.20)–(2.22) become

$$i \frac{db_q}{d\tau} = \sum_{q'} H_{qq'}^{\text{adi}}(\tau) b_{q'}, \quad (2.28)$$

$$H_{qq'}^{\text{adi}}(\tau) = E_q^\tau \delta_{qq'} - i \sum_p c_{pq}^\tau \frac{dc_{pq'}^\tau}{d\tau} \quad (2.29)$$

with rescaled energies $E_q^\tau = (\frac{3}{2} \dot{F} n)^{-1/2} E_q^F$. The off-diagonal coupling term in \mathbf{H}^{adi} , $\bar{\mathbf{c}}^\tau d\mathbf{c}^\tau/d\tau \equiv -\Gamma^\tau$, is an antisymmetric matrix. The derivative can be removed by applying $d\mathbf{H}^{\text{diab}}/d\tau = \mathbf{p}$ (diagonal) and $d(\bar{\mathbf{c}}^\tau \mathbf{c}^\tau)/d\tau = 0$ to $\mathbf{H}^{\text{diab}} = \mathbf{c}^\tau \mathbf{E}^\tau \bar{\mathbf{c}}^\tau$:

$$\begin{aligned} H_{qq'}^{\text{adi}}(\tau) &= E_q^\tau \delta_{qq'} + i \delta_{qq'} \frac{\sum_p c_{pq}^\tau p c_{pq'}^\tau}{E_q^\tau - E_{q'}^\tau} \\ &\equiv E_q^\tau \delta_{qq'} + i \Gamma_{qq'}^\tau, \end{aligned} \quad (2.30)$$

where we have defined a special delta symbol, $\delta_{qq'} \equiv 1 - \delta_{qq'}$ ($\delta_{qq'} = 1$ if $q \neq q'$ ($q = q'$)). This is the computationally useful form of \mathbf{H}^{adi} , requiring only diagonalization of Eq. (2.26). Note that the term $i\Gamma^\tau$, while suggestive of dissipative processes, does not represent the loss of flux but only its transfer among the adiabatic channels.

In the τ scale the ramp rate is fixed at unity with V an adjustable ‘‘coupling strength.’’ The energy scale is provided by the trace in Eq. (2.23), which now equals $-nV$. The shift of the $q = 0$ level at $\tau = 0$ also equals $-nV$, since all the other levels are degenerate at $\tau = 0$, $E_q^\tau = 0$. The

above reduction is useful in calculations where fixed time steps are desirable. As V increases, the energy gap and energy scale $\Delta E = nV$ expand while the field-time scale is frozen.

B. Two-level Landau-Zener effect

The two-level case provides a familiar framework for the multilevel LZE. This illustration applies to any pair of crossing diabatic levels [27] (same n, m), corresponding to hydrogenic energies $p\tau$ with arbitrary slopes p_1 and p_2 . Ignoring all other states, the diabatic Hamiltonian (2.26) now reads

$$\mathbf{H}^{\text{diab}}(\tau) = \begin{bmatrix} p_1\tau - Vu_1^2 & -Vu_1u_2 \\ -Vu_1u_2 & p_2\tau - Vu_2^2 \end{bmatrix}, \quad (2.31)$$

where $u_k = u_{pl}$ ($k=1,2$) are the projections for $p = p_k$ onto the l state, and $2u^2 \equiv u_1^2 + u_2^2 \leq n$ is the total weight of the two states. (For $l=0$, $u_1^2 = u_2^2 = u^2 = 1$.) The adiabatic levels at field-time value τ are

$$E_{\pm}^{\tau} = -Vu^2 + \bar{p}\tau \pm [(s\tau - Vw)^2 + (Vu_1u_2)^2]^{1/2}, \quad (2.32)$$

where

$$\bar{p} = \frac{1}{2}(p_1 + p_2), \quad s = \frac{1}{2}(p_1 - p_2) \neq 0, \quad (2.33)$$

$$w = \frac{1}{2}(u_1^2 - u_2^2),$$

and $q = \pm$ denotes upper and lower levels here. The center of the anticrossing lies at $\bar{\tau} = Vw/s$ and $\bar{E} = -V(p_1u_2^2 - p_2u_1^2)/(p_1 - p_2)$, where the level separation is a minimum and there is an energy gap [28] $\Delta E = 2V|u_1u_2|$. At fields $|\tau| \gg Vu^2/|s|$ the adiabatic levels approach the diabatic ones but are asymptotically shifted from them by $-Vu_k^2$ ($k=1,2$). Note that the sum of core-induced shifts from the hydrogenic positions has the constant value [28] $-2Vu^2$, in accordance with Eq. (2.23) (in the τ scale).

An exact solution of Eqs. (2.25) is possible only in the two-level case [16,29]. Substitution of

$$a_k(\tau) = A_k(\tau) \exp[-i(\frac{1}{2}p_k\tau^2 - Vu_k^2\tau)] \quad (2.34)$$

and of the Hamiltonian (2.31) into (2.25) yields

$$i\frac{dA_1}{d\tau} = -Vu_1u_2 \exp[+i(s\tau^2 - 2Vw\tau)] A_2, \quad (2.35)$$

$$i\frac{dA_2}{d\tau} = -Vu_1u_2 \exp[-i(s\tau^2 - 2Vw\tau)] A_1$$

in the interaction representation. This pair of equations reduces to uncoupled second-order differential equations for $A_1(\tau)$ and $A_2(\tau)$. The solutions are parabolic cylinder functions whose behavior represents tunneling with a complex energy through a mock potential barrier, as was shown by Zener [15].

Alternatively, integration of Eqs. (2.25) or (2.35) from an initial τ_0 to a final τ yields the integral equation

$$A_k(\tau) = A_k(\tau_0) + iVu_1u_2 \sum_{k'=1}^2 \delta_{kk'} \int_{\tau_0}^{\tau} d\tau' e^{\pm i(s\tau'^2 - 2Vw\tau')} A_{k'}(\tau'), \quad (2.36)$$

where the upper or lower sign is taken for $k=1$ or 2 , respectively. If we assume the initial conditions $A_k(\tau_0)=1$ and $A_{k'}(\tau_0)=0$, repeated iteration of Eq. (2.36) produces an infinite series in powers of $(iVu_1u_2)^2$. For $\tau_0 \rightarrow -\infty$ and $\tau \rightarrow \infty$ this series equals

$$A_k(\infty) = \exp[\frac{1}{2}(iVu_1u_2\sqrt{\pi/|s|})^2]. \quad (2.37)$$

Thus, the probability of making a *diabatic transition*, $1 \rightarrow 1$ or $2 \rightarrow 2$ (i.e., $\pm \rightarrow \mp$), across the anticrossing is

$$P^{\text{diab}} = |a_k(\infty)|^2 = |A_k(\infty)|^2 = \exp\left[-2\pi \frac{(Vu_1u_2)^2}{|p_1 - p_2|}\right]. \quad (2.38)$$

To compare with the standard LZE result [2,8,15], we note that $|Vu_1u_2|$ equals half the energy gap ΔE and that the slopes of the diabatic levels are $p_k = dE_k/d\tau$. Rescaling energies and times to atomic units by the factors $(\frac{3}{2}\tilde{F}n)^{\pm 1/2}$ of Eq. (2.24), we find

$$P^{\text{diab}} = e^{-2\pi\gamma}, \quad \gamma = \frac{(\frac{1}{2}\Delta E)^2}{\tilde{F} \left| \frac{dE_1}{dF} - \frac{dE_2}{dF} \right|}, \quad (2.39)$$

where the slopes are now $dE_p/dF = \frac{3}{2}np$. Equation (2.39) is the usual expression for diabatic transitions [15]; the adiabatic-transition probability ($q = \pm \rightarrow \pm$) is of course $P^{\text{adi}} = 1 - P^{\text{diab}}$. It is especially noteworthy that the exponent goes as $V^2 \sim (\text{coupling strength})^2/(\text{ramp rate})$, according to the definition of V in (2.27).

To obtain a crude estimate of P^{diab} for the whole manifold—i.e., for crossing from the lower edge state ($q=0$) to the upper edge state ($q=n-1$) when there are n levels—we can use the two-level result (2.39) as follows. We take the gap energy to be $\Delta E = \mu_1 n^{-3}$ a.u., the difference in slopes for the edge states ($p \approx \pm n$) to be $3n^2$, and equal weights u_k^2 that add up to n (so $|u_1u_2| = \frac{1}{2}n$). Then Eq. (2.38) or (2.39) gives

$$P^{\text{diab}} \approx e^{-\pi V^2 n/4} \quad (2.40)$$

for the whole manifold. The exponent's characteristic dependence on $V^2 \approx \mu_1^2/\tilde{F}$ is correct, though the factor $n/4$ turns out to be an overestimate for large n . Note that the actual two-level manifold [27] $n=2, m=0$ has

$$P^{\text{diab}} = e^{-\pi V^2}, \quad P^{\text{adi}} = 1 - e^{-\pi V^2}, \quad n=2, \quad (2.41)$$

according to Eq. (2.38).

The larger the coupling V between diabatic levels—or the slower the ramp rate—the greater will be the transfer of population between states 1 and 2 governed by Eqs. (2.35). The time evolution of $|a_k(\tau)|^2$ is depicted in Fig. 2(a) for three disparate values of V and the following pa-

parameter values: $u_1 = u_2 = 1$, $p_1 = +1$, $p_2 = -1$, $\tau_0 = -5$, and initial conditions $a_1(\tau_0) = 1$, $a_2(\tau_0) = 0$. The obvious flopping between states persists at $\tau > 0$ on account of the constancy of the terms $-Vu_k u_{k'}$ in \mathbf{H}^{diab} , Eq. (2.31). At large but finite τ , the diabatic states approach but do not quite equal the eigenstates: their energies differ by the constant shift $-Vu_k^2$ even as $\tau \rightarrow \infty$, hence the oscillations. Their envelopes die down in proportion to τ^{-1} as the level spacing ($\approx 2\tau$) increases, and their mean approaches the limits (2.41) for $k=1 \rightarrow 1$ and $k=1 \rightarrow 2$, shown by arrows in the figure.

The adiabatic populations $|b_{\pm}(\tau)|^2$, plotted in Fig. 2(b), approach the asymptotic limits more smoothly. The adiabatic Hamiltonian (2.30) follows from diagonalization of the matrix (2.31):

$$\mathbf{H}^{\text{adi}}(\tau) = \begin{pmatrix} E_-^{\tau} & i\Gamma^{\tau} \\ -i\Gamma^{\tau} & E_+^{\tau} \end{pmatrix}, \quad (2.42)$$

with eigenvalues (2.32) and coupling

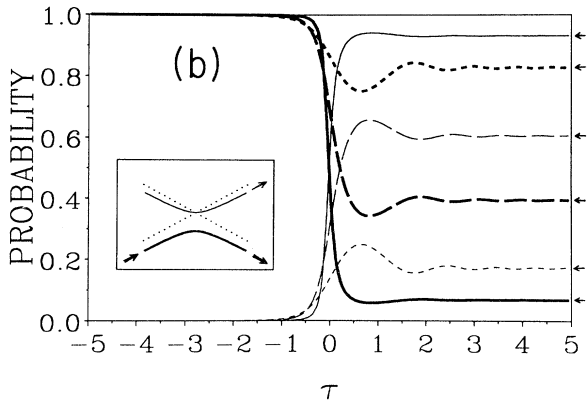
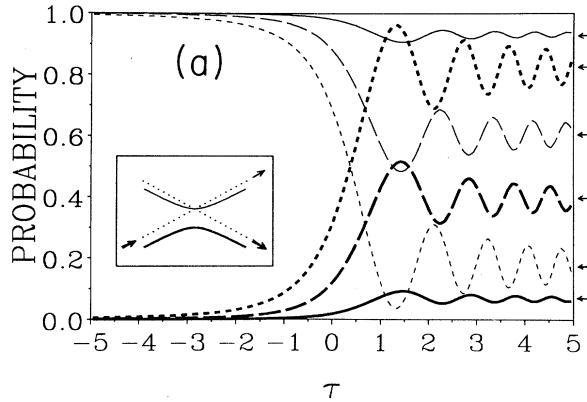


FIG. 2. State populations for $n=2$; $m=0$; initial $a_1(-5) = b_-(-5) = 1$; and $V=0.15$ (solid lines), 0.40 (long-dashed lines), and 0.75 (short-dashed lines). Arrows at right: limiting LZE probabilities (2.41). Thin (thick) curves: diabatic (adiabatic) transitions. (a) Diabatic-basis probabilities $|a_k(\tau)|^2$; $k'=1$ (thin lines), $k'=2$ (thick lines). (b) Adiabatic-basis probabilities $|b_q(\tau)|^2$; $q'=+$ (thin lines), $q'=-$ (thick lines). Insets: two-level bowties, as in Fig. 1.

$$\Gamma^{\tau} = \Gamma_{-+}^{\tau} = -\Gamma_{+-}^{\tau} = \frac{\frac{1}{2}(Vu_1 u_2 / s)}{(\tau - \bar{\tau})^2 + (Vu_1 u_2 / s)^2}. \quad (2.43)$$

The off-diagonal element has the form of a Lorentzian in the field-time variable with full width at half maximum (FWHM) [30]

$$\Delta\tau = 2|Vu_1 u_2 / s| = \Delta E / |s|, \quad (2.44)$$

which functions as an effective width of the anticrossing [31]. Most of the population transfer evident in Fig. 2(b) is thus confined to the range $|\tau| \lesssim \Delta\tau = 2V$, while the rapid falloff of $\Gamma^{\tau} \sim \tau^{-3}$ at $\tau \gg V$ ensures a smooth approach to the limits $P^{\text{adi}} = 1 - e^{-\pi V^2}$ and $P^{\text{diab}} = e^{-\pi V^2}$.

After ramping through a manifold, the final-state population distribution for a given initial state q depends on the single parameter V (if only one μ_l is nonzero). When considering full traversal of an avoided crossing, we will usually present the *adiabatic-level* populations $|b_q(\tau)|^2$ vs V , which will be called $P_{q \rightarrow q'}(V)$ in the limit $\tau = -\tau_0 \rightarrow \infty$. For example, Fig. 3 shows the adiabatic ($q \rightarrow q' = q$) and diabatic ($q \rightarrow q' \neq q$) crossing probabilities $P_{q \rightarrow q'}(V)$ for the two-level case, Eqs. (2.41). The two curves $P_{+ \rightarrow +}$ and $P_{- \rightarrow -}$ are identical, as are the pair $P_{+ \rightarrow -}$ and $P_{- \rightarrow +}$. In the multilevel case this is generally not so. However, for given initial q , $P_{q \rightarrow q'}(V)$ will always mimic the rising adiabatic-transition curve in Fig. 3, and there will always be one final state $q' \neq q$ whose $P_{q \rightarrow q'}(V)$ follows a falling diabatic-transition curve corresponding to some $P_{p \rightarrow p}(V)$. As $\tau \rightarrow \infty$ the distributions for these two final states attain

$$P_{q \rightarrow q} \xrightarrow[V \rightarrow 0]{} 0, \quad P_{q \rightarrow q'} = P_{p \rightarrow p} \xrightarrow[V \rightarrow 0]{} 1 \quad (2.45a)$$

in the diabatic, fast-slew limit ($\dot{F} \rightarrow \infty$ or $\mu_l \rightarrow 0$), and

$$P_{q \rightarrow q} \xrightarrow[V \rightarrow \infty]{} 1, \quad P_{q \rightarrow q'} = P_{p \rightarrow p} \xrightarrow[V \rightarrow \infty]{} 0 \quad (2.45b)$$

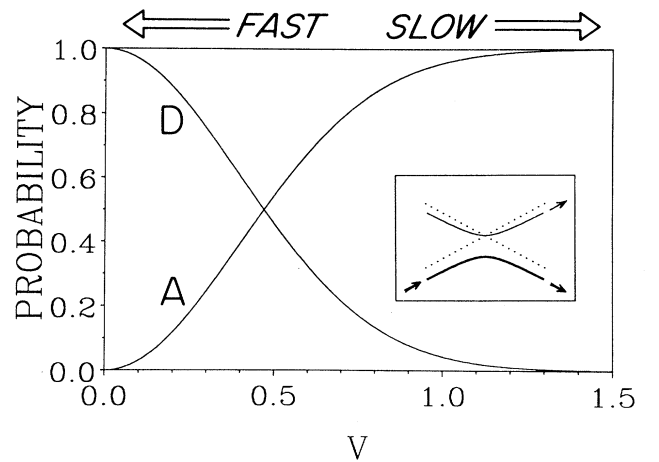


FIG. 3. Limiting transition probabilities vs V for full traversal through a two-level manifold, Eqs. (2.41). Diabatic transitions ($k \rightarrow k' = k$ or $q \rightarrow q' \neq q$), curve D ; adiabatic transitions ($k \rightarrow k' \neq k$ or $q \rightarrow q' = q$), curve A . Note limits (2.45a) and (2.45b).

in the adiabatic, slow-slew limit ($\dot{F} \rightarrow 0$; $V > 1$ in practice). All other $q' \neq q$ vanish in both limits.

C. Many-state diagonalization and adiabatic coupling at fixed field

In this subsection we discuss procedures for approximating \mathbf{H}^{adi} . A full manifold of $n - m$ levels can be treated analytically in a static field [10] (i.e., at fixed τ): the diabatic Hamiltonian (2.26) can be diagonalized, and the eigenvalues $\{E_q^\tau\}$ and eigenvectors $\{c_{pq}^\tau\}$ may then be used to construct the adiabatic Hamiltonian (2.30). Although this is possible for any number of nonzero μ_l via the methods of Ref. [10], we assume here that $\mu_l = 0$ for all l except $\mu_l > 0$ for one $l \geq m$. [The reader should refer to the exemplary plots in Fig. 1(b) for the bowtie eigenvalues, and to Fig. 5 below for the coupling elements $\Gamma_{qq'}^\tau$ for $n = 10$ and $l = 0$; the matrix elements $\Gamma_{qq'}^\tau$ shown in Fig. 5 are representative of both the magnitude and functional form of $\Gamma_{qq'}^\tau$ for any n .] The time dependence of the state amplitudes cannot, however, be solved analytically as in the two-level case. Nevertheless, the analytical structure of \mathbf{H}^{adi} will help elucidate our numerical results for the transition probability curves $P_{q \rightarrow q'}(V)$.

The eigenvalues of \mathbf{H}^{diab} are the $n - m$ solutions E^τ of

$$\begin{aligned} & |(\tau\mathbf{p} - E^\tau\mathbf{1}) - V\mathbf{u}\mathbf{u}| \\ &= \prod_{p'} (p'\tau - E^\tau) - V \sum_p u_{pl}^2 \prod_{p' (\neq p)} (p'\tau - E^\tau) \\ &= \left[1 - V \sum_p \frac{u_{pl}^2}{p\tau - E^\tau} \right] \prod_{p'} (p'\tau - E^\tau) = 0. \end{aligned} \quad (2.46)$$

On the first line of Eq. (2.46), \mathbf{p} is diagonal, $\mathbf{1}$ is the unit matrix, and \mathbf{u} is a column vector of the coefficients (2.14) for a given l ; the sums and products range over $p = -(n - m - 1), \dots, n - m - 1$ in steps of 2. (When $l = m = 0$ the matrix $\mathbf{u}\mathbf{u}$ is just an $n \times n$ matrix filled with ones—cf. Appendix A.) The nonhydrogenic energies are therefore determined implicitly from

$$\sum_p \frac{u_{pl}^2}{p\tau - E^\tau} = \frac{1}{V}. \quad (2.47)$$

At $\tau \gg V$ an expansion of (2.47) in powers of (V/τ) yields

$$E_q^\tau = p\tau - Vu_{pl}^2 - \frac{V^2 u_{pl}^2}{\tau} \sum_{p' (\neq p)} \frac{u_{p'l}^2}{p' - p} + \dots, \quad (2.48)$$

which shows how each solution E_q^τ approaches a particular hydrogenic energy $p\tau$ to within a constant asymptotic shift $-Vu_{pl}^2$. The indices q and p are related at $\tau \gg V$ through $q = n_1$ and Eq. (2.9), and are shifted by one at $\tau \ll -V$, as discussed in Sec. II A. The adiabatic curves $q = 1, \dots, n - m - 1$ in fact lie between the diabatic curves $n_1 = q - 1$ and $n_1 = q$ over the entire range $-\infty < \tau < \infty$, as is evident in Fig. 1(b). This subgroup of levels appear to form a distinct Stark manifold—they all cross at $\tau = 0$ in a pseudohydrogenic bowtie—so they will be referred to as the *adiabatic manifold levels*. The lowest curve $q = 0$ veers below both $n_1 = n - m - 1$ and

$n_1 = 0$ as $\tau \rightarrow 0$, where it evolves into the pure spherical level that is shifted to $-nV$ (in the τ scale). Adiabatic curves that are likewise split from the manifold at $\tau = 0$ are designated *shifted levels* and equal $\{\mu_l \neq 0\}$ in number. Once the manifold of $\{E_q^\tau\}$ is found it is not necessary to solve Eq. (2.47) for $E_q^\tau = 0$, since Eq. (2.23) implies

$$E_0^\tau = -nV - \sum_{q (\neq 0)} E_q^\tau \quad (2.49)$$

at all τ .

The knot of manifold levels at $\tau = 0$ unravels when we rescale the energy so as to remove the linear- τ behavior:

$$\begin{aligned} E^\tau &= 2\tau[\lambda^\varphi - \frac{1}{2}(n - m)], \\ \lambda^\varphi &= \frac{1}{2}[E^\tau/\tau + (n - m)], \end{aligned} \quad (2.50)$$

where

$$\varphi \equiv \frac{2\tau}{V} = \frac{3nF}{\mu_l n^{-4}} \quad (2.51)$$

is a rescaled field variable. Substitution of Eqs. (2.50) and (2.51) into Eq. (2.47) yields

$$\sum_{n_1=0}^{n-m-1} \frac{u_{pl}^2}{n_1 + \frac{1}{2} - \lambda^\varphi} = \varphi, \quad (2.52)$$

where the dependence of u_{pl} on n_1 in the sum is implied by Eq. (2.9). In the λ scale, the hydrogenic solutions $E_p^\tau = p\tau$ ($V \rightarrow 0$) correspond to $\lambda_{n_1}^\varphi = n_1 + \frac{1}{2}$. They mark the poles of the left-hand side of (2.52) and serve to delimit the branches of a tangentlike function of λ^φ ; each branch represents a manifold level λ_q^φ . As was shown in Ref. [10], this function reduces to a simple approximate form for the symmetric case $l = m = 0$ (which has the distribution $u_{p0}^2 = 1$ for all p):

$$\sum_{n_1=0}^{n-1} \frac{1}{n_1 + \frac{1}{2} - \lambda^\varphi} = \pi \tan(\pi\lambda^\varphi) + \ln \left[\frac{n - \lambda^\varphi}{\lambda^\varphi} \right]. \quad (2.53)$$

Other values of l or m result in similar but more complicated functions of λ^φ ; we explicitly consider eigenvalues only for $l = 0$ with $\mu_0 \neq 0$ for the s state [32].

The solution of Eq. (2.52) for the *manifold* levels follows from the inversion of (2.53) [10]:

$$\lambda_q^\varphi = q + \frac{1}{\pi} \tan^{-1}[(\varphi - \sigma_q)/\pi], \quad q = 1, \dots, n - 1, \quad (2.54)$$

$$\sigma_q = \ln \left[\frac{n - q}{q} \right] \quad (2.55)$$

in the λ scale, while eigenvalues $\{E_q^\tau\}$ in the τ scale follow from (2.50), and $\{E_q^F\}$ in a.u. from $E_q^F = (\frac{3}{2}Fn)^{1/2}E_q^\tau$. The branch of the tangent in (2.54) has been chosen to lie within $(-\frac{1}{2}\pi, \frac{1}{2}\pi)$ so that λ_q^φ approaches the hydrogenic solutions $\lambda_q^\varphi = n_1 \pm \frac{1}{2}$ as $\varphi = 2\tau/V \rightarrow \pm\infty$, with $q = n_1 = 1, \dots, n - 1$. Figure 4 shows $\{\lambda_q^\varphi\}$ for $n = 10$. Each eigenvalue (2.54) increases by unity over the range $-\infty < \varphi < \infty$ as the adiabatic level switches from

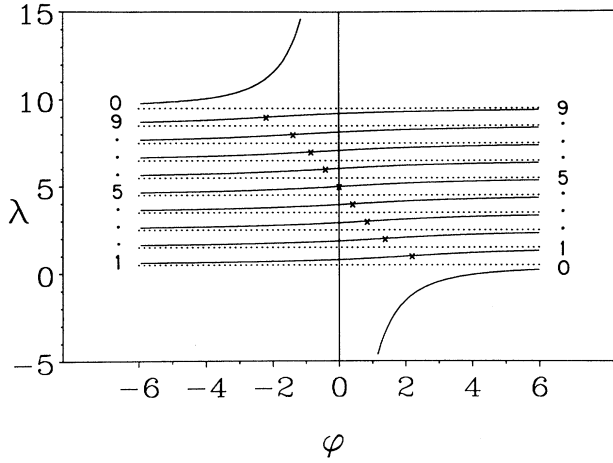


FIG. 4. λ -scale eigenvalues λ_q^φ (solid curves), Eqs. (2.54) and (2.55), vs $\varphi=2\tau/V$ for $n=10$, $m=0$, $\mu_0=0.1$. Numbers label adiabatic manifold levels $q=1, \dots, 9$, shifted level $q=0$. Diabatic levels (dotted curves), $\lambda=n_1+\frac{1}{2}$, $n_1=0, \dots, 9$. Crosses mark the center of each q branch, $\varphi=\sigma_q$.

$\lambda_q^\varphi=q-\frac{1}{2}$ to $\lambda_q^\varphi=q+\frac{1}{2}$. The center of the jump occurs at $\varphi=\sigma_q$: i.e., at $\tau < 0$ for $q=[\frac{1}{2}n]+1, \dots, n-1$ and at $\tau > 0$ for $q=1, \dots, [\frac{1}{2}(n-1)]$ (and at $\tau=0$ for $q=\frac{1}{2}n$ when n is even). Here, the square brackets mean “integral part of.” Retwisting the bowtie back to the energy scale via (2.50) results in the symmetric fanning out of the adiabatic manifold with respect to the hydrogenic one [10] at $\tau \approx 0$ [cf. Fig. 1(b)]. The *shifted* level is obtained from the λ -scale version of Eq. (2.49),

$$\lambda_0^\varphi = n\left(\frac{1}{2}n - \varphi^{-1}\right) - \sum_{q=1}^{n-1} \lambda_q^\varphi, \quad (2.56)$$

which has a simple pole at $\varphi=0$, as seen [32,33] in Fig. 4. Note the approach of λ_0^φ to the hydrogenic edge-state values $\lambda_0^\varphi=n-\frac{1}{2}$ (i.e., $n_1=n-1$) as $\varphi \rightarrow -\infty$ and $\lambda_0^\varphi=\frac{1}{2}$ (i.e., $n_1=0$) as $\varphi \rightarrow \infty$. Also note that one recovers, via Eq. (2.50), the τ -scaled asymptotic levels (2.48) from Eqs. (2.54)–(2.56).

The Schrödinger equation in this “untwisted” scale, $\mathbf{H}^{\text{diab}}(\varphi)\mathbf{c}^\varphi=\mathbf{c}^\varphi\lambda^\varphi$, follows from the Hamiltonian (2.26) and Eq. (2.50):

$$\left[\left(n_1+\frac{1}{2}\mathbf{1}\right)-\varphi^{-1}\mathbf{u}\bar{\mathbf{u}}\right]\mathbf{c}^\varphi=\mathbf{c}^\varphi\lambda^\varphi. \quad (2.57)$$

[In this discussion the parabolic channel index p is retained, so that elements such as $(n_1+\frac{1}{2})_p$ form a diagonal matrix corresponding to values of p given by Eq. (2.9).] The eigenvectors of Eq. (2.57)—which form the columns of \mathbf{c}^φ —are obtained by inspection using the eigenvalue condition (2.52):

$$c_{pq}^\varphi = N_q^\varphi \frac{u_{pl}}{\lambda_q^\varphi - (n_1 + \frac{1}{2})_p}, \quad (2.58)$$

where N_q^φ is a normalization factor for the q th vector at field φ . The composition of eigenstates in the diabatic basis, Eq. (2.17), is obviously dominated by one or the other of the two diabatic states whose hydrogenic levels

bracket the q th level [i.e., $n_1=q$ or $q-1$ for $q \neq 0$; cf. Eq. (2.54) and Fig. 4]. The normalization condition $\sum_p |c_{pq}^\varphi|^2=1$ determines N_q^φ upon application of the operator $d/d\varphi$ to Eq. (2.52):

$$\begin{aligned} N_q^\varphi &= \pm \left[\sum_{n_1=0}^{n-m-1} \left(\frac{u_{pl}}{n_1 + \frac{1}{2} - \lambda_q^\varphi} \right)^2 \right]^{-1/2} \\ &= \pm \left(\frac{d\lambda_q^\varphi}{d\varphi} \right)^{1/2}, \end{aligned} \quad (2.59)$$

where the plus sign applies to all q at all φ —except $q=0$ at $\varphi > 0$, for which the minus sign is to be used. (The sign convention for \mathbf{c}^φ is discussed in Appendix B.) For $\varphi=0$, insertion of the appropriate limits of λ_0^φ and N_0^φ into Eq. (2.58) yields $\lim_{\varphi \rightarrow \pm 0} c_{p0}^\varphi = \pm u_{pl}/\sqrt{n}$, which is seen to reproduce precisely the spherical l state prescribed by Eqs. (2.13) and (2.14). The eigenstates of the adiabatic manifold [10], however, are diagonal in neither the spherical nor the parabolic basis at $\varphi=0$.

Construction of the adiabatic Hamiltonian (2.30) proceeds with the evaluation of the matrix $\bar{\mathbf{c}}^\tau \mathbf{p} \mathbf{c}^\tau$. [Here and below, substitutions such as $\mathbf{c}^\varphi \rightarrow \mathbf{c}^\tau$ accompany the change of parameters $\varphi \rightarrow \tau$, Eq. (2.51).] A simple calculation yields

$$\begin{aligned} \sum_p c_{pq}^\varphi p c_{pq}^\varphi &= 2N_q^\varphi N_{q'}^\varphi \sum_p \frac{u_{pl}^2 \bar{n}_p}{(\bar{n}_p - \lambda_q^\varphi)(\bar{n}_p - \lambda_{q'}^\varphi)} \\ &= 2\varphi N_q^\varphi N_{q'}^\varphi, \end{aligned} \quad (2.60)$$

where we have used Eq. (2.58) for c_{pq}^φ and c_{pq}^φ ; Eq. (2.9) for p and n_1 , with $\bar{n}_p=(n_1+\frac{1}{2})_p$; $\bar{\mathbf{c}}^\varphi \mathbf{c}^\varphi=\mathbf{1}$; and the eigenvalue condition (2.52). We can return to functions of τ by writing $\varphi=2\tau/V$ in the eigenvalues (2.54) and normalization factors (2.59), and by rescaling the energy denominator of Eq. (2.30) as per (2.50). The antisymmetric adiabatic coupling matrix Γ^τ in \mathbf{H}^{adi} becomes simply

$$\begin{aligned} \Gamma_{qq'}^\tau &= \pm \frac{2}{V} \frac{\left(\frac{d\lambda_q^\varphi}{d\varphi} \frac{d\lambda_{q'}^\varphi}{d\varphi} \right)^{1/2}}{\lambda_q^\varphi - \lambda_{q'}^\varphi} \delta_{qq'} \\ &= \pm \frac{\left(\frac{d\lambda_q^\tau}{d\tau} \frac{d\lambda_{q'}^\tau}{d\tau} \right)^{1/2}}{\lambda_q^\tau - \lambda_{q'}^\tau} \delta_{qq'}, \end{aligned} \quad (2.61)$$

where the minus sign applies only when $\tau > 0$ and either $q=0$ or $q'=0$ (see Appendix B).

Taken together, Eqs. (2.50) for E_q^τ and (2.61) for $\Gamma_{qq'}^\tau$ completely specify $\mathbf{H}^{\text{adi}}(\tau)=\mathbf{E}^\tau+i\Gamma^\tau$ at a fixed field or time in terms of the λ -scale eigenvalues $\{\lambda_q^\tau\}$ determined by Eqs. (2.52) and (2.56) [33]. The expression for $\Gamma_{qq'}^\tau$ is exact—for one nonzero μ_l and any l or m . [The result (2.54) applies only to the case $l=0$, however.] Note that in the first form of (2.61), the only dependence on V appears in the explicit factor $2/V$; the remaining function of the rescaled variable φ depends only on the quantum

numbers n , l , and m through Eq. (2.52).

In the symmetric case ($l=0$), the coupling among adiabatic levels follows from the eigenvalues $\{\lambda_q^\varphi\}$ given in Eqs. (2.54)–(2.56). Application of Eq. (2.61) involves

$$\Gamma_{qq'}^\tau = \frac{2}{V} \frac{\left[(q-q') + \frac{1}{\pi} \tan^{-1} \left[\frac{2\pi\delta_{qq'}}{(\varphi - \bar{\sigma}_{qq'})^2 + (\pi^2 - \delta_{qq'}^2)} \right] \right]^{-1}}{\{[(\varphi - \bar{\sigma}_{qq'})^2 + (\pi^2 - \delta_{qq'}^2)]^2 + (2\pi\delta_{qq'})^2\}^{1/2}}, \quad q, q' \neq 0, \quad (2.62)$$

where $\varphi = 2\tau/V$ and

$$\bar{\sigma}_{qq'} = \frac{1}{2}(\sigma_q + \sigma_{q'}), \quad \delta_{qq'} = \frac{1}{2}(\sigma_{q'} - \sigma_q). \quad (2.63)$$

Equation (2.62) is written in this form to emphasize two features. (1) The factor $1/\{\}^{1/2}$ is actually the geometric average of two Lorentzians having equal widths $\Delta\varphi = 2\pi$ but centers displaced in φ by $2|\delta_{qq'}|$. If the splitting is small and $|\delta_{qq'}| < \pi$, the radical is adequately approximated by a single Lorentzian of width $2(\pi + \delta_{qq'}^2/\pi)$. If $|\delta_{qq'}| > \pi$, on the other hand, a double-lobed structure appears; however, the definition (2.55) implies that this cannot occur until at least $n > e^\pi + 1 \approx 24$, when the edge states ($q=1$, $q'=n-1$) are sufficiently split. (2) $\Gamma_{qq'}^\tau$ includes an overall factor $(q-q'+\dots)^{-1}$. The arctangent term lies between 0 and $\frac{1}{2}$ if $|\delta_{qq'}| \leq \pi$ and never exceeds 1 if $|\delta_{qq'}| > \pi$; it can be ignored compared to $\Delta q = q' - q$. (That is, the factor $\lambda_q^\tau - \lambda_{q'}^\tau$ has a relatively small step-unstep variation from the constant value $q - q'$; cf. Fig. 4.)

Thus, the matrix element coupling pairs of $m=0$ manifold levels is localized in field roughly like a Lorentzian centered at $\tau = \frac{1}{2}V\bar{\sigma}_{qq'}$,

$$\Gamma_{qq'}^\tau \approx \frac{1}{q-q'} \left[\frac{\pi^{-1}(\frac{1}{2}\Delta\tau_{qq'})}{(\tau - \frac{1}{2}V\bar{\sigma}_{qq'})^2 + (\frac{1}{2}\Delta\tau_{qq'})^2} \right], \quad (2.64)$$

with FWHM

$$\Delta\tau_{qq'} = \pi V(1 + \delta_{qq'}^2/\pi^2). \quad (2.65)$$

The interaction strength scales like $(\Delta q)^{-1}$, with a maximum value given by

$$\Gamma_{qq'}^\tau(\text{maximum}) \approx \frac{1}{V} \frac{2/\pi^2}{q-q'} \quad (2.66)$$

and asymptotic form

$$\Gamma_{qq'}^\tau \rightarrow \frac{1}{2\Delta q} \frac{V}{\tau^2}, \quad |\tau| \gg V. \quad (2.67)$$

The quasi-Lorentzian behavior of the adiabatic coupling elements (2.64) is reminiscent of the exact two-level result for Γ_{-+} , Eq. (2.43)—a Lorentzian [30] with a FWHM that scales like $\Delta\tau \sim V$. Note that, although Eqs. (2.62)–(2.67) apply only when $|\delta_{qq'}| < \pi$, any double-humped element $\Gamma_{qq'}^\tau$ (for $|\delta_{qq'}| > \pi$) will be smaller than the largest $\Gamma_{qq'}^\tau$ (those with $|\Delta q|=1$) by at least a factor

derivatives $d\lambda_q^\varphi/d\varphi$ of the arctangent in (2.54), which yields Lorentzian-like factors $[\pi^2 + (\varphi - \sigma_q)^2]^{-1/2}$. One finds that the matrix element coupling any two members of the adiabatic manifold reduces to

$\sim 2n$ and therefore will be negligible.

The elements of Γ^τ are plotted as $V\Gamma_{qq'}^\tau$ vs $\varphi = 2\tau/V$ in Fig. 5 for $n=10$, $l=m=0$, and $q' > q$. This scaling produces a map of functions of field that is independent of V , i.e., of μ_l and \dot{F} . The functions shown in Fig. 5 were calculated via numerical diagonalization of \mathbf{H}^{diab} and direct construction of \mathbf{H}^{adi} in the manner of Eq. (2.30). All the positive matrix elements are those coupling the shifted level to the manifold levels, $\Gamma_{0q'}^\tau$; these are described below. The negative ones represent coupling among adiabatic manifold levels, Eq. (2.62); they are fairly well represented by Eq. (2.64). The latter fall into groups according to their values of $|\Delta q|$: the eight values most negative at $\tau \approx 0$ correspond to $|\Delta q|=1$, i.e., $\Gamma_{12}^\tau, \dots, \Gamma_{89}^\tau$. Successive groups of fewer levels correspond to $|\Delta q|=2, 3, \dots, 8$, the coupling Γ_{19}^τ being smallest in magnitude. As might be expected, the closer two levels are to one another, the more strongly they couple. However, the manifold levels are *degenerate* at $\tau=0$, so

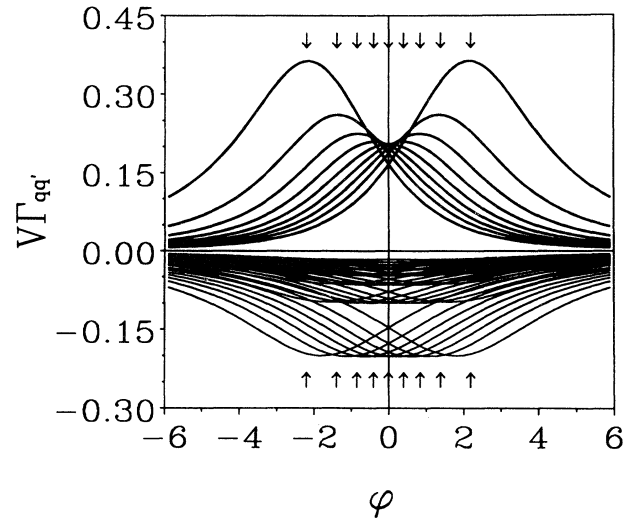


FIG. 5. Adiabatic-level couplings $V\Gamma_{qq'}^\tau$ vs φ , for same parameters as Fig. 4, and $q' > q$. Positive-valued curves: coupling to shifted level, $q=0$. Negative-valued curves: coupling within adiabatic manifold, $q \neq 0$ and $q' \neq 0$, $|q - q'| = 1, 2, \dots, 8$. Arrows: $\varphi = \sigma_q$, Eq. (2.55), approximately mark peaks of $\Gamma_{qq'}^\tau$. Scaling shown produces a μ_0 - and \dot{F} -independent coupling matrix Γ^τ . See the text.

“close” in this context refers to separation in the λ scale—not to an energy difference. Although the adiabatic manifold mimics the hydrogenic bowtie in appearance, the coupling Γ^τ produces behavior opposite to that of the diabatic bowtie: in the diabatic limit ($V \rightarrow 0$), a rapidly ramped field thoroughly mixes the adiabatic levels, whereas they remain unmixed in the adiabatic limit ($V \rightarrow \infty$).

It is not so straightforward to calculate $\Gamma_{0q'}^\tau$, since λ_ϕ^0 is a rather complex function of the other $\{\lambda_{q'}^\phi\}$ [cf. Eqs. (2.54)–(2.56)]. One could estimate the sum in (2.56), but even an analytical guess for λ_ϕ^0 must then be substituted into Eq. (2.61) along with the $\{\lambda_{q'}^\phi\}$ and their derivatives; the result is inevitably unwieldy [34]. We content ourselves here with noting the general appearance of the $q=0$ family in Fig. 5. Each member $\Gamma_{0q'}^\tau$ is a quasi-Lorentzian centered at $\tau \approx \frac{1}{2}V\sigma_{q'}$ ($\varphi \approx \sigma_{q'}$) with FWHM $\Delta\tau_{0q'} \approx 2V$. At $\tau=0$, λ_ϕ^0 is finite: in the limit $\tau \rightarrow 0$, the leading term of λ_ϕ^0 is $-n\varphi^{-1}$ and of its derivative is $d\lambda_\phi^0/d\varphi \rightarrow n\varphi^{-2}$. Equations (2.54) and (2.61) then imply

$$\Gamma_{0q'}^\tau \rightarrow \frac{1}{V} \frac{2}{[n(\pi^2 + \sigma_{q'}^2)]^{1/2}}, \quad \tau=0. \quad (2.68)$$

In particular, the level whose coupling to $q=0$ has the smallest peak value is $q' = \frac{1}{2}n$ (if n is even), for which $\sigma_{q'}=0$ and $\Gamma_{0n/2}^\tau = (2/\pi V)n^{-1/2}$ at $\tau=0$. Yet even this is larger than all the intermanifold couplings (2.66) when $n \leq 10$ (though smaller than some $|\Delta q|=1, 2, \dots$ couplings when $n > 10$). The very largest peak coupling belongs to the adiabatic edge states, $q'=n-1$ and $q'=1$, at $\tau \approx \pm V \ln \sqrt{n-1}$ (see Fig. 5). Most importantly, the maximum coupling for $m=0$ is found to have a scaled value [35], $V\Gamma_{01}^\tau = V\Gamma_{0n-1}^\tau \approx 0.35$, that is essentially *independent* of n . This is almost twice the largest possible *intra-manifold* value $V\Gamma_{qq'}^\tau = 2/\pi^2$ for $\Delta q=1$.

Ramping through the whole n manifold—at any \dot{F} —does not simply involve a sequence of independent Landau-Zener events. In light of Eq. (2.39), one would naively expect a ramped electric field to mix any pair of adiabatic levels to varying degrees in a kind of LZÉ. But the final probability distributions $P_{q \rightarrow q'}$ are ultimately complicated by the fact that the interactions $\Gamma_{qq'}^\tau$, though individually localized in field, completely overlap one another (see Fig. 5). In this sense, “scattering” from the bowtie is an inherently coherent, multilevel process.

One other factor to consider, suggested by the two-level-mixing picture, is the levels’ slope or “velocity” difference in the denominator of the Landau-Zener exponent in Eq. (2.39). This difference is smallest between adjacent manifold levels, which also have $\Delta q=1$ and the largest coupling; hence *adiabatic neighbors will undergo the most mixing by a ramped field*. The effect is even more pronounced for the shifted level, which in addition to having maximal coupling to the two adiabatic-manifold edge levels over a broad field range lies nearly parallel to them. [This corresponds to $s \approx 0$ in Eq. (2.43).] These facts will account for the tendency of an $m=0$ population initially in any one state q at $\tau_0 \ll 0$ to wind up predominantly in either the same state ($q'=q$) or one of its neighbors [36] ($q'=q \pm 1$) at $\tau \gg 0$, no matter what

the ramp rate. In particular, a $q=0, m=0$ level begun at $\tau_0 \ll 0$ will emerge at $\tau \gg 0$ in a mixture composed mostly of $q=0$ and the edge level $q=n-1$ (with some $q=1$).

III. THE TIME-EVOLUTION OPERATOR

The history of the Rydberg electron in the Schrödinger representation is contained in the state amplitudes $\{a_k(t)\}$ in Eq. (2.2), for a generic basis of $n-m$ states labeled k or k' . These amplitudes form a column vector $\mathbf{a}(t)$ that evolves in time according to the Schrödinger equation (2.3). Since at $t=t_0$ one may independently populate any one of the $n-m$ states, a complete description of $\Psi(t)$ requires the calculation of $n-m$ state vectors $\mathbf{a}_k(t)$, each representing the evolution of the system beginning in a different k state. The *propagator* or *time-evolution operator* $\hat{\mathbf{U}}$ in this representation is just the square, unitary matrix \mathbf{U} consisting of the column vectors $\{\mathbf{a}_k(t)\}$. This definition implies that a set of amplitudes $\mathbf{a}(t)$ at time t is generated from arbitrary initial conditions $\mathbf{a}(t_0)$ by

$$\mathbf{a}(t) = \mathbf{U}(t, t_0) \mathbf{a}(t_0), \quad (3.1)$$

while the initial conditions on \mathbf{U} are

$$\mathbf{U}(t_0, t_0) = \mathbf{1}. \quad (3.2)$$

$\mathbf{U}(t, t_0)$ also evolves according to the Schrödinger equation (2.3):

$$i \frac{d\mathbf{U}}{dt} = \mathcal{H}(t) \mathbf{U}, \quad (3.3)$$

where the time translation generator

$$\mathcal{H}(t) = \mathbf{H}(t) + i \langle \dot{\psi} | \tilde{\psi} \rangle \quad (3.4)$$

is a Hermitian matrix. \mathcal{H} functions as an effective Hamiltonian, its second term coming from the ramp’s effect on the basis states themselves (i.e., on the column vector $\dot{\psi}$; $\tilde{\psi}$ is a row vector). In the three bases introduced in Sec. II A, \mathcal{H} stands for one of the Hamiltonians: \mathbf{H}^{sph} [Eq. (2.7) and (2.8)], \mathbf{H}^{diab} [Eq. (2.15), (2.18), or (2.26)], or \mathbf{H}^{adi} [Eqs. (2.21) and (2.22), or (2.29) and (2.30)].

The formal solution of Eq. (3.3) is

$$\mathbf{U}(t, t_0) = \exp \left[-i \int_{t_0}^t dt' \mathcal{H}(t') \right]. \quad (3.5)$$

However, the usual interpretation of the integral as a limiting sum of actions $\mathcal{H}(t')dt'$ cannot obtain, since the Hamiltonian generally does *not* obey $[\mathcal{H}(t'), \mathcal{H}(t'')] = 0$ when $t' \neq t''$. Equation (3.5) holds only if \mathcal{H} is strictly constant in time or if variations in $\mathcal{H}(t)$ are so slow that the evolution is truly adiabatic [and the term with $d\psi/dt$ in (3.4) approaches zero]. The evolution must be represented instead by a sequence of transformations $\mathbf{U}(t + \Delta t, t)$ over small time steps Δt taken in the limit $\Delta t \rightarrow 0$, so that Eq. (3.5) applies but only over infinitesimal time intervals. This is the Riemann product representation [17] of $\mathbf{U}(t, t_0)$:

$$\begin{aligned} \mathbf{U}(t, t_0) &= \lim_{N \rightarrow \infty} \mathbf{U}(t_N, t_{N-1}) \cdots \mathbf{U}(t_2, t_1) \mathbf{U}(t_1, t_0) \\ &= \lim_{N \rightarrow \infty} \prod_{j=1}^N \exp \left[-i \int_{t_{j-1}}^{t_j} dt' \mathcal{H}(t') \right], \end{aligned} \quad (3.6)$$

where $t_N \equiv t$. The interval $[t_0, t]$ has been subdivided into N intervals of widths $\Delta t_j = t_j - t_{j-1}$ that satisfy $\sum_j \Delta t_j = t - t_0$; the subdivisions need not be equal. The method outlined below actually uses two levels of partitioning. The result (3.6) is exact [17] in the limit $\Delta t_j \rightarrow 0$ for all the finest-resolution time steps Δt_j .

In order to calculate $\mathbf{U}(\infty, -\infty)$ for a linear-ramp potential in Eq. (2.1), we first truncate the total time domain to $[t_0, |t_0|]$. The boundary $t_0 \ll 0$ is chosen to be so large that it lies outside the mixing region discussed in Sec. II C (see Fig. 5): i.e., $|\tau_0| \gg V$, $|t_0| \gg 2|\mu|/3\dot{F}n^5$. This is equivalent to the hydrogenic-limit condition (1.3). Thus, the time $t_0 = -F_{\max}/\dot{F}$ should correspond to a field F_{\max} where the Stark splitting greatly exceeds the largest core-induced level shift.

The practical implementation of Eq. (3.6) for a given generator $\mathcal{H}(t)$ now boils down to the following tasks.

(1) The entire interval $[t_0, |t_0|]$ is divided into a fixed set of N “macroscopic” steps $\{\Delta t_j\}$ tailored to gross variations in phases like $\int dt' [E_p(t') - E_{p'}(t')]$.

(2) Each macroscopic interval $[t_{j-1}, t_j]$ is further subdivided into $N'_j \geq 1$ “microscopic” intervals of width $\Delta' t_j = \Delta t_j / N'_j$. These must be small enough to ensure convergence of $\mathbf{U}(t_j, t_{j-1})$ —to a specified accuracy—over the j th macroscopic interval.

(3) Each microscopic interval $[t_a, t_b]$ (where $t_{j-1} \leq t_a < t_b = t_a + \Delta' t_j \leq t_j$) is assigned a unitary-matrix factor $\mathbf{U}(t_b, t_a)$, in analogy to the factors in the second line of (3.6). All N'_j such matrices are multiplied together to obtain $\mathbf{U}(t_j, t_{j-1})$ at the “current time” $t = t_j$. Each such (converged) macroscopic propagator is used in turn to update the time evolution operator to the current time:

$$\mathbf{U}(t, t_0) = \mathbf{U}(t, t_{j-1}) \mathbf{U}(t_{j-1}, t_0), \quad t = t_j. \quad (3.7)$$

(4) Evaluation of the anti-Hermitian matrix $[-i \int dt' \mathcal{H}(t')]$ over a microscopic interval is always accompanied by its exponentiation to yield the unitary factor $\mathbf{U}(t_b, t_a)$. The latter requires a diagonalization in analogy to Eq. (2.18), but here it applies to the *integral* of $\mathcal{H}(t)$, a Hermitian matrix:

$$\mathbf{M}(t_b, t_a) = \int_{t_a}^{t_b} dt' \mathcal{H}(t') = \mathbf{X} \mathbf{\Lambda} \mathbf{X}^\dagger, \quad (3.8)$$

so that

$$\mathbf{U}(t_b, t_a) = \exp[-i \mathbf{M}(t_b, t_a)] = \mathbf{X} e^{-i \mathbf{\Lambda}} \mathbf{X}^\dagger. \quad (3.9)$$

The columns of the unitary matrix \mathbf{X} contain the eigenvectors of \mathbf{M} , and the diagonal matrix $\mathbf{\Lambda}$ its (real) eigenvalues.

(5) Finally, the probability of beginning in any state k at $t = t_0 \rightarrow -\infty$ and ending in any state k' at $t = |t_0| \rightarrow \infty$ is

$$P_{k \rightarrow k'} = \lim_{t_0 \rightarrow -\infty} |U_{k'k}(|t_0|, t_0)|^2. \quad (3.10)$$

The results $P_{k \rightarrow k'}$ depend on the quantum numbers n and m , the atomic parameters $\{\mu_l\}$, and the experimentally controllable parameter \dot{F} ; these define a “given generator” $\mathcal{H}(t)$. Theoretically, we can vary the quantum defects and the ramp rate arbitrarily, but the number of independent parameters is actually one less. Since we are considering $P_{k \rightarrow k'}$ in the limit $|t_0|$ or $|\tau_0| \rightarrow \infty$, any time scale suffices. The rescaling (2.24) effectively fixes the ramp rate at unity, producing the dynamical equations (2.25) and (2.26) (in the diabatic basis). In general, the Hamiltonian

$$H_{pp'}^{\text{diab}}(\tau) = p \tau \delta_{pp'} - \sum_{l=m}^{n-1} V_l u_{pl} u_{p'l} \quad (3.11)$$

involves one parameter V_l per nonzero quantum defect, defined in Eq. (2.27). This means that at a given ramp rate \dot{F} there is a typical time scale $\Delta \tau_l \simeq O(V_l)$ for each l over which the adiabatic q states are dynamically coupled during the ramp. Consequently, the final-state probabilities $P_{q \rightarrow q'}(\dot{F})$ will exhibit general patterns extending over different scales in \dot{F} (see Sec. V).

Details of the numerical procedure for calculating $\mathbf{U}(|t_0|, t_0)$ are discussed in Appendix C, but two important refinements of the above tasks deserve mention here. The computationally most expensive step listed above is the matrix diagonalization (3.8). The total number of *microscopic* intervals visited at all stages of the calculation should therefore be minimized. But a desired level of accuracy over the j th macroscopic interval is attained by increasing the number N'_j of microscopic steps—thereby decreasing the step size $\Delta' t_j$ —until $\mathbf{U}(t_j, t_{j-1})$ is sufficiently converged. It is desirable to choose macroscopic step sizes and their microscopic subdivisions dynamically if possible, so convergence to the exact $\mathbf{U}(|t_0|, t_0)$ is optimized; see Appendix C. The other, more interesting refinement is discussed below in Sec. III A and in Appendix D, wherein *Magnus corrections* are employed to hasten the convergence of $\mathbf{U}(t_b, t_a)$.

Symmetries of $\mathbf{U}(t, t_0)$ further permit a halving of the computational effort required to obtain $\mathbf{U}(|t_0|, t_0)$. Precise analytical expressions for $\mathbf{U}(|t_0|, t_0)$ or $\mathbf{U}(\infty, -\infty)$ are otherwise elusive, though explicit expressions for $P_{p \rightarrow p'}(V)$ are available in the limits $V \rightarrow 0$ and $V \rightarrow \infty$; these results are presented in Sec. III B.

A. Magnus corrections

The time evolution operator for a microscopic interval is better approximated by Eq. (3.9) as the step size $\Delta' t_j = t_b - t_a$ decreases. However, the approximation can be improved for any finite interval $[t_a, t_b]$ by modifying the matrix $\mathbf{M}(t_b, t_a)$. The form of $\mathbf{M}(t_b, t_a)$ given in Eq. (3.8) is just its lowest-order form. Magnus corrections to $\mathbf{M}(t_b, t_a)$ allow $e^{-i \mathbf{M}}$ to converge much more rapidly to the exact $\mathbf{U}(t_b, t_a)$. Hence wider microscopic step sizes can be used and many fewer diagonalizations need to be performed *in toto*.

Magnus's approach [18,37] resembles a WKB-type approximation in t . Insertion of the ansatz (3.9) into the Schrödinger equation (3.3) leads to an equation for

$\mathbf{M}(t, t_a)$ [37]:

$$\frac{d\mathbf{M}}{dt} = \left[\frac{\mathbf{C}_M}{\exp(\mathbf{C}_M) - \mathbf{1}} \right] \mathcal{H}(t). \quad (3.12)$$

The operator \mathbf{C}_M effects commutation of a matrix with $-i\mathbf{M}$: $\mathbf{C}_M \mathbf{Z} = -i[\mathbf{M}, \mathbf{Z}]$, $\mathbf{C}_M^2 \mathbf{Z} = -[\mathbf{M}, [\mathbf{M}, \mathbf{Z}]]$, etc., where \mathbf{Z} is any square matrix the same size as \mathbf{M} . Expansion of the operator series inside the brackets and integration over $[t_a, t]$ yields

$$\begin{aligned} \mathbf{M}(t, t_a) &= \int_{t_a}^t dt' (\mathbf{1} - \frac{1}{2}\mathbf{C}_M + \frac{1}{12}\mathbf{C}_M^2 - \frac{1}{720}\mathbf{C}_M^4 + \dots) \mathcal{H}(t') \\ &= \int_{t_a}^t dt' \mathcal{H}(t') + i\frac{1}{2} \int_{t_a}^t dt' [\mathbf{M}(t', t_a), \mathcal{H}(t')] \\ &\quad - \frac{1}{12} \int_{t_a}^t dt' [\mathbf{M}(t', t_a), [\mathbf{M}(t', t_a), \mathcal{H}(t')]] \\ &\quad - \dots, \end{aligned} \quad (3.13)$$

where we have used the boundary condition $\mathbf{M}(t_a, t_a) = 0$ to match Eq. (3.2). This integral equation can be solved by recursive substitution of $\mathbf{M}(t, t_a)$ back into the integrals, which calls for a perturbation-series expansion for $\mathbf{M}(t, t_a)$:

$$\begin{aligned} \mathbf{M}(t, t_a) &= \mathbf{M}^{(1)}(t, t_a) + \mathbf{M}^{(2)}(t, t_a) \\ &\quad + \mathbf{M}^{(3)}(t, t_a) + \dots \end{aligned} \quad (3.14)$$

Substitution of this series into Eq. (3.13) and collection of terms according to their number of commutators gives each $\mathbf{M}^{(n)}(t, t_a)$ ($n \geq 1$) as an n -fold integral of products of n unequal-time matrices $\mathcal{H}(t')$. The $(n+1)$ th-order Magnus term essentially measures $\partial^n \mathcal{H} / \partial t^n$ via n unequal-time commutators—subsequent terms diminish according to the smoothness of $\mathcal{H}(t)$.

Explicit expressions for $\mathbf{M}^{(n)}(t, t_a)$ for an arbitrary generator $\mathcal{H}(t)$ can be found in Appendix D and in Refs. [18, 19]. Of special concern for the bowtie problem are Hamiltonians of the form

$$\mathcal{H}(t) = \mathbf{P} + F(t)\mathbf{Q} \quad (3.15)$$

with *time-independent* matrices \mathbf{P} and \mathbf{Q} . Both \mathbf{H}^{sph} and \mathbf{H}^{diab} have this structure, as does the Hamiltonian in any other basis obtained from the l or p bases by a time-independent transformation. [\mathbf{H}^{adi} , however, does not simplify in this way since \mathbf{c}^F in Eqs. (2.17)–(2.19) depends on $F(t)$.] With this structure, the multiple integrals of $\mathbf{M}^{(n)}(t, t_a)$ reduce to multiple integrals over a presumably known function $F(t)$. The multiple commutators of \mathbf{P} and \mathbf{Q} depend on neither t nor \dot{F} ; they can be computed once for given n , m , and $\{\mu_l\}$, and stored prior to all ramps through the manifold. Explicit expressions for $\mathbf{M}^{(n)}(t, t_a)$ of order $n = 1$ –3 in terms of integrals of $F(t')$ are also given in Appendix D.

The choice of a linear ramp $F(t) = \dot{F}t$ in Eqs. (3.13)–(3.15) implies

$$\begin{aligned} \mathbf{M}(t_b, t_a) &= (\mathbf{P} + \mathbf{Q}\dot{F}\bar{t})\Delta t + i[\mathbf{P}, \mathbf{Q}]\frac{1}{12}\dot{F}(\Delta t)^3 \\ &\quad - [[\mathbf{P}, \mathbf{Q}], \mathbf{Q}]\frac{1}{240}\dot{F}^2(\Delta t)^5 + O((\Delta t)^5) \end{aligned} \quad (3.16)$$

up to third order, where $\Delta t = t_b - t_a$ is the step size and

$\bar{t} = \frac{1}{2}(t_a + t_b)$ is the midinterval time. Notice that the term linear in Δt is just $\mathbf{M}^{(1)}(t_b, t_a) = \mathcal{H}(\bar{t})\Delta t$, i.e., the uncorrected integral of Eq. (3.8). All higher-order terms $\mathbf{M}^{(n)}(t_b, t_a)$ scale like $(\dot{F})^n \varrho(\Delta t)^{n_p + 2n_q}$ with $n = n_p + n_q$, where n_p and n_q are the numbers of factors of \mathbf{P} and \mathbf{Q} , respectively, in a term's commutator(s) (see Appendix D). The scaling with powers of Δt implies that higher Magnus corrections to $\int_{t_a}^{t_b} dt' \mathcal{H}(t')$ converge more rapidly as Δt decreases.

Equation (3.16) is the working formula in our calculations in the spherical and parabolic bases [38]. In the former case \mathbf{P} is diagonal [cf. Eq. (2.7)] whereas in the latter \mathbf{Q} is diagonal [cf. Eq. (3.11)]. The adiabatic basis requires instead multiple numerical integrations of $\mathcal{H}(t')$; hence calculations of $M_{q'q}(t_b, t_a)$ tend to be tedious and slow to converge. In any case, once $\mathbf{M}(t_b, t_a)$ is obtained for a microscopic interval $[t_a, t_b]$ it is diagonalized and used to construct $\mathbf{U}(t_b, t_a)$ as in Eqs. (3.8) and (3.9).

B. Symmetries and limiting cases of $\mathbf{U}(t, t_0)$

Symmetries of the time evolution operator can be exploited in computations to reduce the number of independent elements of \mathbf{U} . Specific relations among elements $U_{k'k}(t_2, t_1)$ may depend on the particular generator $\mathcal{H}(t)$, basis states (k', k) , or times t_1 and t_2 in question. We assume that $\mathcal{H}(t)$ conforms to the stricture

$$\mathcal{H}(-t) = \langle\langle \mathcal{H}(t) \rangle\rangle^* = \langle\langle \mathcal{H}(t) \rangle\rangle^T, \quad (3.17)$$

where \mathcal{H}^T is the transpose of \mathcal{H} . The special delimiters $\langle\langle \rangle\rangle$ have a dual purpose: they indicate multiplication of each row-column pairs of the enclosed matrix by an arbitrary phase factor, as well as possible permutation of the state labels $\{k\}$ (i.e., the rows *and* columns of the matrix) upon $t \leftrightarrow -t$. All of our Hamiltonians for the linear field— \mathbf{H}^{sph} , \mathbf{H}^{diab} , and \mathbf{H}^{adi} —obey Eq. (3.17) (see Appendix B).

We note three time-based symmetry operations on $\mathbf{U}(t_2, t_1)$. *Time reversal*, according to Eqs. (3.2) and (3.7), implies

$$\mathbf{U}(t_1, t_2) = [\mathbf{U}(t_2, t_1)]^{-1} = [\mathbf{U}(t_2, t_1)]^\dagger, \quad (3.18a)$$

where the interval $[t_1, t_2]$ is arbitrary here. The unitarity of \mathbf{U} follows of course from the hermiticity of \mathcal{H} in the Schrödinger equation (3.3): $\mathbf{U}^\dagger \mathbf{U} = \text{const} = \mathbf{1}$, so orthonormality of the state vectors persists [cf. Eq. (2.4)]. The *time parity* operation $t \rightarrow -t$ (and $t_0 \rightarrow -t_0$) applied to Eq. (3.3), (3.5), or the sequence of infinitesimal transformations (3.6) yields

$$\mathbf{U}(-t_2, -t_1) = \langle\langle \mathbf{U}(t_2, t_1) \rangle\rangle^*. \quad (3.18b)$$

A third operation combines the above two, whereby *time advances in the negative-time domain*:

$$\mathbf{U}(-t_1, -t_2) = \langle\langle \mathbf{U}(t_2, t_1) \rangle\rangle^T. \quad (3.18c)$$

Note that the validity of Eqs. (3.18b) and (3.18c) depends on the constraint (3.17) on $\mathcal{H}(\pm t)$, and can be verified with the help of Eqs. (3.8) and (3.9).

The relation (3.18c) renders calculation of $\mathbf{U}(|t_0|, t_0)$

unnecessary in one half of the time domain, since

$$\begin{aligned}\mathbf{U}(-t_0, t_0) &= \mathbf{U}(-t_0, 0)\mathbf{U}(0, t_0) \\ &= \mathbf{U}(-t_0, 0)\langle\langle \mathbf{U}(-t_0, 0) \rangle\rangle^T \\ &= \langle\langle \mathbf{U}(0, t_0) \rangle\rangle^T \mathbf{U}(0, t_0).\end{aligned}\quad (3.19)$$

(Recall that we take $t_0 < 0$.) Thus, a full traversal through the manifold can be completely described by a Riemann product of factors $\mathbf{U}(t_j, t_{j-1})$ [such as Eq. (3.6)] for macroscopic intervals restricted to either $t \geq 0$ or $t \leq 0$. Equation (3.19) further implies that $\mathbf{U}(|t_0|, t_0)$ and indeed $\mathbf{U}(\infty, -\infty)$ are symmetric unitary matrices—aside from some possible minus signs and a permutation of either rows or columns. When orthonormality is taken into account, the number of independent probabilities $P_{k \rightarrow k'}$, Eq. (3.10), is therefore $\frac{1}{2}(n-m)(n-m-1)$.

The permutation of indices consistent with (3.19) is the one that produces the *same energy ordering of levels* at $t > 0$ and $t < 0$. In the p basis, the reshuffling $p \leftrightarrow -p$ coupled with $t \leftrightarrow -t$ preserves the levels' order; e.g., for $n=6$ and $m=0$, the levels (2.10) that are labeled $p = \{5, 3, 1, -1, -3, -5\}$ at $t < 0$ map to $p' = \{-5, -3, -1, 1, 3, 5\}$, respectively, at $t > 0$ [see Fig. 1(b)]. Thus, the symmetry of $U_{p'p}(\infty, -\infty)$ generally implies

$$P_{p \rightarrow p'} = P_{-p' \rightarrow -p}. \quad (3.20)$$

Since the diabatic and adiabatic states coincide as $t \rightarrow \pm\infty$, the probabilities $P_{p \rightarrow p'}$ also represent $P_{q \rightarrow q'}$ when the proper identification between p and q bases is made at $t \ll 0$ and $t \gg 0$ (see Sec. II A and Fig. 1). The correspondences between q and q' depend on the number of quantum defects and their signs. The mapping for the six-level, single- μ_l example takes $q' = \{0, 1, 2, 3, 4, 5\}$ at $t > 0$ into $q = \{0, 5, 4, 3, 2, 1\}$ at $t < 0$. Then we have, e.g., $P_{0 \rightarrow 5} = P_{1 \rightarrow 0}$, $P_{5 \rightarrow 0} = P_{0 \rightarrow 1}$, $P_{0 \rightarrow 4} = P_{2 \rightarrow 0}$, $P_{5 \rightarrow 2} = P_{4 \rightarrow 1}$, and $P_{1 \rightarrow 1} = P_{5 \rightarrow 5}$, whereas $P_{0 \rightarrow 0}$, $P_{5 \rightarrow 1}$, $P_{4 \rightarrow 2}$, $P_{3 \rightarrow 3}$, $P_{2 \rightarrow 4}$, and $P_{1 \rightarrow 5}$ are all unique. The general rules for relating pairs of elements $P_{q \rightarrow q'}$ are easily inferred from the labeling of adiabatic levels standardized in Sec. II A. All the above relations are independent of \dot{F} .

Approximate analytical forms for $U_{p'p}(\infty, -\infty)$ can be obtained in the diabatic (zero core coupling) limit and, less precisely, for $U_{q'q}(\infty, -\infty)$ in the adiabatic (zero ramp rate) limit. The procedure is to start with an integral Schrödinger equation for $\mathbf{U}(t, t_0)$ and expand it in a Dyson series, in the spirit of Eqs. (3.12) and (3.13) for

$\mathbf{M}(t, t_0)$. The high- \dot{F} , low- V result will generalize the two-level result of Sec. II B.

Consider first the diabatic limit, where the parabolic basis is appropriate. In the τ scale the Schrödinger equation (3.3) for the general diabatic Hamiltonian (3.11) becomes

$$i \frac{d\mathbf{U}(\tau, \tau_0)}{d\tau} = [(\mathbf{p}\tau - \mathbf{v}) - \mathbf{V}]\mathbf{U}(\tau, \tau_0), \quad (3.21)$$

where we have split the core-coupling matrix in the p basis into diagonal (\mathbf{v}) and off-diagonal (\mathbf{V}) pieces:

$$\begin{aligned}v_{pp} \delta_{p'p} + V_{p'p} &= \sum_{l=m}^{n-1} u_{p'l} V_l u_{pl} \\ &= (\frac{3}{2}\dot{F}n)^{-1/2} n^{-3} \sum_{l=m}^{n-1} U_{p'l}^{(nm)} \mu_l \bar{U}_{lp}^{(nm)}.\end{aligned}\quad (3.22)$$

Following Eq. (2.34), we transform $\mathbf{U}(\tau, \tau_0)$ to the interaction representation:

$$\begin{aligned}\mathbf{U}(\tau, \tau_0) &= \exp[-i(\frac{1}{2}\mathbf{p}\tau^2 - \mathbf{v}\tau)] \mathbf{A}(\tau, \tau_0) \\ &= [\mathbf{A}(\tau, \tau)]^\dagger \mathbf{A}(\tau, \tau_0),\end{aligned}\quad (3.23)$$

which removes the diagonal elements of \mathbf{H}^{diab} . The appearance of the diagonal matrix of phases $\mathbf{A}(\tau, \tau)$ is a consequence of the boundary condition (3.2) [39]. Substituting $\mathbf{U}(\tau, \tau_0)$ into Eq. (3.21) and integrating over $[\tau_0, \tau]$ leads to

$$\begin{aligned}\mathbf{A}(\tau, \tau_0) &= \mathbf{A}(\tau_0, \tau_0) \\ &+ i \int_{\tau_0}^{\tau} d\tau_1 \exp[+i(\frac{1}{2}\mathbf{p}\tau_1^2 - \mathbf{v}\tau_1)] \\ &\quad \times \mathbf{V} \exp[-i(\frac{1}{2}\mathbf{p}\tau_1^2 - \mathbf{v}\tau_1)] \\ &\quad \times \mathbf{A}(\tau_1, \tau_0).\end{aligned}\quad (3.24)$$

This is the analog of Eq. (2.36) for many levels and any number of quantum defects. Substituting the time-evolution matrix $\mathbf{A}(\tau, \tau_0)$ back into the integral in Eq. (3.24) and iterating indefinitely yields an infinite-series solution for $\mathbf{A}(\tau, \tau_0)$ generated by $\mathbf{A}(\tau_0, \tau_0)$. Left-multiplying Eq. (3.24) by $[\mathbf{A}(\tau, \tau)]^\dagger$ gives $\mathbf{U}(\tau, \tau_0)$, Eq. (3.23). Each element $U_{p'p}(\tau, \tau_0)$ is thus proportional to a phase factor $[A_{p'p}(\tau, \tau)]^\dagger A_{pp}(\tau_0, \tau_0)$ which is irrelevant to the final probability $P_{p \rightarrow p'}$. Setting the upper integration limit to $\tau = |\tau_0|$ and taking the limit $\tau_0 \rightarrow -\infty$ yields

$$\begin{aligned}\langle\langle \mathbf{U}(\infty, -\infty) \rangle\rangle &= \mathbf{1} + i \int_{-\infty}^{\infty} d\tau_1 e^{+i(\mathbf{p}\tau_1^2/2 - \mathbf{v}\tau_1)} \mathbf{V} e^{-i(\mathbf{p}\tau_1^2/2 - \mathbf{v}\tau_1)} \\ &\quad - \int_{-\infty}^{\infty} d\tau_1 e^{+i(\mathbf{p}\tau_1^2/2 - \mathbf{v}\tau_1)} \mathbf{V} e^{-i(\mathbf{p}\tau_1^2/2 - \mathbf{v}\tau_1)} \int_{-\infty}^{\tau_1} d\tau_2 e^{+i(\mathbf{p}\tau_2^2/2 - \mathbf{v}\tau_2)} \mathbf{V} e^{-i(\mathbf{p}\tau_2^2/2 - \mathbf{v}\tau_2)} + \dots,\end{aligned}\quad (3.25)$$

with no permutations implied. The integrals in Eq. (3.25) are evaluated in Appendix B. Terms of third and higher order cannot, in general, be evaluated analytically.

The simplest case considered in Sec. II has one nonzero

quantum defect for $l=m=0$. All diagonal elements v_{pp} and nondiagonal elements $V_{p'p}$ in Eqs. (2.26) and (2.27) then equal V_0 , so all factors $e^{\pm iV\tau}$ cancel out. Equation (3.25) for $l=0$ explicitly reduces, to within a phase, to

(see Appendix B)

$$\begin{aligned}
U_{p'p}(\infty, -\infty) &= \delta_{p'p} + iV\delta_{p'p} \frac{\sqrt{2\pi i}}{\sqrt{p'-p}} \\
&\quad - V^2 \sum_s \delta_{p's} \delta_{sp} \frac{\pi i}{\sqrt{(p'-s)(s-p)}} \\
&\quad + O((\sqrt{\pi}V)^3) \quad (3.26)
\end{aligned}$$

for any values of p and p' . (The summation variable s ranges over all allowed values of p or p' with $\Delta s = 2$.) In particular, the elements with $p' = p$ represent *adiabatic transitions*:

$$U_{pp}(\infty, -\infty) = 1 - \pi V^2 \sum_{s \neq p} \frac{1}{|s-p|} + O(\pi^2 V^4). \quad (3.27)$$

The probabilities (3.10) for nondiabetic transitions ($p' \neq p$) are therefore

$$\begin{aligned}
P_{p \rightarrow p'}(V) &= \pi V^2 \frac{2}{|p'-p|} \\
&\quad \mp (\sqrt{\pi}V)^3 \frac{2}{\sqrt{|p'-p|}} (\Sigma_1 - \Sigma_2 + \Sigma_3) \\
&\quad + O((\sqrt{\pi}V)^4), \quad p' \leq p, \quad (3.28)
\end{aligned}$$

where

$$\Sigma_1 = \sum_{s < \min(p, p')} |(s-p)(s-p')|^{-1/2}, \quad (3.29a)$$

$$\Sigma_2 = \sum_{\min(p, p') < s < \max(p, p')} |(s-p)(s-p')|^{-1/2}, \quad (3.29b)$$

$$\Sigma_3 = \sum_{s > \max(p, p')} |(s-p)(s-p')|^{-1/2}, \quad (3.29c)$$

and any of these sums vanishes by convention if it has a null range. The adiabatic transition probabilities can be obtained from $P_{p \rightarrow p} = 1 - \sum_{p' \neq p} P_{p \rightarrow p'}$ and Eq. (3.28):

$$P_{p \rightarrow p}(V) = 1 - \pi V^2 \sum_{s \neq p} \frac{2}{|s-p|} + O(\pi^2 V^4). \quad (3.30)$$

The term of order $(\sqrt{\pi}V)^3$ involves a double summation that vanishes upon interchange of its dummy indices; this shows that the third-order term is correctly missing from Eq. (3.27). In fact, the entire series is *even* in V for adiabatic transitions:

$$P_{p \rightarrow p}(-V) = P_{-p \rightarrow -p}(V) = P_{p \rightarrow p}(V). \quad (3.31)$$

The first equality follows because the joint operations $\{\mu_l\} \rightarrow \{-\mu_l\}$ and $\tau \rightarrow -\tau$ leave Eq. (3.21) unchanged while (3.20) identifies $\tau \rightarrow -\tau$ with $P_{p \rightarrow p} \rightarrow P_{-p \rightarrow -p}$.

Fast enough ramp rates or weak atomic cores always result in transition probabilities of order $\pi V^2 = 2\pi\mu_0^2/(3\dot{F}n^9)$ as $V \rightarrow 0$, except for the adiabatic transitions, which have $P_{p \rightarrow p} = 1 - O(\pi V^2)$. [The corresponding limits for the q basis are given in Eq. (2.45a).] A tableau of the series coefficients in Eqs. (3.28)–(3.30) for $n = 8$ and $m = 0$, good up to third order as $V \rightarrow 0$, appears in Table I. Notice that transitions between states are more likely for neighboring levels, and especially that the cubic term hints at higher- V behavior by enhancing adiabatic transitions [e.g., $n_1 = 7 \rightarrow n'_1 = 0$ ($q = 0 \rightarrow q' = 0$) and $n_1 = 6 \rightarrow n'_1 = 7$ ($q = 7 \rightarrow q' = 7$)] at the expense of others. Note also that for $n = 2$ only values $p, p' = \pm 1$ would occur: Eqs. (3.28)–(3.30) imply $P_{p \rightarrow p'} = \pi V^2 + O(\pi^2 V^4)$ if $p' \neq p$, because the sums Σ_i all vanish, and $P_{p \rightarrow p} = 1 - \pi V^2 + O(\pi^2 V^4)$. These are, of course, the leading terms from the exact two-level result (2.41) for the LZE.

The most general expression good to second order essentially involves the replacement of V^2 above with squared elements of the matrix \mathbf{V} [Eq. (3.22)]. From the first integral in Eq. (3.25) we have

TABLE I. Low-order series-expansion coefficients of the transition probabilities $P_{p \rightarrow p'}(V_0)$ or $P_{q \rightarrow q'}(V_0)$, Eqs. (3.28)–(3.30), for $n = 8$, $m = 0$, and $\mu_0 > 0$. Row numbers at left, initial $n_1(q)$; columns, final $n'_1(q')$; note that $p = 2n_1 - 7$ and $p' = 2n'_1 - 7$. Shown are coefficients of πV_0^2 and (in brackets) $(\sqrt{\pi}V_0)^3$.

$n_1(q) \backslash n'_1(q')$	0(0)	1(1)	2(2)	3(3)	4(4)	5(5)	6(6)	7(7)
0(1)	-2.593 [0]	1.000 [+1.389]	0.500 [+0.281]	0.333 [-0.071]	0.250 [-0.248]	0.200 [-0.361]	0.167 [-0.449]	0.143 [-0.542]
1(2)	1.000 [-1.389]	-3.450 [0]	1.000 [+1.780]	0.500 [+0.485]	0.333 [+0.056]	0.250 [-0.167]	0.200 [-0.316]	0.167 [-0.449]
2(3)	0.500 [-0.281]	1.000 [-1.780]	-3.783 [0]	1.000 [+1.940]	0.500 [+0.560]	0.333 [+0.089]	0.250 [-0.167]	0.200 [-0.361]
3(4)	0.333 [+0.071]	0.500 [-0.485]	1.000 [-1.940]	-3.917 [0]	1.000 [+1.986]	0.500 [+0.560]	0.333 [+0.056]	0.250 [-0.248]
4(5)	0.250 [+0.248]	0.333 [-0.056]	0.500 [-0.560]	1.000 [-1.986]	-3.917 [0]	1.000 [+1.940]	0.500 [+0.485]	0.333 [-0.071]
5(6)	0.200 [+0.361]	0.250 [+0.167]	0.333 [-0.089]	0.500 [-0.560]	1.000 [-1.940]	-3.783 [0]	1.000 [+1.780]	0.500 [+0.281]
6(7)	0.167 [+0.449]	0.200 [+0.316]	0.250 [+0.167]	0.333 [-0.056]	0.500 [-0.485]	1.000 [-1.780]	-3.450 [0]	1.000 [+1.389]
7(0)	0.143 [+0.542]	0.167 [+0.449]	0.200 [+0.361]	0.250 [+0.248]	0.333 [+0.071]	0.500 [-0.281]	1.000 [-1.389]	-2.593 [0]

TABLE II. Lowest-order series-expansion coefficients of the transition probabilities $P_{p \rightarrow p'}(\dot{F})$ or $P_{q \rightarrow q'}(\dot{F})$, Eq. (3.32), for $n=8$, $m=0$, and $\mu_1 > 0$. Row and column numbers same as Table I. Shown are coefficients of πV_1^2 .

$n_1(q) \backslash n_1'(q')$	0(0)	1(1)	2(2)	3(3)	4(4)	5(5)	6(6)	7(7)
0(1)	-4.783	2.778	0.500	0.037	0.028	0.200	0.463	0.778
1(2)	2.778	-4.209	0.510	0.028	0.019	0.128	0.283	0.463
2(3)	0.500	0.510	-1.430	0.020	0.010	0.061	0.128	0.200
3(4)	0.037	0.028	0.020	-0.145	0.002	0.010	0.019	0.028
4(5)	0.028	0.019	0.010	0.002	-0.145	0.020	0.028	0.037
5(6)	0.200	0.128	0.061	0.010	0.020	-1.430	0.510	0.500
6(7)	0.463	0.283	0.128	0.019	0.028	0.510	-4.209	2.778
7(0)	0.778	0.463	0.200	0.028	0.037	0.500	2.778	-4.783

$$P_{p \rightarrow p'}(\dot{F}) \approx \begin{cases} \frac{4\pi}{3\dot{F}n^9} \frac{\left[\sum_l \mu_l u_{p'l} u_{pl} \right]^2}{|p'-p|}, & p' \neq p, \\ 1 - \frac{4\pi}{3\dot{F}n^9} \sum_{s (\neq p)} \frac{\left[\sum_l \mu_l u_{sl} u_{pl} \right]^2}{|s-p|}, & p' = p \end{cases} \quad (3.32)$$

(Appendix B), which applies to any manifold with any quantum defects as $\dot{F} \rightarrow \infty$. Table II shows the coefficients of $\pi V_1^2 = 2\pi\mu_1^2 / (3\dot{F}n^9)$ for $n=8$, $m=0$, and μ_l nonzero only for $l=1$ instead of $l=0$. In contrast to the $l=0$ case of Table I, there is larger coupling between edge states ($|p| \rightarrow n$) here and an absence of coupling to midmanifold states ($|p| \approx 0$) (see Appendix A). This shows up as an enhancement (diminishment) of popula-

tion transfer to and from states of higher (lower) $|p|$, as compared to the uniform-coupling $l=0$ case. States of higher m and small $l-m$ would display the opposite trend—favoring transfer among midmanifold states and disfavoring outer states.

In the adiabatic limit, $\dot{F} \rightarrow 0$, we use the Hamiltonian \mathbf{H}^{adi} [Eq. (2.29) or (2.30)] for \mathcal{H} in a τ -scaled Schrödinger equation (3.3). The diagonal matrix $\mathbf{E}(\tau)$ of eigenvalues E_q^τ is removed via the substitution

$$\mathbf{U}(\tau, \tau_0) = \exp \left[-i \int_0^\tau d\tau' \mathbf{E}(\tau') \right] \mathbf{B}(\tau, \tau_0), \quad (3.33)$$

where the lower integration limit $\tau'=0$ is arbitrary but accords with (3.23) [39]. In analogy to Eqs. (3.23)–(3.25), we can obtain series for $\mathbf{B}(\tau, \tau_0)$ and $\mathbf{U}(\infty, -\infty)$ in powers (and integrals) of the off-diagonal coupling matrix $i\Gamma(\tau)$. The lowest two terms have elements

$$U_{q'q}(\infty, -\infty) = \delta_{q'q} + \int_{-\infty}^{\infty} d\tau_1 \Gamma_{q'q}(\tau_1) \exp \left[+i \int_0^{\tau_1} d\tau' [\mathbf{E}_{q'}(\tau') - \mathbf{E}_q(\tau')] \right] \quad (3.34)$$

to within a phase factor. The explicit dependence of (3.34) on V emerges from introducing the φ scale (2.51), the λ scale (2.50), and the V -independently scaled couplings $\frac{1}{2}V\Gamma_{q'q}$ in Eq. (2.61), which depend only on the eigenvalues $\{\lambda_q(\varphi)\}$:

$$U_{q'q}(\infty, -\infty) = \delta_{q'q} + \int_{-\infty}^{\infty} d\varphi \left[\frac{1}{2}V\Gamma_{q'q}(\varphi) \right] \exp \left[+i \frac{1}{2}V^2 \int_0^\varphi d\varphi' [\lambda_{q'}(\varphi') - \lambda_q(\varphi')] \right]. \quad (3.35)$$

Thus, in the limit $V \rightarrow \infty$, $P_{q \rightarrow q'}$ approaches $\delta_{q'q}$ not as a power of V^{-1} but rather through a term that vanishes on account of the rapidly oscillating phase factor [40].

IV. NUMERICAL RESULTS—ONE QUANTUM DEFECT

We first present results for the MLZE induced by just one nonzero quantum defect, $\mu_1 > 0$. Calculations of $\mathbf{U}(\tau, \tau_0)$ and $\mathbf{U}(|\tau_0|, \tau_0)$ for manifolds with n ranging from 2 to 96 were carried out on the University of Kentucky's IBM 3090 using the code TIMEPASS. Time evolution matrices \mathbf{U} and \mathbf{M} for microscopic intervals, as prescribed in Sec. III, were normally constructed in the p basis, although their accumulations $\mathbf{U}(\tau, \tau_0)$ and $\mathbf{U}(|\tau_0|, \tau_0)$ were

normally output in the q basis via transformations (2.19). Each “pass” through an n manifold—i.e., each ramp from $\tau=\tau_0$ to $|\tau_0|$ at a fixed value of \dot{F} or $V=V_l$ —typically required a total of 500–1000 microscopic steps (1000–2000 matrix diagonalizations) for adequate convergence of $\mathbf{U}(|\tau_0|, \tau_0)$ to $\mathbf{U}(\infty, -\infty)$. (Issues of convergence and optimization are addressed in Appendix C.) Since the adiabatic levels are significantly coupled only at $|\tau| \lesssim 3V$ (Fig. 5), the initial rescaled time was usually taken in the range $\tau_0 = -10$ to -20 , depending on n and V .

Most of the following results are presented as families of probability curves $P_{q \rightarrow q'}$ vs V with common initial adiabatic states q [based on the definition (3.10)]. Recall that V^2 measures joint variations in the combination of parameters $|\mu_1|^2 n^{-9} / \dot{F}$. We consider the simple $l=m=0$ case in Secs. IV A–IV C. Note that the accuracy of the

calculations and results displayed here is always much better than the graphical resolution of the figures.

A. Time dependence of $U(\tau, \tau_0)$

The time development of the adiabatic-level populations tends to follow the simple $n=2$ patterns of Fig. 2(b). Figures 6(a) and 6(b) show representative multilevel versions of the probabilities $|U_{q'q}(\tau, \tau_0)|^2$ vs τ , in this case for $n=6$, $m=0$, and $\tau_0=-3$. In Fig. 6(a), a relatively fast ramp rate is represented by $V=0.3$; in Fig. 6(b), a slower ramp rate [41] is effected by $V=0.5$. The initial states are, respectively, (a) $q=0$ and (b) $q=5$, and the population of every state q' at time τ is marked with that state's number. The appropriate labeling of adiabatic levels q or $q'=0, \dots, 5$ for $n-m=6$ is shown in Fig. 1(b), which is reproduced as an inset in each figure.

The population in Fig. 6(a) is initially in the diabatic edge state $p=+5$ ($n_1=5$) at $\tau=\tau_0$, which is actually the shifted adiabatic level $q=0$. One expects that a rapid enough field ramp would favor the diabatic transition $p=+5 \rightarrow p'=+5$, i.e., $q=0 \rightarrow q'=5$. This is indeed the case: most of the $q=0$ population (52.4%) is ultimately

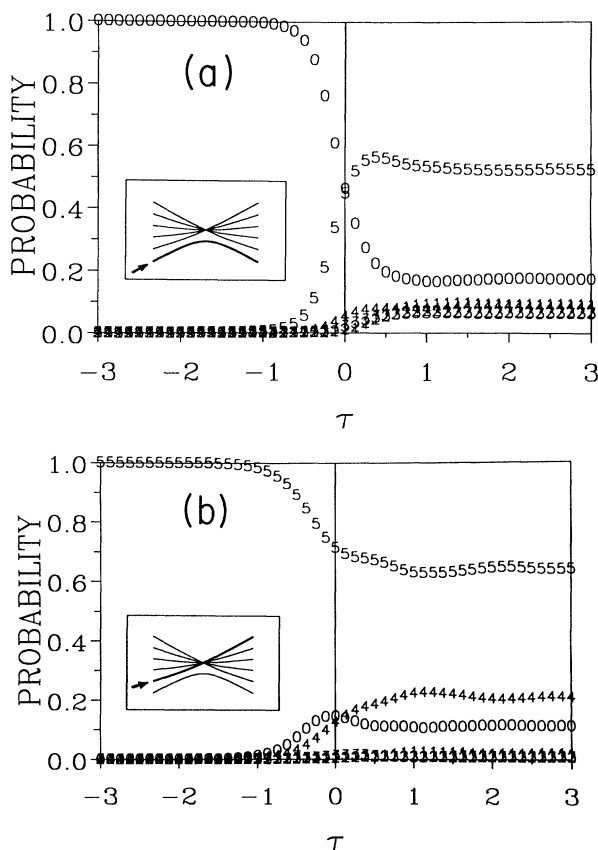


FIG. 6. Time evolution for $n=6$, $m=0$ manifold beginning at $\tau_0=-3$ in state (a) $q=0$ with $V=0.3$, and (b) $q=5$ with $V=0.5$. Population of adiabatic state q' is indicated by the number q' . Insets: $n=6$ bowties [cf. Fig. 1(b)]; thick line is initial adiabatic level q .

transferred to $q'=5$, whereas the adiabatic transition ($q=0 \rightarrow q'=0$) occurs with only 17.3% probability. There also arises a modicum (8.3%) of $q'=4$ (and a hint of $q'=3$ and 2) in the vicinity of $\tau \approx 0$, on the heels of the $q'=5$ buildup, while a comparable amount of $q'=1$ (9.0%) comes in at $\tau > 0$.

Recall that the shifted level $q=0$ is most strongly coupled to the adiabatic-manifold edge levels $q'=5$ and 1, the former at $\tau < 0$ and the latter at $\tau > 0$ (see Sec. II C, Fig. 5). Following the first half of the pass, much of the initial population has already gone to $q'=5$, leaving little to transfer to $q'=1$ on the way out. The ancillary growth of $q'=4 \rightarrow 3 \rightarrow 2$ is a consequence of successive nearest-neighbor couplings within the adiabatic manifold. It is reasonable to suppose that these extra levels could be enhanced by making a slower pass (higher V), but in fact no choice of V accomplishes this.

In Fig. 6(b) the initial state is the lower adiabatic edge state $q=5$ (i.e., $p=+3$ or $n_1=4$) at $\tau=\tau_0$. The adiabatic transition $q=5 \rightarrow q'=5$ now leads to the upper adiabatic edge state at $\tau \gg 0$, while the diabatic transition $p=+3 \rightarrow p'=+3$ ($q=5 \rightarrow q'=4$) steps one level away from the edge of the manifold. Figure 6(b) shows that, as in 6(a), the coupling between states $q'=0$ and 5 dominates at negative τ . Also present is the nearest-neighbor interaction between $q=5$ and $q'=4$ —which persists into the positive- τ domain and leads to the rise of $q'=4$. At this slower ramp rate the adiabatic level ($q'=5$) tops out at 64.4%, while its diabatic neighbor ($q'=4$) comes out with 20.9%—more than the other neighbor ($q'=0$, with 11.3%). The remaining manifold levels ($q'=1, 2, 3$) do not gain significantly.

Many other examples could be given but the essential features of $|U_{q'q}(\tau, \tau_0)|^2$, and hence of $P_{q \rightarrow q'}$, emerge from Fig. 6.

(1) All coupling and population transfer among adiabatic levels are approximately confined within the domain $|\tau| \lesssim 2V$, as anticipated in Sec. II.

(2) The adiabatic-level populations nearly converge to their limiting values $P_{q \rightarrow q'}(V)$ by about $\tau \approx 5V$, with mild and quickly decaying oscillations about those values. A representation of the populations in the diabatic basis, on the other hand, would reveal a multilevel version of the state-flopping oscillations seen in Fig. 2(a), which we refrain from showing here. Such oscillations tend to be complicated, of large amplitude, and slow to converge to the same set of values $P_{q \rightarrow q'}(V)$.

(3) For any initial q (n_1) and any coupling or ramp parameter V , the dominant final-state population belongs either to $q'=q$ or $n'_1=n_1$ (i.e., $p'=p$) and accounts for at least 35% of the total (if $n > 2$). That is, the most probable transition is always either the adiabatic one ($P_{q \rightarrow q}$) or the diabatic one ($P_{p \rightarrow p}$).

(4) The probability of transitions to any of the other $n-2$ levels from a given q is likely to attain 10–15% only for the other (nonadiabatic) nearest neighbor [36] to q . Any of the remaining $n-3$ levels reaches at most a few percent.

The above statements hold for all n and m (if we take

$l=m$ for $\mu_l \neq 0$). The first two hold as well for two or more quantum defects if we use in V the largest $|\mu_l|$; and even the last two statements apply within various ranges of V (see Sec. V).

B. Patterns in $P_{q \rightarrow q'}$ for $l=m=0$

Each initial state q leads to a family of *final-state probability curves* $P_{q \rightarrow q'}(V)$ that depend only on V . There are altogether n^2 such curves for $m=0$ but only $\frac{1}{2}n(n-1)$ of them are independent (cf. Sec. III B). The pattern of each family of curves varies only mildly as one picks different starting q 's within the adiabatic manifold; the edge states, $q=1$ and $q=n-m-1$, exhibit the most obvious deviations. However, the special state $q=0$ produces distributions $P_{0 \rightarrow q'}(V)$ that are quite dissimilar to the others, particularly in the slow-ramp, high- V limit. Furthermore, curves describing the edge-state populations quickly reach limiting forms as n grows (beyond $n=6$, say), if V is properly rescaled (Sec. IV C).

The six sets of probability curves for $n=6$, $m=0$ are plotted in Figs. 7(a)–7(f) for $q=\{0,5,4,3,2,1\}$, respectively. (This ordering corresponds to lowest-to-highest energy levels at $\tau < 0$.) The functions $P_{q \rightarrow q'}(V)$ are again marked by q' . Insets illustrate the various passes through the bowtie.

The most obvious feature of every plot is the pair of curves representing diabatic and adiabatic transitions from each q [36]. The two curves $P_{0 \rightarrow 5}$ and $P_{0 \rightarrow 0}$ for $q=0$ [Fig. 7(a)] closely resemble the Gaussian $n=2$ curves in Fig. 3 because of their drastic convergence to zero and one at large V . The apparently purely exponential behavior in the limit of very slow ramp rates is unique to transitions from the shifted level. The diabatic-transition curves for $q \neq 0$ drop off much more slowly as the initial state is taken closer to the center of the manifold [except $P_{1 \rightarrow 0}$, which is identical to $P_{0 \rightarrow 5}$; cf. the discussion below Eq. (3.20)]. Similarly, the probability of making an adiabatic transition through the middle of the manifold still rises to unity, but sluggishly compared to transitions along the adiabatic edge states.

All the nondiabatic and nonadiabatic transitions generally add up to less than $\frac{1}{3}$ of the total final-state population. The largest recipient amongst these is usually the “other” nearest neighbor [36]—especially at intermediate and slow ramp rates, e.g., $V > 0.4$. The behavior of the shifted level is once more exceptional, as $P_{0 \rightarrow 1}$ and $P_{5 \rightarrow 0}$ (which are equal) die off rapidly at $V > 0.4$. For initial states $q=1-4$ (i.e., those well removed from $q=0$), on the other hand, the buildup of other-neighbor populations persists out to much slower ramp rates, even $V > 1.5$. Figures 7(c) and 7(d) indicate that this effect, for $q \rightarrow q' = q+1$, peaks for transitions between *midmanifold* states.

These high- V results are reasonable in light of the adiabatic coupling terms $\Gamma_{qq'}^\tau$ in Eq. (2.61) (see Fig. 5), which universally scale like $1/V$. Each of the initial states $q=2, 3$, and 4 has both its nearest neighbors $q'=q \pm 1$ embedded in the adiabatic manifold, and couples to both of them throughout most of its passage through the

bowtie. When \dot{F} is slow enough, they are in fact populated equally: at $V \approx 1.5$ in Fig. 7, one observes (c) $P_{4 \rightarrow 5} \approx P_{4 \rightarrow 3}$, (d) $P_{3 \rightarrow 4} \approx P_{3 \rightarrow 2}$, and (e) $P_{2 \rightarrow 3} \approx P_{2 \rightarrow 1}$, and even (a) $P_{0 \rightarrow 1} \approx P_{0 \rightarrow 5}$. The cases (b) $q=5$ and (f) $q=1$ are somewhat odd because during each half of the pass one of them becomes the topmost level, which has only one neighbor to couple to. Hence $P_{5 \rightarrow 0}$ dies away feebly compared to $P_{5 \rightarrow 4}$ at $V \gtrsim 0.6$, as does $P_{1 \rightarrow 0}$ compared to $P_{1 \rightarrow 2}$.

In the fast-ramp limit, the probabilities $P_{q \rightarrow q'}(V)$ accord with the analytical results derived in Eqs. (3.28)–(3.30), although this is not discernible in Fig. 7. In particular, *all probabilities deviate from their $V=0$ values by terms of order πV^2* . When indexed as $P_{p \rightarrow p'}$, the greatest population transfer to other diabatic levels ($p \rightarrow p' \neq p$) occurs for $p'=p \pm 1$, the next largest for $p'=p \pm 2$, etc. (cf. Table I). This diabatic-level behavior for $V \rightarrow 0$ complements the adiabatic-level behavior for $\dot{F} \rightarrow 0$ discussed above.

The tenacity with which the (a) diabatic or (b) adiabatic levels remain populated when subject to some coupling or ramp V is illustrated in Figs. 8(a) and 8(b) for a larger manifold, $n=24$. Here we plot (a) $P_{p \rightarrow p}$ vs p and (b) $P_{q \rightarrow q}$ vs q as circles; those symbols connected by straight lines refer to one of the constant values of V in the range 0.1–1.0, or the extra-slow value 1.5 (thick lines). Thus, under the fastest ramp rate ($V=0.1$) the probability of making a diabatic transition is fairly uniform (at 85%) across most of the manifold, with a slight preference for diabaticity evident towards the manifold edges. Under the same ramp rate, the probability of making an adiabatic transition is quite flat (at 4%) across the entire *adiabatic submanifold* ($q=1-23$) but negligible for the shifted level ($q=0$) [42].

Under the slowest ramp rate ($V=1.5$), diabatic transitions are enhanced towards the manifold's center, while adiabatic transitions are likelier towards the manifold's edges. Note how the lone shifted level, the worst at making fast adiabatic transitions, becomes the best at slow ones. Intermediate values ($V=0.2-0.6$) represent the crossover region between effectively fast and slow ramp rates (cf. Fig. 7). The disparity across the manifold for transition probabilities at a fixed V is greatest in this range: e.g., at $V=0.5$ and 0.6 , the preference for adiabatic transitions at the edges over that at the center surpasses 28% (at $q=1$ and 23) and 42% (at $q=0$). This is attributable to the fewer number of levels in the neighborhood of the adiabatic manifold's edge. That is, there are more paths $q \rightarrow q_1 \rightarrow q_2 \cdots \rightarrow q' \neq q$ by which a central adiabatic level q can arrive at another level q' via the couplings $\Gamma_{qq'}^\tau$, so $P_{q \rightarrow q}$ is lowest in the center and highest at the edges.

C. Variations with n —the MLZE

The question arises as to whether the functions $P_{q \rightarrow q'}(V)$, in the limit $n \rightarrow \infty$, retain the general properties inferred above. It is impractical to consider results for all q for large- n manifolds. Within the adiabatic manifold, members $q=1$, $[\frac{1}{2}n]$, and $n-1$ will suffice to represent variations from one edge across the middle to

the opposite edge.

The case $q=0$ merits special attention. The probabilities for diabatic and adiabatic transitions from $q=0$ are plotted in Fig. 9(a) for $n=2$ (heavy solid lines), $n=3$, and successive doublings [43] $n=6, 12, 24, 48$, and 96 . The rise of all the adiabatic curves $P_{0 \rightarrow 0}(V)$ with increasing V mimics the $n=2$ curve, as does their rapid convergence to unity. There is, furthermore, a shift of the higher- n curves towards lower V , accompanied by some suppression of the probabilities at the low- V end [44]. The diabatic curves $P_{0 \rightarrow n-1}(V)$ also imitate the $n=2$ pattern, with a similar shift to lower V . In fact, Fig. 9(a) is con-

sistent with the possibility that the latter all have precisely the *same* shape, namely, that of a *Gaussian* in V . There is strong numerical evidence that this is indeed true, but a rigorous proof is not yet available.

Consider the following.

Conjecture: In an isolated n manifold with $m=0$, $\mu_0 \neq 0$, and $\mu_l=0$ for $l>0$, the *outer diabatic transition* $q=0 \rightarrow q'=n-1$ (i.e., $p=n-1 \rightarrow p'=n-1$) occurs with probability

$$P_n^{\text{diab}}(V) = \exp(-\beta_n \pi V^2), \quad (4.1)$$

where the new n -dependent factor in the exponent is [45]

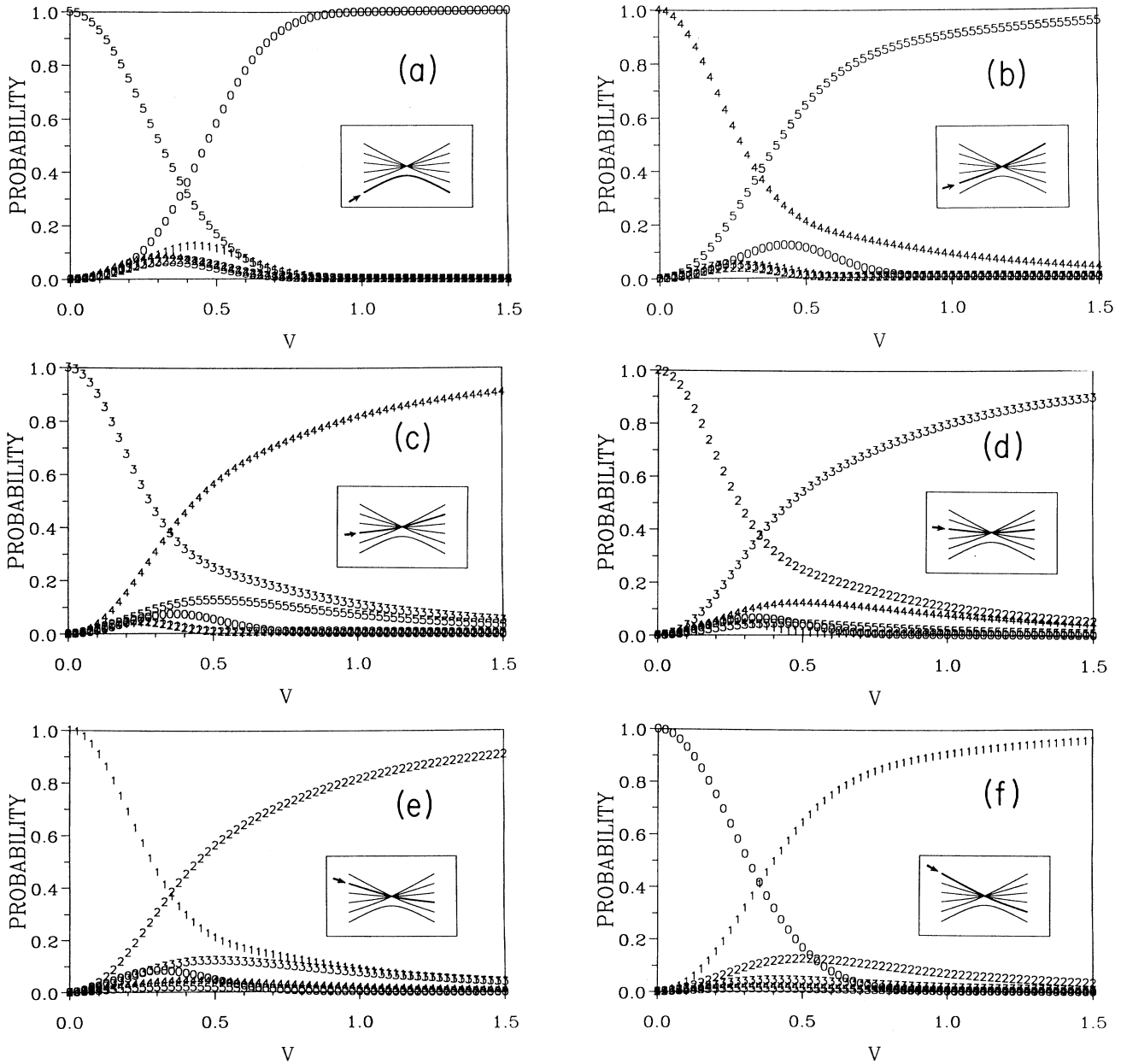


FIG. 7. Probabilities $P_{q \rightarrow q'}(V)$ of arriving in state q' of the $n=6$, $m=0$ manifold beginning in state (a) $q=0$, (b) $q=5$, (c) $q=4$, (d) $q=3$, (e) $q=2$, (f) $q=1$. Curves marked with q' . Insets, as in Fig. 6. See text.

$$\beta_n \equiv \frac{1}{1} + \frac{1}{2} + \cdots + \frac{1}{n-1} \quad (4.2)$$

$$\approx \ln n + 0.5772 - \frac{1}{2n}.$$

This analytic expression is suggested by the $V \rightarrow 0$ form of $P_{p \rightarrow p}(V)$ for $p = n-1$, Eq. (3.30), where β_n is just the coefficient of πV^2 . In Fig. 9(b) we present a comparison between (1) the numerical calculations of $P_{0 \rightarrow n-1}$ used to generate Fig. 9(a) and (2) the exact formula for P_n^{diab} , again for $n=2, 3, 6, \dots, 96$. The symbols mark numerical results; the solid lines are independent plots of Eq. (4.1) using the definition (4.2). The agreement is exact to within the error [$\approx O(0.01\%)$] of the calculations shown in Fig. 9, and has been verified in other runs at higher accuracy—to better than 1 part in 10^6 . We claim that the above conjecture holds exactly.

Outer diabatic transitions connect the extreme bottom of a manifold to the extreme top, or vice versa [42]: $p = \pm(n-1) \rightarrow p' = \pm(n-1)$. Equation (4.1) thus resembles the familiar two-level result (2.41), to which it reduces upon setting $\beta_2=1$. [Note that the rough estimate (2.40) for $n > 2$, which was based on the two-level LZE, amounts to the guess $n/4$ instead of $\beta_n \approx \ln n$.] We

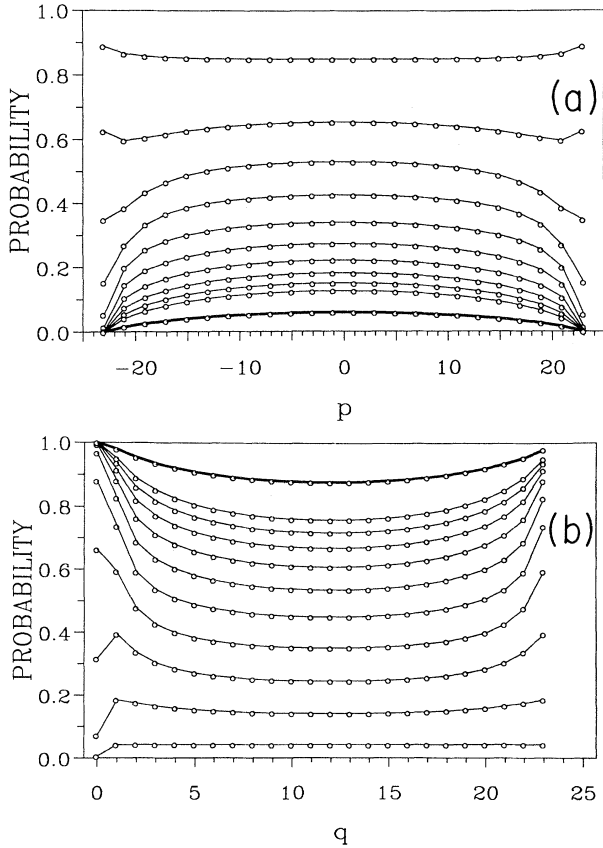


FIG. 8. (a) Diabatic-transition probabilities $P_{p \rightarrow p}$ vs p (\circ) for fixed values (from top to bottom) $V=0.1, 0.2, 0.3, \dots, 1.0$ (thin lines), and $V=1.5$ (thick line). (b) Adiabatic-transition probabilities $P_{q \rightarrow q}$ vs q (\circ), same values of V (from bottom to top).

therefore regard the statement $P_n^{\text{diab}} = e^{-\beta_n \pi V^2}$ as the multilevel generalization of $P^{\text{diab}} = e^{-\pi V^2}$ to all $n \geq 2$, and as a generalization of the LZE to the MLZE (though in a restricted sense, insofar as it refers to a specific transition and coupling scheme).

Equations (4.1) and (4.2) suggest a sequence of two-level diabatic Landau-Zener transitions that occur with probabilities $P_k = \exp(-\pi V^2/k)$ ($k=1, \dots, n-1$). The results of Ref. [16] further suggest that the $\{P_k\}$ could then be used to generate a full set of probabilities $\{P_{p \rightarrow p'}(V)\}$ for all p and p' analytically. However, no set of probabilities so generated agrees with our numerical results for the bowtie [except for $p=p'=\pm(n-1)$]; see Sec. VI.

The explicit dependence of P_n^{diab} on real ramp rates follows from Eq. (4.1) and the definition (2.27) of V :

$$P_n^{\text{diab}}(\dot{F}) = \exp \left[-\frac{2\pi\beta_n |\mu_0|^2}{3\dot{F}n^9} \right], \quad (4.3)$$

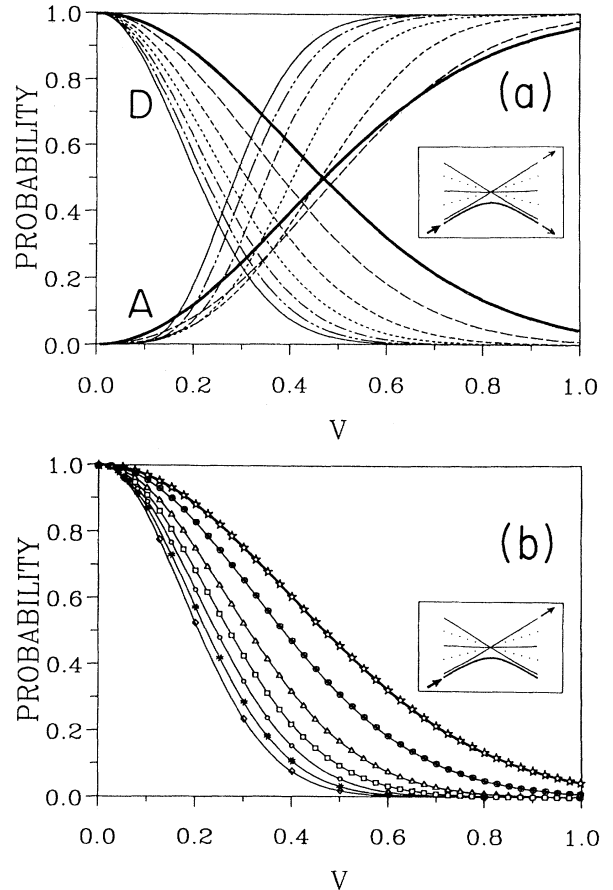


FIG. 9. (a) Probabilities $P_{0 \rightarrow q'}(V)$ for adiabatic ($q=0 \rightarrow q'=0$) and diabatic ($q=0 \rightarrow q'=n-1$) transitions from the shifted level $q=0$, sets of curves *A* and *D*. Manifolds $m=0$ and $n=2$ (—), $n=3$ (---), $n=6$ (---), $n=12$ (---), $n=24$ (---), $n=48$ (---), $n=96$ (—). (b) $P_n^{\text{diab}}(V)$ for outer diabatic transitions: smooth curves, analytical, Eqs. (4.1) and (4.2); symbols, numerical, for $n=2$ (stars), $n=3$ (\oplus), $n=6$ (\triangle), $n=12$ (\square), $n=24$ (\circ), $n=48$ ($*$), $n=96$ (\diamond). Note that V depends on n , Eq. (2.27).

where \dot{F} is in atomic units. In conventional units Eq. (4.3) reads

$$P_n^{\text{diab}} \left[\frac{\dot{F}}{\mu_0^2} \right] = \exp \left[-\beta_n \left[\frac{196.9}{n} \right]^9 \frac{\mu_0^2}{\dot{F}} \right]. \quad (4.4)$$

with \dot{F} in V/cm μsec . For large n , Eq. (4.2) allows us to recast Eq. (4.4) in the form [45]

$$P_n^{\text{diab}} \left[\frac{\dot{F}}{\mu_0^2} \right] = (1.781n)^{[-(196.9/n)^9 \mu_0^2 / \dot{F}]}, \quad (4.5)$$

which reveals the scaling $P_n^{\text{diab}} \propto (n_0/n)^{(n_0/n)^9}$ (where n_0 depends on \dot{F}). Note the similarity of the exponent in (4.3) to the LZSE exponent (2.39). The curves for higher n , as a function of \dot{F} , rise from zero to unity at lower \dot{F} because higher Rydberg manifolds undergo weaker core effects (shifts of approximately $\mu_0 n^{-4}$) and stronger Stark splitting (slopes of approximately n). Therefore, one requires a significantly slower laboratory slew rate, $\dot{F} \propto (\ln n)/n^9$, to observe an outer diabatic transition at higher n with the same probability as at lower n .

Figure 10 shows P_n^{diab} , for n up to 100, plotted against \dot{F}/μ_0^2 on a logarithmic scale, with \dot{F} expressed in V/cm μsec . Such a plot is useful for gauging the states in which the full MLZE—i.e., all diabatic and adiabatic transitions through an $m=0$ bowtie—could be studied experimentally with available slew rates. For example, if the maximum quantum defect were 0.1 and \dot{F} were in the range 1000–10 000 V/cm μsec , one could observe the MLZE for $40 < n < 70$. Lower n manifolds would have $P_n^{\text{diab}} \approx 0$, so all transitions through them would be essentially adiabatic.

The above discussion of the outer diabatic transition probability suggests that all functions $P_{q \rightarrow q'}(V)$ for a given n manifold incorporate the factor β_n into a rescaling of V , at least for $l=0$. If we replace the exponent in Eq. (4.1) with $-\beta_n \pi V^2 \equiv -\pi \tilde{V}^2$, then

$$\begin{aligned} \tilde{V} &\equiv \sqrt{\beta_n} V = |\mu_0| n^{-4} \sqrt{\beta_n} (\frac{3}{2} \dot{F} n)^{-1/2} \\ &\approx 0.816 \sqrt{\ln n} n^{-9/2} |\mu_0| \dot{F}^{-1/2} \end{aligned} \quad (4.6)$$

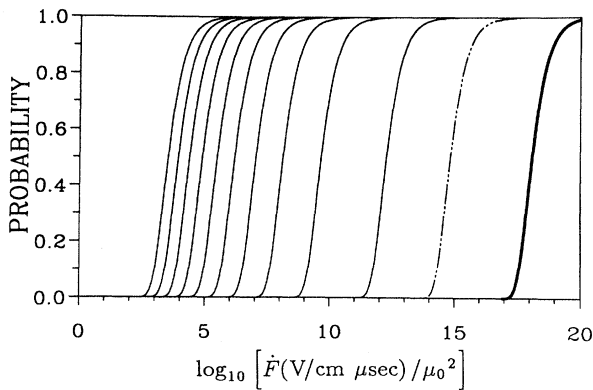


FIG. 10. P_n^{diab} vs $\log_{10}(\dot{F}/\mu_0^2)$ [Eq. (4.4)], where ramp rate \dot{F} is in V/cm μsec . Manifolds $m=0$ and $n=2$ (—), $n=5$ (---), and $n=10, 20, 30, \dots, 100$ (—).

supercedes the definition (2.27) (for $l=0$). Figure 11 shows representative transitions from (a) $q=0$, (b) $q=n-1$, (c) $q=\frac{1}{2}n$, and (d) $q=1$ for the same range of n used in Fig. 9. Each plot shows the trends for adiabatic, diabatic-neighbor, and other-neighbor transition probabilities as n is doubled up to $n=96$.

Transitions from the shifted level [$q=0$, Fig. 11(a)] appear to converge well as n increases. The outer-diabatic curves coincide by construction. The introduction of other-neighbor curves starting with $n=3$ changes the adiabatic behavior significantly; but by $n=24, 48$, and 96 all curves seem to approach limiting functional forms, albeit slowly, first at high \tilde{V} and then at low \tilde{V} . Similarly, transitions from the adiabatic edge levels [$q=n-1$ and 1, Figs. 11(b) and 11(d)] stably evolve to high- n forms, apparently at low \tilde{V} before high \tilde{V} in this case. Note also how the edge-to-edge-neighbor transitions peak at intermediate values of \tilde{V} .

While transitions near the manifold edges behave regularly at high n , the midmanifold behavior [Fig. 11(c)] does not settle down so quickly. As discussed in Sec. IV B, adiabatic and other-neighbor transitions near the center are suppressed compared to the edges at slow ramps; this is seen to occur for all n in Fig. 11(c). However, the rescaling (4.6) is evidently *not* appropriate to the quasicontinuum of levels near the manifold's center, whose gross dependences on n and \dot{F} differ from that of the levels near the edges by not converging at high \tilde{V} as n increases.

Yet it is not immediately clear how to formulate the $n \rightarrow \infty$ limit as a continuum problem. If we regard the diabatic levels as forming a continuum in the λ scale (Fig. 4), then we must regard the shifted level as an interloper that is tuned through the continuum in time. However, the preference for midmanifold transitions $q \rightarrow q$ and $q \rightarrow q \pm 1$ introduces a graininess into such a “continuum.” The limiting forms of $P_{q \rightarrow q'}(V)$ await further study.

We note, finally, that P_n^{diab} for the case of a single $\mu_l \neq 0$, $l=m$, adheres to the analytical forms (4.1) and (4.3) for any $m > 0$ as well as $m=0$, according to calculations performed for $m \neq 0$. One must then use $V = V_l = V_m$, replace $|\mu_0|^2$ with $|\mu_m|^2$, and replace β_n in Eq. (4.2) with

$$\beta_{nm} = 2u_{pl}^2 \sum_{s (\neq p)} \frac{u_{sl}^2}{|p-s|}, \quad p = n - m - 1, \quad l = m \quad (4.7)$$

[cf. Eqs. (2.27) and (3.32)]. The validity of our conjecture for the MLZE in fact seems to transcend the single-quantum-defect approximation, according to preliminary studies. For an arbitrary set of values $\{\mu_l\}$, the probability for outer diabatic transitions is *always* an exponential function having the large- \dot{F} expansion (3.32).

V. TWO QUANTUM DEFECTS

In the model based on a single quantum defect μ_l , all transitions proceed diabatically in the limit $V_l \rightarrow 0$. This corresponds to $\mu_l \rightarrow 0$ for a given ramp rate. In actuality all μ_l are nonzero but quite small, except for the first few

$(\mu_m, \mu_{m+1}, \dots)$. Whereas \dot{F} might be such that V_m, V_{m+1}, \dots , have intermediate values of order one, so that some transitions are adiabatic and some diabatic, all higher l would in contrast have vanishingly small values of V_l . Therefore, the high- l anticrossings at $F \approx 0$ are effectively of zero size: i.e., no coupling of levels through high- l channels occurs within the tiny regions $|F| \lesssim 2|\mu_l|/3n^5$ (unless \dot{F} is extremely small). We can then set $\mu_l = 0$ for all but the few lowest $l \geq m$, the number depending on \dot{F} .

To illustrate the effect of introducing a second nonzero μ_l , we have plotted in Fig. 12 some transition probabilities for $n = 12$, $m = 0$, $\mu_0 = 0.30$, and $\mu_1 = \frac{1}{5}\mu_0$. There are now shifted levels for both $l = 0$ and 1, so $q = 0$ and 1 represent the two lowest levels of the manifold's bowtie at all F (see inset to Fig. 12). We have chosen the initial state $q = 1$, since a fast ramp will "shoot through" the small anticrossing at $F \approx 0$, but a slow enough ramp will allow the $q = 1$ population to move adiabatically through the small- F region and remain in $q = 1$.

Consider first the fast-ramp limit. The probabilities

$P_{1 \rightarrow q'}$ vs V_0 should resemble the curves of Figs. 7(b) and 11(b) if we can neglect μ_1 . Adiabatic, diabatic, and other-neighbor transitions then correspond to $q = 1 \rightarrow q' = 11$, $q' = 10$, and $q' = 0$, respectively [cf. inset to Fig. 11(b)], where we have followed the conventions of Sec. II A for labeling adiabatic levels when there are two quantum defects. Final populations for these states, shown in Fig. 12, indeed follow the expected patterns in the high- \dot{F} range $0 \leq V_0 \lesssim 0.5$.

A scale appropriate to $\mu_1 \neq 0$ is V_1 instead of $V_0 = 5V_1$; equivalently, the scale V_0 can be extended five times as far as is usually necessary to see the adiabatic transition dominate (this was done in Fig. 12). Very slow ramps in the V_0 scale ($V_0 \gg 1$) would not significantly change the $q = 0$ population, so we now imagine the bowtie without the $q = 0$ level but with a truly shifted $q = 1$ level. This case, too, should behave like a manifold with only one nonzero μ_l , resembling Figs. 7(a) and 11(a) for transitions from the shifted level. Now adiabatic, diabatic, and other-neighbor transitions correspond to $q = 1 \rightarrow q' = 1$, $q' = 11$, and $q' = 2$, respectively. In the region $V_0 > 1.5$ of

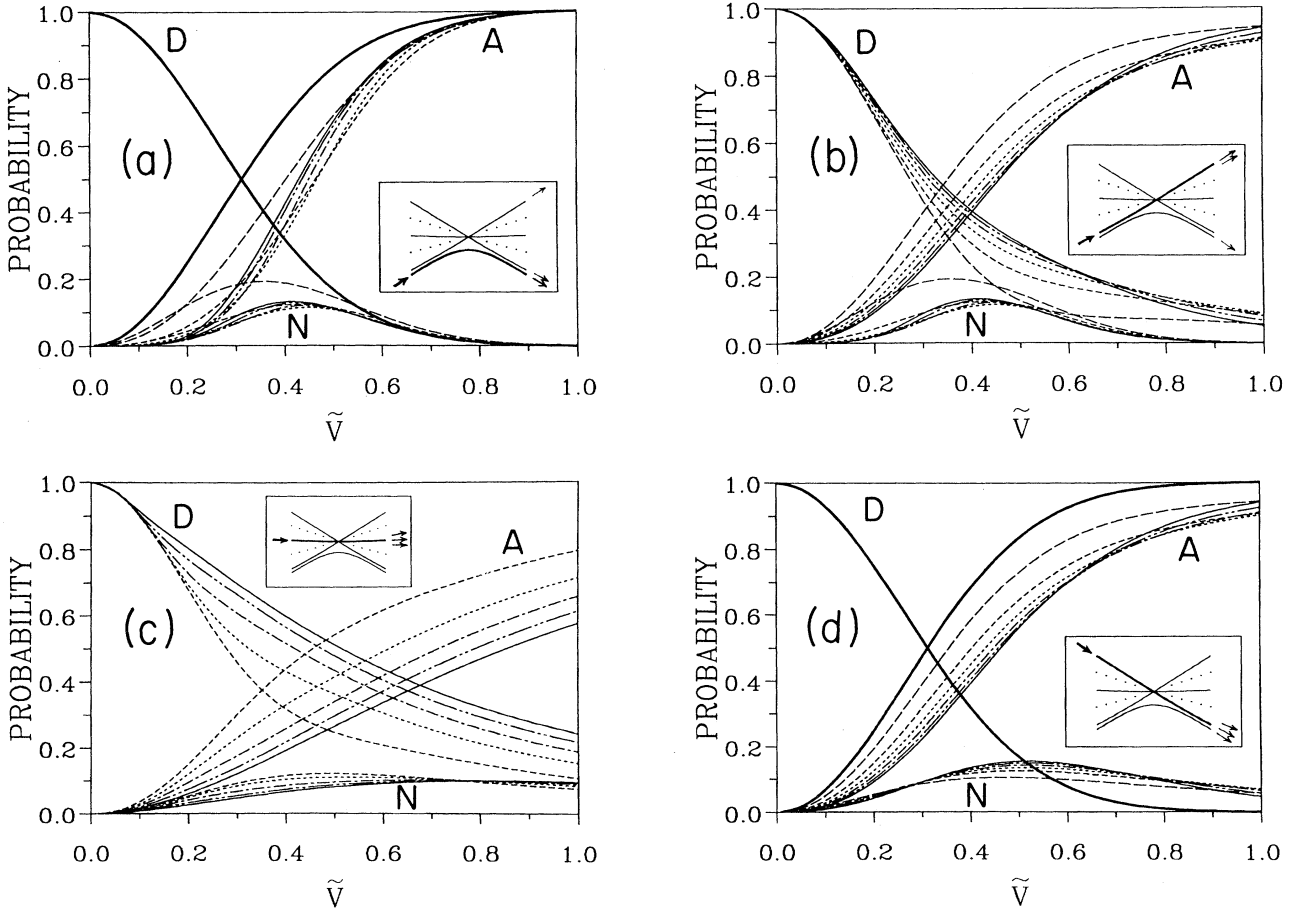


FIG. 11. Transition probability $P_{q \rightarrow q'}$ vs rescaled \tilde{V} , Eq. (4.6), for $m = 0$ and same n as Fig. 9(a) (where the lines are defined): initial state (a) $q = 0$, (b) $q = n - 1$ ($n > 2$), (c) $q = \frac{1}{2}n$ ($n > 3$), (d) $q = 1$. The set of curves A show final q' for adiabatic transitions for each n ; curves D , diabatic transitions; curves N , other-neighbor transitions (see Ref. 36). V scale chosen so that $\tilde{V} = V$ for $n = 6$. Insets: generic bowties showing relevant q 's; thick line, initial q .

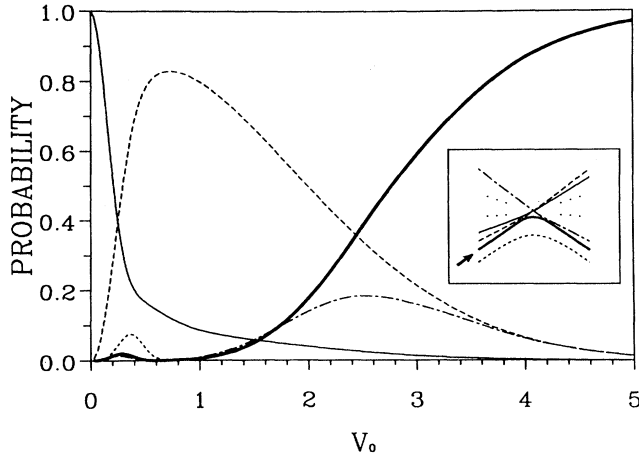


FIG. 12. Transition probability $P_{q \rightarrow q'}$ vs V_0 for $n=12$, $m=0$, two quantum defects $\mu_0=0.30$ and $\mu_1=0.06$, and initial $q=1$. Curves shown for final $q'=0$ (---), 1 (—), 2 (— · —), 10 (— · — · —), and 11 (— · — · —), whose levels appear in inset's bowtie. Note similarity of region $V_0 < 0.5$ to Fig. 7(b), and $V_0 > 1.5$ to Fig. 7(a); see text.

Fig. 12, these curves $P_{1 \rightarrow q'}$ once more agree with the previous single- μ_l results, at least qualitatively.

Different ranges of $|\mu_l|$ thus map onto different ranges of V or \dot{F} . Within each such range, higher (lower) values of $|\mu_l|$ are represented by “sub-bowties” whose probabilities $P_{q \rightarrow q'}$ have effectively attained their limiting fast-ramp (slow-ramp) behavior. All probabilities must of course vary continuously over all ranges of \dot{F} or any V_l , as do those shown in Fig. 12; e.g., note $q'=11$, which switches roles from adiabatic- to diabatic-transition curve. Interference effects will lead to yet more complicated functions $P_{q \rightarrow q'}(V_l)$ when some quantum defects are of the same magnitude and especially when they are of opposite sign. A study of manifolds with several quantum defects will be presented elsewhere.

VI. CONCLUDING REMARKS

We have considered a model of level mixing within a single Rydberg manifold subject to a linearly ramped electric field. The energy levels, composition of the eigenstates, and field-induced coupling among the eigenstates can be described analytically in the simplest case of a purely $l=0$ electron-core interaction ($\mu_0 \neq 0$). Studies of the time evolution operator for this model reveal general patterns in the state-to-state transition probabilities. Most notably, a ramp across the manifold at any rate \dot{F} induces principally adiabatic ($q \rightarrow q$) or diabatic ($p \rightarrow p$) transitions from an initial level; i.e., the final population is always dominated by only two or three particular states, whether the traversal was slow or fast. The introduction of additional quantum defects produces iterations of single- μ -like patterns over slower scales of \dot{F} , allowing one to ignore all but the first few μ_l in practice. Outer diabatic transitions mimic the two-level LZSE, $P^{\text{diab}} = e^{-2\pi\gamma}$, where $\gamma = \beta_n |\mu_0|^2 / (3\dot{F}n^9)$ for the $l=m=0$ case; a simi-

lar result is expected to hold for any set of quantum defects. This MLZE should be observable in transitions within moderately high- n Rydberg manifolds at accessible slew rates [6,20].

Several unresolved issues raised by this model persist, as does the need to extend it. (1) The joint effect of several comparable quantum defects on the probabilities $P_{q \rightarrow q'}(V_l)$ needs to be investigated to identify the kinds of patterns hinted at in Fig. 12, especially oscillations stemming from interference between l channels. (2) A better understanding of the $n \rightarrow \infty$ limit should shed light on the grainy nature of transitions among levels near the middle of the manifold. At first glance the high density of states suggests a continuum bounded from both below and above—but edge and midmanifold states seem to function differently in this regard. (3) Nonlinear field behavior [6,20,21] can be expected to produce non-LZE-like patterns $P_{q \rightarrow q'}$ (defined over suitable time intervals), since the factor dF/dt then leads to variable eigenchannel mixing in Eq. (2.22). Alternatively, as the Fourier transform of the field becomes more nearly monochromatic, a description of state mixing based on the absorption and emission of photons becomes more appropriate. (The purely linear field inconveniently requires photons of all energies.) (4) The next stage of applications to experiments on ramped fields [6] and selective-field ionization [3,4] should involve coherent level mixing between two or more manifolds, at $F \gtrsim 1/3n^5$ [Eq. (1.4)].

An outstanding theoretical challenge is the construction of a rigorous proof of the conjecture of Sec. IV C concerning outer diabatic transitions—that an analytical form of $P_n^{\text{diab}}(V)$ can be found. The elegant method of Demkov [16] suggests that a contour-integral representation of the amplitudes $U_{p,p}(\infty, -\infty)$ be considered. However, the Hamiltonians treated in Ref. [16] involve only *one* diabatic level which varies linearly with time. In the bowtie problem, *all* diabatic levels are proportional to t with different slopes; this case cannot simply be mapped onto the other. An attempt to generalize Demkov's approach is currently under way.

ACKNOWLEDGMENTS

The author would like to thank Phillip Price, Keith MacAdam, Michael Cavagnero, and several other colleagues for their pertinent remarks throughout the course of this work.

APPENDIX A: TRANSFORMATION BETWEEN p AND l BASES

The orthonormal transformation $U_{pl}^{(nm)}$ between parabolic and spherical bases, introduced in Eq. (2.13), is most simply expressed as a Wigner coefficient [46] representing the coupling of two mock angular momenta j_1 and j_2 :

$$U_{pl}^{(nm)} = \langle lm | j_{1z} j_{2z} \rangle, \quad (\text{A1})$$

where

$$\begin{aligned} j_1 = j_2 = \frac{1}{2}(n-1), \\ j_{1z} = \frac{1}{2}(m+p), \quad j_{2z} = \frac{1}{2}(m-p), \end{aligned} \quad (\text{A2})$$

TABLE III. Squared transformation coefficients u_{pl}^2 for $0 \leq m \leq l \leq 3$. Prefactor in parentheses is the sign of u_{pl} when the positive root of u_{pl}^2 is taken; $p = n_1 - n_2$. Note the orthonormality condition (2.14').

l	m	$(\pm)u_{pl}^2$
0	0	(+)1
1	0	(-)3p ² /(n ² -1)
1	1	(-) ³ / ₂ (n ² -p ²)/(n ² -1)
2	0	(+) ⁵ / ₄ (3p ² -n ² +1) ² /[(n ² -1)(n ² -4)]
2	1	(+) ¹⁵ / ₂ (n ² -p ²)p ² /[(n ² -1)(n ² -4)]
2	2	(+) ¹⁵ / ₈ [(n+1) ² -p ²][(n-1) ² -p ²]/[(n ² -1)(n ² -4)]
3	0	(-) ⁷ / ₄ (5p ² -3n ² +7) ² p ² /[(n ² -1)(n ² -4)(n ² -9)]
3	1	(-) ²¹ / ₁₆ (n ² -p ²)(5p ² -n ² +4) ² /[(n ² -1)(n ² -4)(n ² -9)]
3	2	(-) ¹⁰⁵ / ₈ [(n+1) ² -p ²][(n-1) ² -p ²]p ² /[(n ² -1)(n ² -4)(n ² -9)]
3	3	(-) ³¹ / ₁₆ [(n+2) ² -p ²](n ² -p ²)[(n-2) ² -p ²]/[(n ² -1)(n ² -4)(n ² -9)]

and $p = n_1 - n_2$. Explicit forms of $U_{pl}^{(nm)}$ as a function of p and E can be derived for fixed l and m [47]. Expressions for the renormalized u_{pl} of Eq. (2.14) are presented in Table III for $l \leq 3$. Note that, in the limit $n \rightarrow \infty$, $(-1)^{l-m}u_{pl}/\sqrt{2}$ reduces to a normalized associated Legendre polynomial [26], $\bar{P}_l^m(p/n)$.

APPENDIX B: SOME ANALYTICAL DETAILS

Sign conventions

Whenever a matrix is diagonalized [as in Eqs. (2.18) and (3.8)], each normalized eigenvector carries an arbitrary phase factor. It is necessary to standardize and keep track of such factors lest inconsistencies from one time step to the next allow extra minus signs to appear in the Riemann product (3.6) in a discontinuous way. Temporal continuity of the state vector (2.2) in any basis amounts to ordering the energy eigenvalues and following them adiabatically; an unambiguous ordering at any time t is achieved here in the q basis (Sec. II A).

In the single quantum-defect case of Sec. II C, the relative signs of all the elements c_{pq}^φ [Eq. (2.58)] with $q > 0$ are determined by the behavior of $\lambda_q^\varphi - (n_1 + \frac{1}{2})_p$ (see Fig. 4): this factor does not change sign with t , so neither does the normalization factor N_q^φ [Eq. (2.59)]. However, for $q = 0$, λ_q^φ and hence the denominator of (2.58) do switch sign when t does; N_q^φ must then change sign at $t = 0$ to keep c_{p0}^φ continuous. We are free to choose $c_{pq}^\varphi/u_{pl} > 0$ for the first row of \mathbf{c}^φ (i.e., for $n_1 = 0$) at $t < 0$. The sign structure of \mathbf{c}^φ for the $n = 10$ example, aside from the factor u_{pl} , then has the form

$$n_1=0 \begin{pmatrix} q=0 & 1 & 2 & 3 & \cdots & 9 \\ + & + & + & + & \cdots & + \\ 1 & + & - & + & \cdots & + \\ 2 & + & - & - & \cdots & + \\ 3 & + & - & - & \ddots & + \\ \vdots & \vdots & \vdots & \vdots & \ddots & \vdots \\ 8 & + & - & - & \ddots & + \\ 9 & + & - & - & \cdots & - \end{pmatrix} \quad (\text{B1})$$

at all φ (or τ or F). Following Eqs. (2.59)–(2.61), this further implies that the signs of $\Gamma_{qq'}^\tau$ are given for $n = 10$ by

$$\text{sgn} \Gamma^\tau = \begin{matrix} & q'=0 & 1 & 2 & 3 & \cdots & 8 & 9 \\ q=0 & \left(\begin{array}{cccccccc} 0 & + & + & + & \cdots & + & + \\ 1 & - & 0 & - & \cdots & - & - \\ 2 & - & + & 0 & - & \cdots & - & - \\ 3 & - & + & + & 0 & \ddots & - & - \\ \vdots & \vdots & \vdots & \vdots & \ddots & \ddots & \ddots & \vdots \\ 8 & - & + & + & + & \ddots & 0 & - \\ 9 & - & + & + & + & \cdots & + & 0 \end{array} \right) & \end{matrix} \quad (\text{B2})$$

at all τ , which is consistent with Fig. 5. When several quantum defects are involved, prediction of the eigenvalues λ_q^φ and the signs of $\Gamma_{qq'}^\tau$ is not nearly so straightforward.

Constraint on $\mathcal{H}(t)$

The generators for a linear field are highly symmetric under the time parity operation (3.17). In the three bases considered here, the Hamiltonians behave as follows.

The spherical-basis state labels do not permute when $t \leftrightarrow -t$ because the eigenenergies E_l , Eq. (2.5), do not vary with field. Under $F \leftrightarrow -F$ the tridiagonal system (2.7) and (2.8) simply becomes

$$H_{pp'}^{\text{sph}}(-t) = (-1)^{l+l'} H_{pp'}^{\text{sph}}(t). \quad (\text{B3a})$$

Under $F \leftrightarrow -F$ the parabolic-basis energies $E_p(F)$ [Eq. (2.10)], undergo $p \leftrightarrow -p$, a reversal of their order. Some of the transformation coefficients u_{pl} (those with odd $l-m$, Table III) then suffer sign changes $(\pm 1)_p$ in the nonhydrogenic terms of Eqs. (2.15) and (3.11), so

$$H_{pp'}^{\text{diab}}(-t) = (\pm 1)_p (\pm 1)_{p'} H_{-p, -p'}^{\text{diab}}(t). \quad (\text{B3b})$$

The construction of \mathbf{H}^{adi} , Eq. (2.22), depends on the diagonalization of \mathbf{H}^{diab} , whereby each eigenvector labeled q can pick up a phase $(\pm 1)_q$, as discussed above. A set of eigenenergies $\{E_q^F\}$ at $F(t)$ has precisely the same values at $F(-t)$ except the adiabatic state labels $\{q\}$ are permuted (see Secs. II A and III B). Otherwise, $t \leftrightarrow -t$ is equivalent to $\hat{F} \leftrightarrow -\hat{F}$, which implies

$\mathbf{H}^{\text{adi}}(-t) \leftrightarrow [\mathbf{H}^{\text{adi}}(t)]^*$, or

$$H_{qq'}^{\text{adi}}(-t) = (\pm 1)_q (\pm 1)_{q'} \langle\langle H_{qq'}^{\text{adi}}(t) \rangle\rangle^* . \quad (\text{B3c})$$

Evaluation of integrals

The high- \dot{F} expansion of $\mathbf{U}(\infty, -\infty)$ given in Eq. (3.25) applies to an arbitrary set of quantum defects. However, its usefulness is limited because only the first- and second-order terms are readily evaluated. For p basis indices j and k (slopes $p_j = p'$, $p_k = p$), the results to within an overall phase are

$$U_{jk}(\infty, -\infty) = \delta_{jk} + iV_{jk} \mathfrak{J}_{jk} I_{jk}^{(1)} - \sum_s V_{js} V_{sk} \mathfrak{J}_{js} \mathfrak{J}_{sk} I_{jsk}^{(2)} + \dots , \quad (\text{B4})$$

$$I_{jk}^{(1)} = \Phi_{jk} \left[\frac{2\pi i}{p_j - p_k} \right]^{1/2} , \quad (\text{B5a})$$

$$I_{jsk}^{(2)} = \Phi_{js} \Phi_{sk} \frac{1}{2!} \frac{2\pi i}{\sqrt{(p_j - p_s)(p_s - p_k)}} \text{erfc}(z_0) , \quad (\text{B5b})$$

where

$$\Phi_{jk} = \exp \left[-i \frac{(v_{jj} - v_{kk})^2}{2(p_j - p_k)} \right] \quad (\text{B6})$$

is a phase factor; V_{jk} is defined in Eq. (3.22); $\mathfrak{J}_{jk} \equiv 1 - \delta_{jk}$; the argument of the complementary error function [48] is

$$z_0 = \frac{(p_j - p_s)(v_{ss} - v_{kk}) - (p_s - p_k)(v_{jj} - v_{ss})}{\sqrt{2i(p_j - p_s)(p_s - p_k)(p_j - p_k)}} ; \quad (\text{B7})$$

and phases are chosen so that, e.g., $\sqrt{p_j - p_k} = +i\sqrt{|p_j - p_k|}$ when $p_j - p_k < 0$. These expressions also apply when $j = k$ ($p' = p$), in which case $\Phi_{js} \Phi_{sk} = 1$; $z_0 = 0$ and $\text{erfc}(0) = 1$; and the radical in (B5b) equals $i|p_j - p_s|$.

In the single- μ_l , $l = 0$ case all elements of the coupling matrix (3.22) equal $V = V_0$. All phase factors Φ equal unity and the above expressions reduce to Eq. (3.26) or (3.27). In forming $|U_{p'p}(\infty, -\infty)|^2$ from (3.26) to obtain Eqs. (3.28) and (3.29), one extracts the real parts of sums such as $(p' - p)^{-1/2}$ times $i^{5/2}\Sigma_1$, $i^{3/2}\Sigma_2$, and $i^{5/2}\Sigma_3$ for $p' < p$, and times $i^{1/2}\Sigma_1$, $i^{3/2}\Sigma_2$, and $i^{1/2}\Sigma_3$ for $p' > p$. The general first-order result (3.32) follows from Eqs. (B4) and (B5a), which yield $|U_{jk}(\infty, -\infty)|^2 = 2\pi(V_{jk})^2/|p_j - p_k|$ for $j \neq k$.

APPENDIX C: NUMERICAL DETAILS AND CONVERGENCE

The procedure for calculating $\mathbf{U}(\tau, \tau_0)$ is outlined in the beginning of Sec. III; its actual implementation in TIMEPASS is described in this appendix. The rescaled time τ and Hamiltonians $H_{pp'}^{\text{diab}}(\tau)$ and $H_{qq'}^{\text{adi}}(\tau)$ are used here. In the absence of the use of \dot{F} , slow (or fast) ramp rates are synonymous with high (or low) V , respectively, where V equals V_l for that l having the largest $|\mu_l|$.

Time domain

The entire range $[\tau_0, |\tau_0|]$ is specified by choosing some $\tau_0/V \ll 0$. The adiabatic states are coupled predominantly at $|\tau| < 3V$, whereas the convergence of $\mathbf{U}(|\tau_0|, \tau_0)$ to $\mathbf{U}(\infty, -\infty)$ occurs in the domain $|\tau| > 5V$. In the ‘‘tails’’ of the time evolution, as $|\tau| \rightarrow \infty$, the interchannel phase approaches

$$\int^\tau d\tau' [E_p(\tau') - E_{p'}(\tau')] \sim \frac{1}{2}(p - p')\tau^2 .$$

Since typical coherence lengths in τ correspond to phase accumulations of π —the longest occurring between adjacent levels ($|p - p'| = 2$)—macroscopic time intervals at large $|\tau|$ should scale like $\Delta\tau \lesssim \pi/2|\tau|$ (for any V). However, the adiabatic coupling $\Gamma_{qq'}^\tau$ diminishes like τ^{-2} [cf. Eqs. (2.67) and (3.35)]. Thus, $\mathbf{U}(\tau_0, -|\tau|)$ or $\mathbf{U}(\tau, |\tau_0|)$ converges at $|\tau| \gg |\tau_0|$ reasonably well but requires smaller and smaller time steps and greater computational effort. Since the tails tend to contribute much less than 1% to the final $U_{q'q}(\infty, -\infty)$, it suffices simply to use a large, fixed value for τ_0 ; the usual choice was $\tau_0 = -10$ to -12 for $n \geq 24$ or moderate accuracy (1 part in 10^4), and $\tau_0 \leq -20$ for low n or much higher accuracy. If especially high accuracy is desired (e.g., 1 part in 10^8), one could choose an even bigger $|\tau_0|$, dynamically explore $|\tau| > |\tau_0|$ until $U_{q'q}(\tau + \Delta\tau, \tau)$ sufficiently approaches the unit matrix, or derive an analytical series in powers of $1/\tau$ for $\mathbf{U}(\infty, \tau) = \langle\langle \mathbf{U}(-\tau, -\infty) \rangle\rangle^T$ at $\tau \geq |\tau_0|$.

Subdividing the time scale

The domain $[\tau_0, |\tau_0|]$ is divided into equal macroscopic time steps $\Delta\tau_j = \tau_j - \tau_{j-1}$ ($j = 1, \dots, N$). The size of the macroscopic intervals is typically fixed at $\Delta\tau = \frac{1}{2}$ or 1. Although one has the flexibility to shrink $\Delta\tau_j$ at larger $|\tau_j|$, or to choose otherwise arbitrary $\{\tau_j\}$, it was found that this did not greatly enhance the efficiency of the total calculation for linear ramps.

Direct calculation of $\mathbf{U}(\tau_j, \tau_{j-1})$ via Eqs. (3.16) and (D5) does not usually give a sufficiently accurate result for the j th interval, however. Further subdivision of $[\tau_{j-1}, \tau_j]$ into N'_j smaller intervals of equal width $\Delta\tau'_j = \Delta\tau/N'_j$ improves the accuracy of \mathbf{U} over each such microscopic domain, and hence the accuracy of the Riemann product

$$\mathbf{U}(\tau_j, \tau_{j-1}) = \prod_{k=1}^{N'_j} \mathbf{U}(\tau_{j-1} + k\Delta\tau'_j, \tau_{j-1} + (k-1)\Delta\tau'_j) \quad (\text{C1})$$

over the whole macroscopic interval. In each macroscopic interval, the number of microscopic subdivisions is increased until a desired accuracy is reached. TIMEPASS tries the sequence [49] $N' = \{1, 2, 3, 4, 6, 8, 12, 16, 24, 32, 48, 64, 100, 150, 200, 300, 500\}$, the rationale being optimization: only a few microscopic intervals might suffice, so trial values of N'_j should not increase too fast, yet occasionally very small subdivisions are needed, e.g., if the current basis is inappropriate to a particular time domain. (Note that the choice $\Delta\tau \sim 1$ is large enough to

permit a nontrivial number of successively finer subdivisions to test convergence yet small enough so that the Magnus corrections can begin to converge [50].) Our somewhat simplistic test for convergence forms the product of $\mathbf{U}(\tau_j, \tau_{j-1})$ resulting from the previous trial N'_j and \mathbf{U}^\dagger for the present value of N'_j , and compares this product with the unit matrix: “convergence” is achieved when the magnitude of the largest off-diagonal element falls below a prespecified accuracy.

It is desirable to minimize the total number of diagonalizations performed by minimizing the total number of trial microscopic steps. Computation is reduced by beginning the microscopic-number sequence for the $(j+1)$ th macroscopic interval with the N' that is two choices smaller than the final value of N'_j used for the j th interval, rather than with $N'_{j+1}=1$. This allows for a final $N'_{j+1} < N'_j$ while avoiding what are probably wasted trials with too few subdivisions. For calculations of the full time evolution matrix $\mathbf{U}(|\tau_0|, \tau_0)$, a global savings of 50% comes from the use of Eq. (3.19), which effectively halves the total time domain owing to the symmetries of $\mathcal{H}(\tau)$ discussed in Sec. III B. [The phases that appear upon $\tau \leftrightarrow -\tau$ are easily obtained via Eq. (B3a) after temporarily switching to the spherical basis.]

Choice of basis

The three bases introduced in Sec. II A approximately diagonalize $\mathcal{H}(\tau)$ under different conditions: the spherical basis when $|\tau| \ll V$, the parabolic one when $|\tau| \gg V$ or $V \ll 1$ (fast ramp), and the local basis when $V \gg 1$ (slow ramp). Any basis employed under conditions unfavorable for the j th macroscopic step might require a very large number N'_j of microscopic subdivisions, enjoy less efficient matrix diagonalizations (and a higher cost in real computation time), or converge only slowly.

The usefulness of the l basis was found to be limited in practice, at least for full traversal of the manifold: although it requires about as many total diagonalizations as the parabolic basis and has the advantage of having a tridiagonal Hamiltonian, each diagonalization takes longer because the spherical representation of $\mathbf{U}(\tau + \Delta\tau, \tau)$ itself is not even close to diagonal except when $|\tau| \approx 0$. Unlike the p basis, $\langle\langle \mathbf{U}(\infty, -\infty) \rangle\rangle$ in the l basis does not approach diagonality for any range of V .

The adiabatic q basis works best out in the wings at $|\tau| \gg 3V$, but involves more tedious calculations: every microscopic step in every trial run requires an extra diagonalization (to obtain H_{qq}^{adi}), which automatically doubles the computation time of each factor in Eq. (C1). Moreover, the use of the Magnus-corrected matrix \mathbf{M} given by the multiple integrals in Eqs. (D1) must be done numerically, which requires yet further subdivisions of the microscopic subintervals to approximate the integrals.

The parabolic basis avoids most of these problems: it converges decently for the most interesting ranges of both τ and V (i.e., values not too large), when Magnus corrections up to order $(\Delta t)^5$ are incorporated; $\langle\langle \mathbf{U}(\infty, -\infty) \rangle\rangle$ further becomes diagonal in both limits $V \rightarrow 0$ and $V \rightarrow \infty$. The calculations are therefore simplified by using only this basis when seeking

$\mathbf{U}(|\tau_0|, \tau_0)$. The next layer of improvement would provide a test for goodness-of-basis in each macroscopic interval; at large enough times (e.g., $|\tau| > 5V$) the switch to the adiabatic basis would need to be made, and at smaller times to the diabatic basis.

A simple goodness-of-basis parameter for the j th interval is

$$G_j = \sum_{k', k=0}^{n-m-1} |U_{k'k}(\tau_j, \tau_{j-1})|. \quad (\text{C2})$$

If $\langle\langle \mathbf{U}(\tau_j, \tau_{j-1}) \rangle\rangle = \mathbf{1}$ (i.e., if \mathbf{U} is diagonal under some permutation of indices), then the basis is good and G_j equals its minimum possible value, $n-m$. In a very “undisagonal” basis, on the other hand, every element of \mathbf{U} would have the same magnitude, yielding the maximum value, $G_j = (n-m)^{3/2}$ (e.g., the unitary matrix $U_{k'k} = (n-m)^{-1/2} \exp[2\pi i k'k/(n-m)]$ is maximally poor in this sense).

Table IV illustrates the use of the three bases for the $n=10$, $m=0$ manifold. Results are given for six representative time intervals during both a fast ramp ($V=0.02$) and a slow ramp ($V=1.00$), with $\Delta\tau = \frac{1}{2}$; all Magnus corrections discussed in Appendix D are included (except only the first correction is included, numerically, for the adiabatic basis). The columns list final values for N'_j and G_j subject to a stringent accuracy of 10^{-8} as defined above; G_j ranges between 10 and 31.6. (Note that the trends of N'_j and G_j are not entirely monotonic; on a finer scale, they would be seen to dip to very low values on occasion.) Also listed are the total number of microscopic intervals needed, $\sum_j N'_j$, and the total number of intervals actually tried, according to the above sequence $N' = \{1, 2, \dots, N'_j\}$, for an entire sweep from $\tau=0-15$ with $\Delta\tau = \frac{1}{2}$. In addition to the trends evident in Table IV for the different bases, one should note the following rules of thumb when considering the entire time domain: (1) the inclusion of Magnus corrections in both spherical and parabolic bases reduces the number of diagonalizations by factors of at least 3–4 and 4–6 for slow and fast ramps, respectively; (2) about twice as many total microscopic steps are needed for slow ramps as for fast ramps; (3) the overhead of extra trial microscopic steps—beyond the $\{N'_j\}$ finally needed for convergence—is always about 120–125%.

Sign conventions

Our sign conventions are standardized by requiring the first element of every q eigenvector to be positive, if not zero (cf. Appendix B). In general, however, one must assume that the first element might go through a zero at some τ (except when there is only one $\mu_l \neq 0$, $l=m$, as in Sec. II C and Appendix B). If all elements but the first of an eigenvector are found to change sign after the next microscopic time step, the sign of the whole vector must be flipped. For the sake of consistency, this convention should also be used for the (constant) hydrogenic-basis transformation $U_{pl}^{(nm)}$ (Appendix A). One must also avoid diagonalization at precisely $\tau=0$, owing to state ambiguities for the degenerate eigenvalues.

TABLE IV. Number of microscopic steps N'_j and goodness-of-basis parameter G_j for $\mathbf{U}(\tau_j, \tau_{j-1})$ represented in three different bases, taken from half-traversals at both fast and slow ramps through the $n=10, m=0$ manifold between $\tau_0=0$ and $\tau=15$. Intervals $j=1, 6, 11, 16, 21$, and 30 are shown out of $N=30$ macroscopic divisions ($\Delta\tau=\frac{1}{2}$). The asterisk indicates lack of convergence (to 10^{-8}) for $N'_j \leq 500$. The last line under each basis lists $\sum_{j=1}^{30} N'_j$ and (in parentheses) the total number of trial microscopic steps for the whole ramp. See text.

Basis	$V=0.02$ (fast ramp)			$V=1.00$ (slow ramp)		
	$[\tau_{j-1}, \tau_j]$	N'_j	G_j	$[\tau_{j-1}, \tau_j]$	N'_j	G_j
Spherical	[0.0,0.5]	24	18.1	[0.0,0.5]	48	17.7
	[2.5,3.0]	24	25.6	[2.5,3.0]	48	28.5
	[5.0,5.5]	32	26.2	[5.0,5.5]	64	26.3
	[7.5,8.0]	32	26.7	[7.5,8.0]	64	27.2
	[10.0,10.5]	32	27.7	[10.0,10.5]	64	28.2
	[14.5,15.0]	48	28.0	[14.5,15.0]	100	28.3
	[0,15]	960 (2168)		[0,15]	1888 (4260)	
Parabolic	[0.0,0.5]	6	10.85	[0.0,0.5]	16	20.3
	[2.5,3.0]	16	10.22	[2.5,3.0]	32	18.8
	[5.0,5.5]	32	10.10	[5.0,5.5]	64	14.5
	[7.5,8.0]	32	10.07	[7.5,8.0]	64	13.4
	[10.0,10.5]	48	10.06	[10.0,10.5]	64	12.8
	[14.5,15.0]	48	10.04	[14.5,15.0]	100	11.9
	[0,15]	970 (2183)		[0,15]	1796 (4060)	
Adiabatic	[0.0,0.5]	*	22.3	[0.0,0.5]	200	13.2
	[2.5,3.0]	64	10.0107	[2.5,3.0]	150	10.447
	[5.0,5.5]	16	10.0011	[5.0,5.5]	32	10.050
	[7.5,8.0]	16	10.0004	[7.5,8.0]	32	10.019
	[10.0,10.5]	16	10.0002	[10.0,10.5]	32	10.010
	[14.5,15.0]	8	10.0001	[14.5,15.0]	32	10.003
	[0,15]	1774 (3794)		[0,15]	2526 (5502)	

APPENDIX D: MAGNUS CORRECTIONS

The use of the Magnus expansion for the time evolution matrix (Sec. III A) is discussed in Refs. [17–19,37,50]. In particular, Refs. [18,19] provide explicit terms for any generator $\mathcal{H}(t)$, and Refs. [37,50] discuss convergence properties of the exponential representation of \mathbf{U} . We consider here only results pertinent to the bowtie problem.

Solution of the Schrödinger equation (3.12) for $\mathbf{M}(t_b, t_a)$ leads to the integral representation (3.13), where $\mathbf{U}(t, t_a) = \exp[-i\mathbf{M}(t, t_a)]$, and $[t_a, t]$ is any small [50] time interval. Use of the series (3.14) and a term-by-term comparison of integrals of the same “order” then allows one to write each $\mathbf{M}^{(n)}(t, t_a)$ as a multiple integral of n factors $\mathcal{H}(t_i)$ ($i=1, \dots, n$); the n th-order term is an n -fold integral over $n-1$ unequal-time commutators of the $\{\mathcal{H}(t_i)\}$. The results up to $n=3$ are

$$\mathbf{M}^{(1)}(t, t_a) = \int_{t_a}^t dt_1 \mathcal{H}(t_1), \quad (\text{D1a})$$

$$\mathbf{M}^{(2)}(t, t_a) = -i \frac{1}{2} \int_{t_a}^t dt_1 \int_{t_a}^{t_1} dt_2 [\mathcal{H}(t_1), \mathcal{H}(t_2)], \quad (\text{D1b})$$

$$\mathbf{M}^{(3)}(t, t_a) = -\frac{1}{4} \int_{t_a}^t dt_1 \int_{t_a}^{t_1} dt_2 \int_{t_a}^{t_2} dt_3 [\mathcal{H}(t_1), [\mathcal{H}(t_2), \mathcal{H}(t_3)]] - \frac{1}{12} \int_{t_a}^t dt_1 \int_{t_a}^{t_1} dt_2 \int_{t_a}^{t_2} dt_2'' [[\mathcal{H}(t_1), \mathcal{H}(t_2'')], \mathcal{H}(t_2'')]. \quad (\text{D1c})$$

It will prove necessary also to keep one of several $n=4$ integrals, which will be evaluated below.

The special form $\mathcal{H}(t) = \mathbf{P} + F(t)\mathbf{Q}$, Eq. (3.15), further reduces the above expressions to integrals over a given field function $F(t)$, times commutators of the constant matrices \mathbf{P} and \mathbf{Q} . If the moments of $F(t)$ are denoted

$$J_n(t) = \int_{t_a}^t dt' (t' - t_a)^n F(t'), \quad (\text{D2})$$

evaluation of the above integrals yields

$$\mathbf{M}^{(1)}(t, t_a) = \mathbf{P}\Delta t + \mathbf{Q}J_0(t) = (\mathbf{P} + \mathbf{Q}\dot{F}\bar{t})\Delta t, \quad (\text{D3a})$$

$$\mathbf{M}^{(2)}(t, t_a) = i[\mathbf{P}, \mathbf{Q}][\frac{1}{2}\Delta t J_0(t) - J_1(t)] = i[\mathbf{P}, \mathbf{Q}]\frac{1}{12}\dot{F}(\Delta t)^3, \quad (\text{D3b})$$

$$\begin{aligned} \mathbf{M}^{(3)}(t, t_a) &= [[\mathbf{P}, \mathbf{Q}], \mathbf{P}] \left[\frac{1}{12} (\Delta t)^2 J_0(t) - \frac{1}{2} \Delta t J_1(t) + \frac{1}{2} J_2(t) \right] \\ &\quad - [[\mathbf{P}, \mathbf{Q}], \mathbf{Q}] \left[\frac{1}{2} J_0(t) J_1(t) - \frac{5}{12} \Delta t [J_0(t)]^2 + \frac{1}{2} \int_{t_a}^t dt' [J_0(t')]^2 \right] \\ &= - [[\mathbf{P}, \mathbf{Q}], \mathbf{Q}] \frac{1}{240} \dot{F}^2 (\Delta t)^5, \end{aligned} \quad (\text{D3c})$$

where $\Delta t = t - t_a$ and $\bar{t} = \frac{1}{2}(t_a + t)$. The final equality given for each $\mathbf{M}^{(n)}(t, t_a)$ applies specifically to $F(t) = \dot{F}t$ and appears in Eq. (3.16). Note that the coefficient of $[[\mathbf{P}, \mathbf{Q}], \mathbf{P}]$ in $\mathbf{M}^{(3)}(t, t_a)$ vanishes in this case.

For linear fields, an alternative ansatz to the series (3.14) is a direct expansion of $\mathbf{M}(t, t_a)$ in terms of all linearly independent commutators of \mathbf{P} and \mathbf{Q} :

$$\mathbf{M}(t, t_a) = (\mathbf{P} + \mathbf{Q}\dot{F}\bar{t})\Delta t + [\mathbf{P}, \mathbf{Q}]a_{PQ}(t) + [[\mathbf{P}, \mathbf{Q}], \mathbf{P}]a_{PQ,P}(t) + [[\mathbf{P}, \mathbf{Q}], \mathbf{Q}]a_{PQ,Q}(t) + [[[\mathbf{P}, \mathbf{Q}], \mathbf{P}], \mathbf{P}]a_{PQ,P,P}(t) + \cdots, \quad (\text{D4})$$

which circumvents the general results (D1)–(D3). Substitution of (D4) into Eq. (3.13) yields the coefficients $a_{PQ} \propto \dot{F}(\Delta t)^3$, $a_{PQ,P} = 0$, and $a_{PQ,Q} \propto \dot{F}^2(\Delta t)^5$, as obtained above. Note that each factor \mathbf{Q} in a multiple commutator is accompanied by a factor \dot{F} , from the term $\dot{F}t\mathbf{Q}$ in the Hamiltonian in Eqs. (D1). Furthermore, if there are n_P factors \mathbf{P} and n_Q factors \mathbf{Q} in the commutators, $\mathbf{M}^{(n)}(t, t_a)$ has $n = n_P + n_Q$ time integrals, including a product of time factors of total dimension $[t^{n_Q}]$. $\mathbf{M}^{(n)}(t, t_a)$ will thus have terms that scale like $(\Delta t)^{n_P + 2n_Q}$, with several possible powers $n_P + 2n_Q \geq n + 1$ contributing to the n th-order term when $n > 3$. In particular, $n = 4$ contains a nonzero coefficient $a_{PQ,P,P}(t)$ that scales like $(\Delta t)^5$. Inclusion of $\mathbf{M}^{(3)}(t, t_a) \propto (\Delta t)^5$ requires that this $n = 4$ term also be kept if uniform convergence of $\mathbf{M}(t, t_a)$ is to obtain as $\Delta t \rightarrow 0$. Only the third integral in Eq. (3.13) contributes to $a_{PQ,P,P}(t)$; substitution of (D4) leads to

$$\begin{aligned} \mathbf{M}^{(4)}(t, t_a) &= -\frac{1}{12} \int_{t_a}^t dt' \left[\mathbf{P}(t' - t_a) + \cdots, \left[\cdots + [\mathbf{P}, \mathbf{Q}] \frac{i}{12} \dot{F}(t' - t_a)^3 + \cdots, \mathbf{P} + \cdots \right] \right] + \cdots \\ &= i[[[\mathbf{P}, \mathbf{Q}], \mathbf{P}], \mathbf{P}] \frac{1}{720} \dot{F}(\Delta t)^5 + \cdots, \end{aligned} \quad (\text{D5})$$

where the ellipses represent other terms. A further refinement, necessary at large $|t|$, is to replace each \mathbf{P} in the triple commutator with $\mathcal{H}(\bar{t}) = \mathbf{P} + \mathbf{Q}\dot{F}\bar{t}$. The term (D5) should be added to those of Eq. (3.16) when doing calculations with “third-order” Magnus corrections for the bowtie.

-
- [1] Also known as the Landau-Zener-Stueckelberg effect. Stueckelberg's contribution is not meant to be slighted; see C. Stueckelberg, *Helv. Phys. Acta* **5**, 369 (1932).
- [2] J. R. Rubbmark, M. M. Kash, M. G. Littman, and D. Kleppner, *Phys. Rev. A* **23**, 3107 (1981).
- [3] *Rydberg States of Atoms and Molecules*, edited by R. F. Stebbings and F. B. Dunning (Cambridge University Press, New York, 1983), Chaps. 3 and 9.
- [4] C. Higgs, M. A. Fineman, F. B. Dunning, and R. F. Stebbings, *J. Phys. B* **15**, L697 (1982).
- [5] D. R. Mariani, W. van de Water, P. M. Koch, and T. Bergeman, *Phys. Rev. Lett.* **50**, 1261 (1983).
- [6] R. G. Rolfs, D. B. Smith, and K. B. MacAdam, *J. Phys. B* **16**, L533 (1983). See also K. B. MacAdam, R. Rolfs, and D. A. Crosby, *Phys. Rev. A* **24**, 1286 (1981).
- [7] Fine-structure effects are ignored here. Their inclusion would require only trivial modifications, such as defining states (n, l, m_l, m_j) , (n, n_1, m_l, m_j) , etc., with m_j but not m_l conserved.
- [8] L. D. Landau and E. M. Lifshitz, *Quantum Mechanics (Non-Relativistic Theory)* (Pergamon, Oxford, 1976).
- [9] H. A. Bethe and E. E. Salpeter, *Quantum Mechanics of One- and Two-Electron Atoms* (Springer, Berlin, 1957).
- [10] D. A. Harmin, *Phys. Rev. A* **30**, 2413 (1984).
- [11] U. Fano and A. R. P. Rau, *Atomic Collisions and Spectra* (Academic, Orlando, 1986).
- [12] M. L. Zimmerman, M. G. Littman, M. M. Kash, and D. Kleppner, *Phys. Rev. A* **20**, 2251 (1979).
- [13] Concerning applications of quantum-defect theory, one would use a K matrix instead of the potential matrix elements $\langle nl' | V | nl \rangle = \delta_{l'l} (-\mu_l n^{-3})$, and replace μ_l with $\pi^{-1} \tan \pi \mu_l$, which is not limited to $(-\frac{1}{2}, \frac{1}{2})$; Eqs. (1.3) and (1.5) then lead to $\tan |\pi \mu| < \pi n / 15$. See Refs. 10 and 11.
- [14] H. B. van Linden van den Heuvell and T. F. Gallagher, *Phys. Rev. A* **32**, 1495 (1985).
- [15] C. Zener, *Proc. R. Soc. London, Ser. A* **137**, 696 (1932).
- [16] The special case where all levels but one have the same slope dE/dt is solvable: Yu. N. Demkov, *Dokl. Acad. Nauk SSSR* **166**, 1076 (1966) [*Sov. Phys.—Dokl.* **11**, 138 (1966)]; Yu. N. Demkov and V. I. Osherov, *Zh. Eksp. Teor. Fiz.* **53**, 1589 (1967) [*Sov. Phys.—JETP* **26**, 916 (1968)]. See also Y. Kayanuma and S. Fukuchi, *J. Phys. B* **18**, 4089 (1985).
- [17] See, e.g., (a) J. D. Dollard and C. N. Friedman, *J. Math. Phys.* **18**, 1598 (1977); (b) G. F. Thomas and W. J. Meath, *J. Phys. B* **16**, 951 (1983). See also the references in (c) S.-I. Chu, *Adv. At. Mol. Phys.* **21**, 197 (1985).
- [18] K. F. Milfeld and R. E. Wyatt, *Phys. Rev. A* **27**, 72 (1983), and references therein.
- [19] S. Klarsfeld and J. A. Oteo, *Phys. Rev. A* **39**, 3270 (1989).
- [20] K. B. MacAdam (private communication).
- [21] W. van de Water, K. A. H. van Leeuwen, S. Yoakum, E. J. Galvez, L. Moorman, T. Bergeman, B. E. Sauer, and P. M. Koch, *Phys. Rev. Lett.* **63**, 762 (1989); W. van de Water, S.

- Yoakum, T. van Leeuwen, B. E. Sauer, L. Moonman, E. J. Galvez, D. R. Mariani, and P. M. Koch, *Phys. Rev. A* **42**, 572 (1990).
- [22] Reference 9, p. 263, Eq. (63.5). See also P. N. Price and D. A. Harmin, *Phys. Rev. A* **42**, 2555 (1990). The minus sign in Eq. (2.8) is necessary for consistency with the transformation $U^{(nm)}$ in (2.13) and (A1). This sign follows from the assumption that all wave functions are positive as $r \rightarrow 0$, $\xi \rightarrow 0$, and $\eta \rightarrow 0$.
- [23] E. Luc-Koenig and A. Bachelier, *J. Phys. B* **13**, 1743 (1980); **13**, 1769 (1980).
- [24] D. A. Harmin, *Phys. Rev. A* **24**, 2491 (1981).
- [25] A renormalized form of the Runge-Lenz vector is often called A , with $A_z = (n_1 - n_2)/n = p/n$. See Ref. 8 (Sec. 37); Ref. 10; and, for a group-theoretical discussion, M. J. Englefield, *Group Theory and the Coulomb Problem* (Wiley, New York, 1972).
- [26] D. A. Harmin, in *Atoms in Strong Fields*, edited by C. A. Nicolaides, C. W. Clark, and M. H. Nayfeh (Plenum, New York, 1990), p. 61.
- [27] This example applies to a subset of any two levels out of the manifold's $n - m \geq 2$ levels. The case $n = 2$, $l = m = 0$ has just $p = \pm 1$ and $u_1 = u_2 = 1$.
- [28] The two-level results simplify when the weights are equal, $u_1^2 = u_2^2 = u^2$, whence the anticrossing center lies at $\bar{\tau} = 0$ and $\bar{E} = -Vu^2$, where the levels are $E_+ = 0$ and $E_- = -2Vu^2$ and the gap is $\Delta E = 2Vu^2 = 2|\bar{E}|$. If $|u_1| \neq |u_2|$, the gap $\Delta E = 2V|u_1 u_2|$ is smaller than $-2Vu^2$ in magnitude.
- [29] Certain subclasses of three-level manifolds can be solved analytically. See C. E. Carroll and F. T. Hioe, *J. Phys. A* **19**, 2061 (1986), and references therein.
- [30] The Lorentzian form of the two-level adiabatic coupling arising from a P matrix was shown by C. W. Clark, *Phys. Lett.* **70A**, 295 (1979).
- [31] Equation (2.44) agrees with the effective width of a two-level anticrossing defined in Eq. (7) of Ref. 2. See also D. R. Bates, *Proc. R. Soc. London, Ser. A* **257**, 22 (1960); M. R. Spalburg, J. Los, and A. Z. Devdariani, *Chem. Phys.* **103**, 253 (1986); K. Mullen, E. Ben-Jacob, Y. Gefen, and Z. Schuss, *Phys. Rev. Lett.* **62**, 2543 (1989).
- [32] See Eqs. (3.14)–(3.26), Sec. III A of Ref. 10. The present Eq. (2.53) is plotted in Figs. 1 and 2(a) of that reference, which are seen to represent the inverse of Eq. (2.54), plotted here in Fig. 4.
- [33] Equation (2.56) is true for $m \neq 0$ upon the replacement $n(\frac{1}{2}n - \varphi^{-1}) \rightarrow \frac{1}{2}(n - m)^2 - n\varphi^{-1}$.
- [34] A reasonable guess begins with $E_0^\tau = -V - (n - 1)\sqrt{V^2 + \tau^2}$, which correctly satisfies $E_0^\tau = -nV$ at $\tau = 0$ as well as the first two terms of the asymptotic series (2.48). The rescaling (2.50) then yields $\lambda g = n(\frac{1}{2} - \varphi^{-1}) - (n - 1)[(1 + \frac{1}{4}\varphi^2)^{1/2} - 1]/\varphi$, which can be employed in Eq. (2.61). Nevertheless, Γ_{0q}^τ still eludes the simple form that Fig. 5 seems to suggest.
- [35] The maximum adiabatic coupling converges at large n ; e.g., at $n = 10, 40$, and 80 one finds Γ_{01}^τ or $\Gamma_{0n-1}^\tau = 0.364, 0.350$, and 0.348 , respectively. A fit to the positions of these maxima over the entire range $n = [10, 80]$ yields $|\tau| \approx \frac{1}{2}V \ln(n - 1.021) - 0.020$, which is consistent with $\varphi = \sigma_1 = -\sigma_{n-1}$.
- [36] In the q basis, adiabatic transitions have $q \rightarrow q' = q$. For one nonzero μ_l , we can always define two nearest-neighbor transitions $q \rightarrow q' \neq q$: (1) diabatic, where $q = 0$ goes to $q' = n - m - 1$, and $q \rightarrow q' = q - 1$ for other q ; (2) other-neighbor, where $q = n - m - 1$ goes to $q' = 0$, and $q \rightarrow q' = q + 1$ for other q .
- [37] W. Magnus, *Comm. Pure Appl. Math.* **7**, 649 (1954); P. Pechukas and J. C. Light, *J. Chem. Phys.* **44**, 3897 (1966).
- [38] Actually, a fourth-order Magnus term that is $\sim O((\Delta t)^5)$ —of the same order as the third term in Eq. (3.16)—is also evaluated, since convergence as $\Delta t \rightarrow 0$ depends on the power of Δt ; see Appendix D, Eq. (D5).
- [39] The argument $(\frac{1}{2}\mathbf{p}\tau^2 - \mathbf{v}\tau)$ is just $\int_0^\tau d\tau'(\mathbf{p}\tau' - \mathbf{v})$. The lower limit $\tau' = 0$ is arbitrary but implies $A(\tau, \tau) = \mathbf{1}$; the choice $\tau' = \tau_0$ would guarantee $A(\tau, \tau) = \mathbf{1}$.
- [40] See M. V. Berry, *Proc. R. Soc. London, Ser. A* **429**, 61 (1990), for a discussion of transitions in the adiabatic limit.
- [41] The value $V = 0.3$ by no means represents a very fast ramp rate, nor is $V = 0.5$ terribly slow; these values were chosen for Fig. 6 to illustrate nontrivial mixtures of the levels. A diabatic (adiabatic) transition will occur with nearly 100% probability for $V \lesssim 0.1$ for any q ($V \gtrsim 1$ for $q = 0$, $V \gtrsim 2$ for $q \neq 0$). See Figs. 7–11.
- [42] Note in Fig. 8(a) the symmetry $P_{p \rightarrow p} = P_{-p \rightarrow -p}$ implied by Eq. (3.20). The analogous symmetry for the q levels in Fig. 8(b) translates into $P_{q \rightarrow q} = P_{n-q \rightarrow n-q}$, $1 \leq q \leq n - 1$; $P_{0 \rightarrow 0}$ is unique.
- [43] There is nothing exceptional about even $n - m$ (as opposed to odd $n - m$) as the number of states in the manifold increases.
- [44] The nonmonotonic dependence on n of the adiabatic-curve shapes at low V follows from Eqs. (3.28)–(3.29c). Using $p = +(n - 1)$ and $p' = -(n - 1)$, one finds $P_{q=0 \rightarrow q'=0}(V) \approx \pi V^2 / (n - 1) + \sqrt{[\pi/2(n - 1)]\pi^2 V^3 + O(V^4)}$ as $V \rightarrow 0$, where $\Sigma_1 = \Sigma_3 = 0$ and we have used $\lim_{n \rightarrow \infty} \Sigma_2 = \frac{1}{2}\pi$ for the sum (3.29b).
- [45] The approximate form of β_n in Eq. (4.2) is already good to 1% for $n = 3$. See M. Abramowitz and I. A. Stegun, *Handbook of Mathematical Functions* (Dover, New York, 1970), Chap. 6. Euler's constant is $\gamma = 0.5772\dots$, and $e^\gamma = 1.781\dots$.
- [46] D. Park, *Z. Phys.* **159**, 155 (1960).
- [47] See Ref. 26, Sec. III E, for a detailed discussion of $U_{pl}^{(nm)}$, and Eq. (3.71) and Table I therein for results. See also D. A. Harmin, *Phys. Rev. A* **26**, 2656 (1982).
- [48] M. Abramowitz and I. A. Stegun, *Handbook of Mathematical Functions* (Ref. 45), Chap. 7.
- [49] This sequence would be especially well suited to a Richardson-type *extrapolation* scheme, whereby predictions of \mathbf{U} based on the first several trials are deemed more reliable as they better converge to the actual \mathbf{U} obtained from higher- N_j' trials. See W. H. Press, B. P. Flannery, S. A. Teukolsky, and W. T. Vetterling, *Numerical Recipes* (Cambridge University Press, New York, 1986). However, the problem of “extrapolating” the entire matrix \mathbf{U} while maintaining unitarity is nontrivial and may be computationally costly.
- [50] F. M. Fernandez, *Phys. Rev. A* **41**, 2311 (1990).